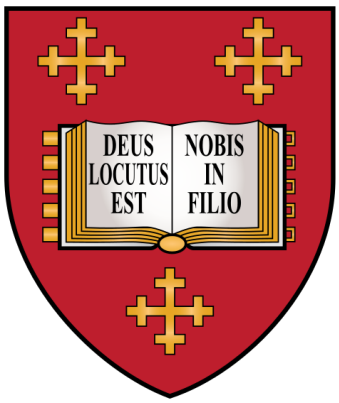

Solvation structure, transport and stability in Li-ion battery electrolytes

Conor Phelan

Mansfield College

University of Oxford

A thesis submitted for the degree of Doctor of Philosophy in Materials

Trinity 2024

Declaration

This thesis is submitted to fulfil the requirements for the degree of Doctor of Philosophy in the Department of Materials at the University of Oxford. I declare that this thesis has not been submitted, in whole or in part, in any previous application for a degree. I declare that, except where specific reference is made to the work of others, or explicit acknowledgement is given, the contents of this dissertation are the results of my own work and this thesis contains fewer than 40,000 words.

Acknowledgements

Firstly I would like to thank my supervisor, Prof Robert Weatherup, for giving me the chance to undertake my DPhil at the Materials Department in the University of Oxford. Thank you for the many, many discussions on electrolyte solvation structure, bringing a level of sanity to my optimistic ideas and giving me the freedom and backing to pursue research questions I had a genuine interest in. Thanks to this I have developed skills and gained knowledge that I don't think I would have been able to acquire anywhere else and will be forever grateful for the opportunity you've given me.

Next I would like to thank all the past and present members of the Weatherup research group. It has truly been a pleasure both in the lab and in the pub (on the rare occasions I actually turned up!). To Erik, thank you for always being so willing and eager to help with my projects whenever your battery expertise was required. Especially in my first year, your consistent guidance and support helped me find my feet and begin developing the skills I'd need to carry out my projects. I'll always look back fondly on the many problems you'd give invaluable insight on, always opening the answer with "In my old lab...". To Jack, thank you for suffering the many, many discussion we have had on MD, solvation structure, DFT in general and electrolyte O K-edges. Working with all of you has been a highlight of my time in Oxford and will look back on it fondly for many years to come.

It's safe to say rowing has been a very enjoyable part of my time here. Rowing with Mansfield College and especially vice-captaining the club in my final year has been an absolute pleasure. We may not have won blades but we definitely had the best vibes on the river every single year. The wonderful people I've met through Mansfield College and unforgettable memories from my time there is something I'll look back on with a smile for the rest of my life.

Last but certainly not least, Mom, Dad, Michaela and Caoimhe, a big thank you for all of your continued support, guidance and wisdom throughout my life so far. Without all of you I would never be where I am now and for that I will be eternally grateful. An especially big thank you for putting up with my horrendous text message response times, but still always making time and en effort on my account. It means the world to me and I wouldn't have been able to do this DPhil without you.

Publications

Swallow, J.E., Fraser, M.W., Kneusels, N.J.H., Charlton, J.F., Sole, C.G., Phelan, C.M., Björklund, E., Bencok, P., Escudero, C., Pérez-Dieste, V. and Grey, C.P., 2022. Revealing solid electrolyte interphase formation through interface-sensitive Operando X-ray absorption spectroscopy. Nature Communications, 13(1), p.6070.

Phelan, C.M., Bjorklund, E., Singh, J., Fraser, M., Didwal, P.N., Rees, G.J., Ruff, Z., Ferrer, P., Grinter, D.C., Grey, C.P. and Weatherup, R.S., 2024. Role of Salt Concentration in Stabilizing Charged Ni-Rich Cathode Interfaces in Li-Ion Batteries. Chemistry of Materials, 36(7), pp.3334-3344.

An, L., Swallow, J.E., Cong, P., Zhang, R., Poletayev, A.D., Björklund, E., Didwal, P.N., Fraser, M.W., Jones, L.A., Phelan, C.M. and Ramesh, N., 2024. Distinguishing bulk redox from near-surface degradation in lithium nickel oxide cathodes. Energy Environmental Science, 17(21), pp.8379-8391.

Ramesh, N., Banerjee, H., Swallow, J.E., Bjorklund, E., Dean, A., Didwal, P., Fraser, M., Phelan, C.M., An, L., Singh, J. and Lewis, J., 2024. Atomistic Interpretation of the Oxygen K-Edge X-ray Absorption Spectra of Layered Li-Ion Battery Cathode Materials. Chemistry of Materials, 36(22), pp.11051-11064.

Abstract

The electrolyte is a key component in lithium-ion batteries (LIB), which will play a crucial role in mitigating the global dependence on fossil fuels through the electrification of vehicles and the storage of energy from renewable sources. Our understanding of these devices continually evolves as we delve into the reactions occuring at the interface between the electrodes and the electrolyte. To further improve LIB energy densities for vehicle electrification and grid-scale energy storage applications through the use of high voltage cathode materials, a thorough understanding of electrolyte solvation structure, transport and electrochemical stability must be achieved.

The effect of salt concentration on the electrochemical stability of lithium hexafluorophosphate ($LiPF_6$) in ethylene carbonate (EC) : ethyl methyl carbonate (EMC) (vol:vol 3:7) electrolytes at high voltage, Ni-rich cathode interfaces has been investigated. Initially, we investigate the cathode-electrolyte interphase (CEI), examining the influence of $LiPF_6$ salt concentration on its composition in $LiN_{0.8}Mn_{0.1}Co_{0.1}O_2$ (NMC811) and $Li_4Ti_5O_{12}$ (LTO) cells under constant potential holds. We propose reaction mechanisms describing the degradation of electrolyte components on the NMC811 surface by considering the observed degradation and CEI composition post cycling.

Next, the relationship between electrolyte solvation structure and continuum scale transport properties are linked by investigating the behaviour of electrolytes under applied currents. We calculate Maxwell-Stefan diffusion coefficients ($Đ_{ij}$), and thermodynamic-activity factors (Γ_{ij}) directly from classical molecular dynamics (MD) simulations for LIB electrolytes in the Maxwell-Stefan (MS) diffusion formulation. This approach combines MD with operando confocal Raman microspectroscopy to test the accuracy of these parameters against experimental concentration gradients formed under a constant current. We present the computed values of these parameters for electrolytes investigated herein.

Finally, we study the relationship between electrolyte solvation structure and electrochemical stability using MD, density functional theory (DFT), X-ray absorption spectroscopy (XAS) and Raman spectroscopy. MD, Raman spectroscopy and XAS reveal the influence of salt concentration on the solvation environments in LIB electrolytes. DFT reveals the effect of salt concentration on the highest occupied molecular orbital (HOMO) and lowest unoccupied molecular orbital (LUMO) states. The inferred impact of these changes on both the oxidative and reductive stabilities of the electrolyte are compared to experimental findings.

This comprehensive study offers new insights into the correlation between electrolyte solvation structure and salt concentration, elucidating its consequential effects on transport properties, electrochemical stability and CEI composition, particularly concerning high voltage nickel-rich $LiNi_{1-x-y}Mn_xCo_yO_2$ (NMC) cathode materials in carbonate based LIB electrolytes. Such insights pave the way for informed strategies aimed at mitigating NMC degradation at elevated potentials, such as through the judicious selection of electrolyte additives to aid the widespread adoption of high voltage cathodes in electric vehicles and grid-scale energy storage systems.

Statement of Authorship

1. In Chapter 3, the inductively coupled plasma optical emission spectroscopy (ICP-OES) measurments on the LTO anodes and glass fiber (GF) separators were performed by Dr Zachary Ruff under the supervision of Prof Clare Grey at the Department of Chemistry, University of Cambridge.

2. In Chapter 5, the DFT calculations performed using the ONETEP linear scaling code were performed by Dr Arihant Bhandari under the supervision of Prof Chris-Kriton Skylaris at the University of Southampton.

Contents

List of Abbreviations

$E_{\mathbf{B}}$ binding energy.

$E_{\mathbf{K}}$ kinetic energy.

$R_{\mathbf{ct}}$ charge transfer resistance.

$\Delta\nu$ wavenumbers.

Γ_{ij} thermodynamic-activity factors.

$\mathbf{Đ}_{ij}$ Maxwell-Stefan diffusion coefficients.

HF hydrofluoric acid.

AGG Aggregates.

BVP boundary value problem.

CCD charged coupled device.

CEI cathode-electrolyte interphase.

CIP contact ion pairs.

CN coordination number.

COM center of mass.

CPE constant phase elements.

DEC diethyl carbonate.

DFN Doyle-Fuller-Newman.

DFT density functional theory.

DLS Diamond Light Source.

DMC dimethyl carbonate.

DN dual numbers.

DOS density of states.

EC ethylene carbonate.

EIS Electrochemical impedance spectroscopy.

EMC ethyl methyl carbonate.

ESCA electron spectroscopy for chemical analysis.

EXAFS extended X-ray absorption fine structure.

FEC fluoroethylene carbonate.

FY fluorescence yield.

GF glass fiber.

HOMO highest occupied molecular orbital.

ICP-OES inductively coupled plasma optical emission spectroscopy.

IPFY inverse partial fluorescence yield.

LCE Locally concentrated electrolytes.

LCO lithium cobalt oxide ($LiCoO_2$).

LDFP lithium difluorophosphate.

LED lithium ethylene dicarbonate, $(CH_2OCO_2Li)_2$.

Li^+ Lithium ions.

LIB lithium-ion batteries.

$LiPF_6$ lithium hexafluorophosphate.

LTO $Li_4Ti_5O_{12}$.

LUMO lowest unoccupied molecular orbital.

MD classical molecular dynamics.

MRI magnetic resonance imaging.

MS Maxwell-Stefan.

NMC $LiNi_{1-x-y}Mn_xCo_yO_2$.

NMC811 $LiN_{0.8}Mn_{0.1}Co_{0.1}O_2$.

NMR Nuclear magnetic resonance spectroscopy.

NXES non-resonant X-ray emission spectrum.

OPAS Osmotic Pressure Activity of Solvent.

OPLSAA non-polarizable optimized potential for liquid simulations all-atom.

PC propylene carbonate.

PF_6^- hexafluorophosphate.

PMT photomultiplier tube.

rdf radial distribution function.

RESP Restrained Electrostatic Potential.

rf radiofrequency.

RSL reduced surface layer.

RXES resonant X-ray emission spectrum.

SEI solid-electrolyte interphase.

SoC state of charge.

SSIP solvent separated ion pairs.

T1 Spin-lattice relaxation.

T2 spin-spin relaxation.

TEY total electron yield.

TM transition metal.

UK United Kingdom.

VACF velocity autocorrelation function.

XANES X-ray absorption near edge structure.

XAS X-ray absorption spectroscopy.

XPS X-ray photoelectron spectroscopy.

Chapter 1

Introduction

As the demand for energy in modern times continues to increase so too does the desire to move away from environmentally unfriendly fossil fuels towards greener, renewable forms of energy such as wind and sunlight. Due to the intermittent nature of these energy sources, the times of maximum energy generation do not coincide with times of peak energy demand. Consequently, improved grid-scale energy storage solutions are required to capture the energy when it is produced and provide it to satisfy the energy demand peaks or supply troughs. The United Kingdom (UK) also aims to bring all greenhouse gas emissions to net zero by 2050.[1] LIBs are playing a key role in realising these energy storage and vehicle electrification targets.

LIBs are a cornerstone technology in modern society, powering a vast array of devices from smartphones and laptops to electric vehicles and grid storage systems. They represent a significant evolution in energy storage technology, characterized by ongoing innovations that have enhanced their capacity, safety, and efficiency. The origins of LIB technology can be traced back to the mid-20th century, as researchers sought alternatives to traditional lead-acid and nickel-cadmium batteries. In the 1970s M. Stanley Whittingham developed the concept of a rechargeable lithium battery while working at Exxon, using titanium disulfide (TiS_2) as the cathode material and metallic lithium as the anode. His prototype demonstrated the potential of lithium as a high energy density material but safety concerns related to the use of metallic lithium, in particular the formation of dendrites causing short circuits, limited its application. In the years that followed at the University of Oxford John B. Goodenough discovered lithium cobalt oxide ($LiCoO_2$) (LCO) as a stable, high voltage cathode material. In 1985, Akira Yoshino identified petroleum coke, a carbon based electrode, as a suitable anode to pair with LCO while working at Asahi Kasei Corporation in Japan. Unlike metallic lithium, this anode did not form dendrites leading to the creation of a safer, rechargeable LIB that could be commercialized. This was

done by Sony Corporation and Asahi Kasei in 1991. For their efforts, Whittingham, Goodenough and Yoshino were awarded the Nobel Prize in Chemistry in 2019.

LIBs are a highly efficient form of electrochemical energy storage. They possess low self discharge rates, high coulombic efficiencies, high energy densities and relatively wide operating temperature ranges.[2–5] The ever decreasing cost of LIBs has made them an appealing option for vehicle electrification, but even higher energy densities than the current state of the art are required for them to fulfill this role. Higher voltage cathode materials such as Ni-rich NMC are a promising option to realise higher energy density LIBs, but their electrochemical instability has impeded widespread adoption. Cobalt possesses ethical concerns regarding its acquisition[6] but may be substituted by nickel to achieve higher theoretical specific capacities, also lower cost, because nickel is more abundant.[7,8] However, nickel-rich NMC cathodes exhibit poor electrochemical stabilities at high voltages due to parasitic side reactions with the electrolyte.[9–11] These result in phase transitions and structural degradation, causing capacity loss and poor cycling performance. Structural degradation is accompanied by transition metal (TM) dissolution and incorporation into the solid-electrolyte interphase (SEI) formed on the anode, further compromising long term cycling performance.[12] Highly concentrated electrolytes have been proposed as a solution to stabilise the reactive nickel-rich interfaces and enable their widespread use. Consequently, a comprehensive understanding of the effect of concentration on electrolyte properties and the consequent influence on electrochemical stability must be achieved to enable the widespread adoption of high voltage cathodes in modern LIBs.

1.1 Fundamentals of LIBs

Figure 1.1 shows the basic design of a LIB cell. The terms *cathode* and *anode* originate from the direction of electron flow at the electrode interfaces. A *cathodic current* is when electrons are transferred from the electrode phase to the electrolyte phase. An *anodic current* is when electrons are transferred from the electrolyte phase to the electrode phase. Between charging and discharging, the direction of current flow changes. Consequently, the electrodes acting as the cathode and anode are different between charging and discharging. In the battery literature the terms cathode and anode are used to describe the behaviour of electrodes during discharge. Consequently, the positive electrode (i.e. the electrode that undergoes redox reactions at a more positive potential compared to the negative electrode) is called the cathode, and the negative electrode, the anode. The electrolyte is an electronic insulator which is ionically conducting. Current in the electrolyte is carried by the flow of ions. In the electrode and the external circuit, current is carried by electrons. In commercial cells, electrodes are cast on current collectors, which are alternatively stacked on top of each other, and a separator soaked in electrolyte is placed between the layers. The separator prevents physical contact between electrodes to prevent short circuits while allowing the flow of electrolyte solvents and ions through it. The cathode and anode materials are often powders with poor electronic conductivities. The powders are often mixed with a polymer based binder and an electronically conducting additive like carbon black to form a coating. The coating is then cast on current collector such as copper for the anode and aluminium for the cathode. The result is the formation of a conductive network between active material particles allowing the efficient extraction and incorporation of electrons between the electrode and the external circuit during LIB operation. The electrolyte is typically $LiPF_6$ dissolved in a mixture of cyclic and linear organic carbonates with additives. During LIB discharge oxidation and reduction occur at the anode cathode respectively. Equations 1.1 and 1.2 show the half reactions for a cell with a graphitic anode (C_6) and LCO as an anode.

$$\mathrm{Li}_x\mathrm{C}_6 \rightleftharpoons x\mathrm{Li}^+ + x\mathrm{e}^- + \mathrm{C}_6 \tag{1.1}$$

$$\mathrm{Li}_{1-x}\mathrm{CoO}_2 + x\mathrm{Li}^+ + x\mathrm{e}^- \rightleftharpoons \mathrm{LiCoO}_2 \tag{1.2}$$

$$\mathrm{Li}_x\mathrm{C}_6 + \mathrm{Li}_{1-x}\mathrm{CoO}_2 \rightleftharpoons \mathrm{LiCoO}_2 + \mathrm{C}_6 \tag{1.3}$$

Lithium ions (Li^+) are reduced at the cathode, consuming an electron from the current

collector while being incorporated into its structure. The anode is oxidised, resulting in the release of Li^+ into the electrolyte and an electron into the current collector. During LIB charging the reverse reactions occur. Equation 1.3 represents the simplified full cell equation describing the operation of a LCO vs. graphite full cell. The potential of the electrode is determined by its state of lithiation. The Gibbs free energy change quantifies the amount of chemical energy that may be stored/released in the cell that depends on the potential difference between the electrodes, E_{cell}.

$$\Delta G = -nFE_{\text{cell}} \tag{1.4}$$

n is the number of electrons exchanged in the process and F is Faraday's constant. During discharge the potential difference between the electrodes drives electrons between electrodes to lower the cell potential, doing work in the external circuit in the process. The cell specific capacity is a measure of the ability of the electrodes to store Li^+.

$$\text{Specific Capacity} = \frac{nF}{3600M_{\text{w}}} \tag{1.5}$$

M_w is the molecular weight of the active material. The unit of specific capacity is mAh g^{-1}. The theoretical battery cell energy is given by the product of the cell potential, E_{cell} and the cell capacity.

$$\text{Cell Energy} = E_{\text{cell}} \times \text{Active Material Mass} \times \text{Specific Capacity} \tag{1.6}$$

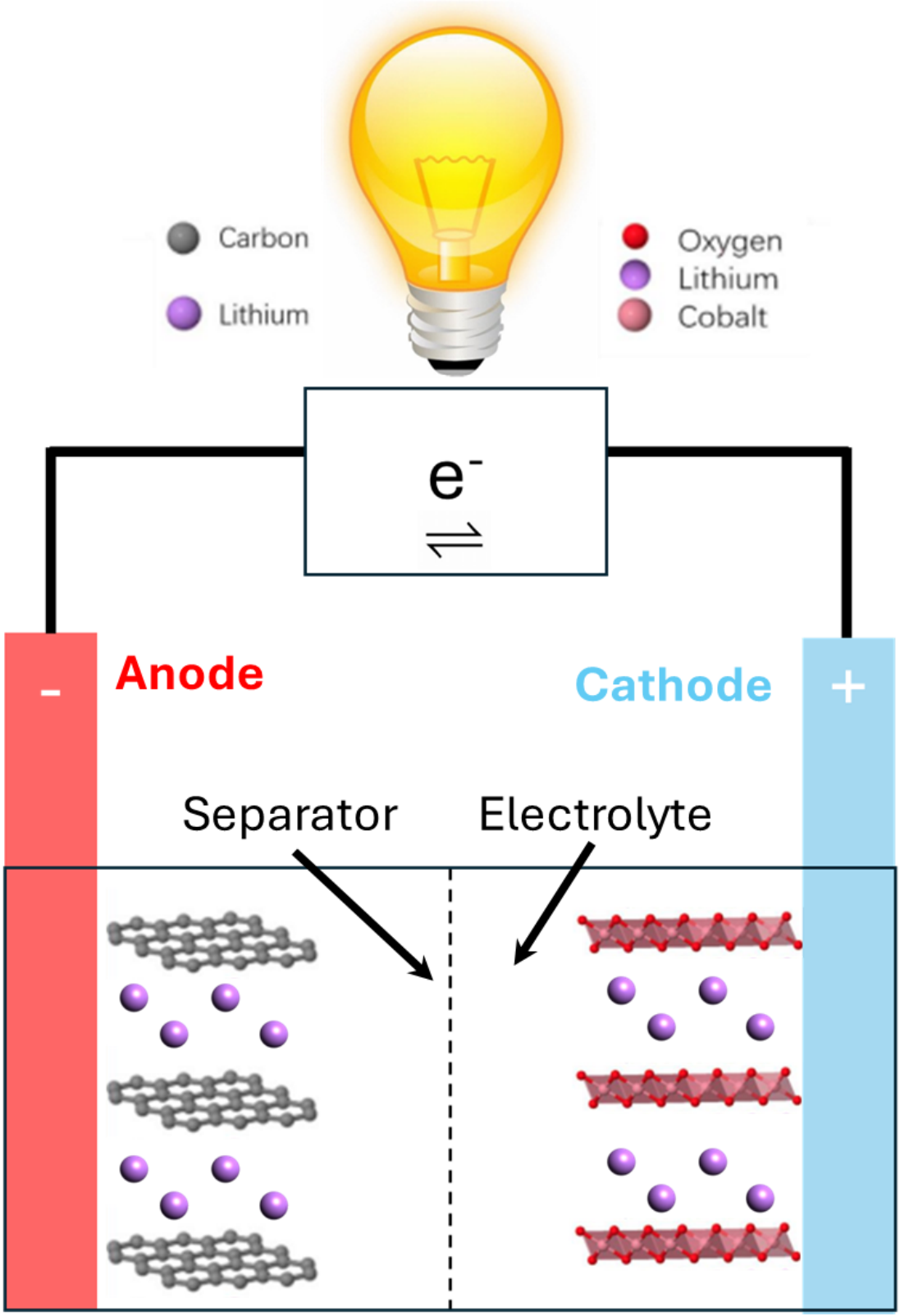

Figure 1.1: Schematic of a LIB cell. The cathode and anode are connected via an external circuit and immersed in an electrolyte. The redox processes described in equations 1.1 and 1.2 occur at the anode and cathode respectively, generating electrons. The separator avoids short circuits by preventing direct physical contact between the cathode and anode.

1.2 Need for Electrolyte Electrochemical Stability

From equation 1.6, high-energy-density cells require high-specific-capacity active materials and large potential differences between the positive and negative electrode.[13] Consequently, the electrolyte must either be stable in contact with the electrode interface or form a sufficiently passivating SEI to prevent continuous electrolyte breakdown.

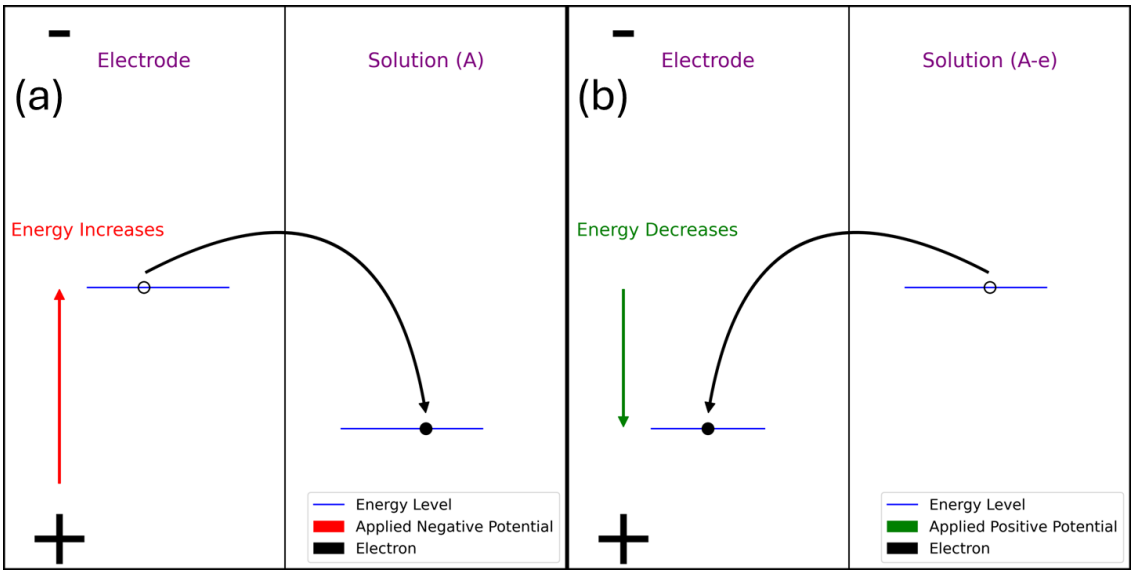

Figure 1.2: Diagram of electron transfer between the electrode and electrolyte for (a) reduction and (b) oxidation processes. By applying positive and negative potentials to the electrode, the energies of its occupied and unoccupied electronic states can be altered and electrochemical reactions at the interfaces induced.

Figure 1.2 shows the electron-transfer processes during reduction and oxidation. By varying the potential applied to the electrode the energies of the occupied and unoccupied electronic states may be varied. At certain potentials electron transfer between the electrode and the electrolyte becomes energetically favourable. When this electron transfer occurs between the electrode and species other than Li^+ side reactions occur. To mitigate these unwanted reactions, the energy of the electrolyte HOMOs should be lower than the energy of the LUMO states in the delithiated positive electrode, and the electrolyte LUMO energies should be should be higher than the HOMO energies in the lithiated negative electrode. Otherwise, the full potential range accessible for a given electrode pairing will not be realized due to the limited electrolyte stability.

Alternatively, the formation of a SEI from the degradation of electrolyte components such as EC can artificially widen the apparent electrochemical stability of the electrolyte.[2,14,15] The SEI prevents the electrolyte solvent and anionic components from coming into direct contact with the electrode, passivating against further electrolyte decomposition and potential electrode exfoliation.[2,15–20] However, other carbonate solvents such as propylene

carbonate (PC) and ethers do not form a good SEI to support the reversible Li^+ redox reactions, leading to electrode exfoliation of graphite electrodes.[15,21]

The salt concentration of the electrolyte heavily impacts the nature of solvation structures in the electrolyte[22,23] and the composition of the SEIs that form on the electrodes.[11] Thus varying salt concentration may be a promising route by which to facilitate the use of high voltage cathode materials.

Increasing salt concentration results in a decrease in the number of free solvent molecules and an increase in the number of anions directly coordinated to Li^+. Improved solvent electrochemical stability is observed in more concentrated electrolytes because their solvation structures alter the electronic structure of the electrolyte species and the chemistry of passivating SEIs.

1.3 Importance of Electrolyte Solvation Structure

To realise widespread adoption of high voltage cathode materials, the electrochemical stability of the electrolyte must be improved. Solvation structures refer to the specific arrangement of solvent molecules and anions around Li^+ in the electrolyte. It influences how Li^+ ions are transported and interact with the electrode surfaces as well as the electronic structure of the electrolyte. It directly affects the desolvation process where Li^+ ions shed the species coordinating them before intercalating into the electrode material. This process influences the formation and characteristics of the electrode's performance[24–37] and the composition, thickness and morphology of the SEI that forms.[38–41] Li^+ interacts strongly with carbonate molecules in the electrolyte via their carbonyl oxygen.[42–45] Li^+ ions are typically coordinated with four ions/molecules in an electrolyte. In more dilute electrolytes, the Li salt fully dissociates and Li^+ is solvated by four solvent molecules. These environments are referred to as a solvent separated ion pairs (SSIP). In the case of $LiPF_6$ in a mixture of EC and EMC, as salt concentration increases hexafluorophosphate (PF_6^-) appears amongst the four species coordinating to Li^+. Environments where Li^+ are solvated by a single PF_6^- and three solvent molecules are known as a contact ion pairs (CIP). Aggregates (AGG) form when Li^+ is solvated by two or more PF_6^- ions. By adjusting the salt concentration of the electrolyte SEI compositions and electrolyte electronic structure may be tailored to facilitate the use of high voltage cathode materials.

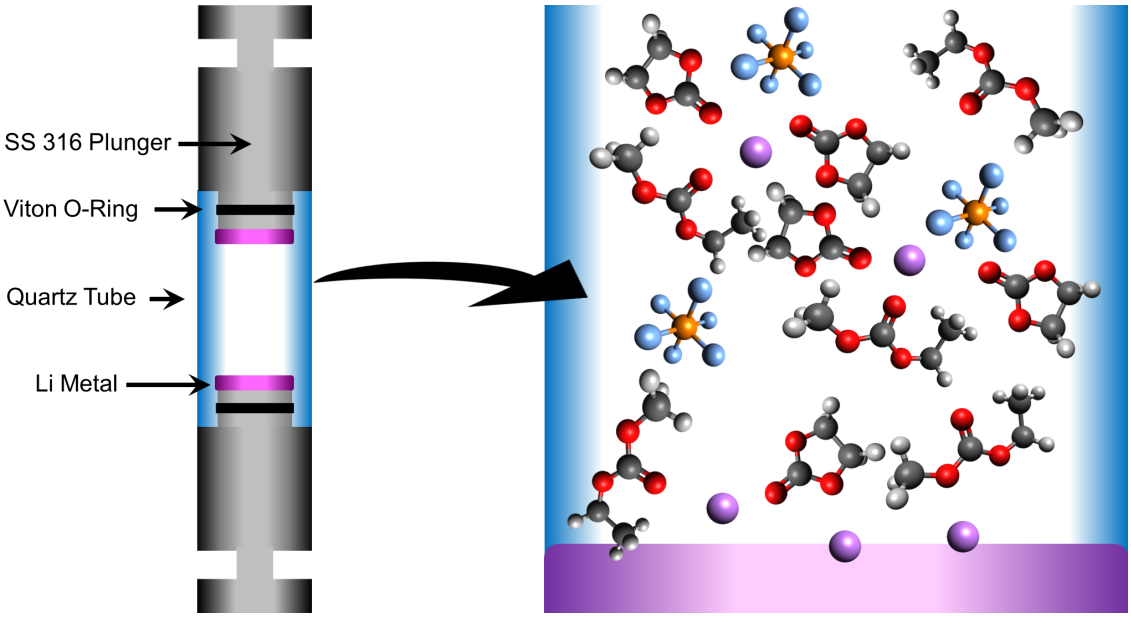

Figure 1.3: Schematic of the optical cell used for Raman spectroscopy in Chapter 4 detailing the coordination of Li^+ by EC and EMC via their carbonyl oxygens. At higher salt concentrations, PF_6^- appears in the first solvation shell resulting in the emergence of CIPs and AGGs.

1.4 Continuum Scale Electrolyte Modelling

Considering the large number of parameters that can influence LIB performance, it is costly to rely solely on experimental testing when optimizing the formulation for a LIB. Continuum scale battery modeling allows the exploration of a wide variety of system parameters with minimal time and materials expenditures. Simulation of LIBs aids the screening of different electrode and electrolyte combinations in order to find electrolyte formulations capable of facilitating the use of high voltage cathode materials. To that end a comprehensive description of the electrolyte, capable of accounting for any number of salt ions, solvent species and additives must be realised. Newman and colleagues began developing concentrated solution theory in the 1960s to better understand electrolyte behaviour.[46] This theory was later combined with their description for porous electrodes[47] as part of the Doyle-Fuller-Newman (DFN) model which is widely used to simulate LIBs.[48] Newman's concentrated solution theory is a specific case of the general MS diffusion formulation[49] which requires four main parameters for battery simulation (a) cation transference number (t_+), (b) a thermodynamic activity factor (χ_M), (c) the salt diffusion coefficient and (d) the ionic conductivity (κ). A key advantage of this approach is the ability to acquire the needed parameters experimentally[50–54] and computationally.[55–57]

Newman's concentrated solution theory works well for binary electrolytes, but commercial LIB electrolytes usually consist of lithium salts in a mixture of non-aqueous solvents which are not appropriately described by the original theory. The single-solvent assumption has been proposed rectify this issue.[54,58,59] This assumption postulates that cosolvents collectively behave as a single entity with all constituents travelling with identical velocities. However, its validity has recently been called into question.[60] More recently, efforts have been made to incorporate a second solvent term, namely EC, in 1 M $LiPF_6$ in EC:EMC based electrolytes using the framework proposed by Monroe.[61–63]

The simulation of gas and liquid phase media using the MS diffusion may be achieved if $Đ_{ij}$ and Γ_{ij} are known.[64] Little attention has been paid to the parameterization of the general MS formulation for LIB electrolytes experimentally, as no method has been proposed to extract these parameters for concentrated, multicomponent systems. The necessary parameters may be calculated computationally using MD simulations[65–67] but the accurate determination of these parameters is hindered by many issues including inaccuracies in the forcefield used, finite system size effects and the need for long simulation times. Additionally, the number of parameters needed for simulation quickly grows large as more species are considered. The key advantage of the general MS formulation over Newman's concentrated electrolyte theory is its ability to describe any number of species in any type of concentrated electrolyte.

1.5 Current LIB Electrolytes

The role of LIB electrolytes is to transport current via the migration of ions. Generally, a battery electrolyte should be electronically insulating to prevent short circuiting and ideally should not participate in side reactions at the electrode interfaces. Liquid electrolytes are common in LIBs due to their high Li^+ conductivities and the good solubility of Li salts in many solvents. To facilitate good LIB cycling at high rates, a high ion conductivity is required, which can be achieved with low viscosities and high dielectric constants of the solvent. All of these properties are affected by the nature of the electrolyte solvation structures at the molecular scale.

To achieve optimal ionic conductivities, the appropriate salt concentration must be ascertained. Too low salt concentrations will manifest low conductivites due to a deficiency of charge carries, while high salt concentrations both raise viscosity and hinder ionic transport due to increased ion/ion interactions. Viscosity is also heavily influenced by the type of solvent molecule, which in turn impacts the ability of ions to migrate and diffuse. Solvent molecules also coordinate to Li^+, and the strength of these interactions determines the magnitudes of the frictional forces that oppose Li^+ mobility. The dielectric constant is used to infer the strength of these interactions which is a measure of the ability of a solvent to dissociate the salt in solution.[68,69] Solvents possessing higher dielectric constants fully separate cation and anion pairs more easily due to stronger cation-solvent interactions. Low dielectric constants will lead to more ion association and lower ionic conductivities.[68]

Solvents in LIB electrolytes typically comprise mixtures of cyclic and linear carbonates.[70] Cyclic carbonates such as EC and PC possess high dielectric constants, while linear carbonates such as EMC and dimethyl carbonate (DMC) have much smaller dielectric constants.[71] Linear carbonates have lower melting points, low viscosities and good thermal stabilities. EC in contrast has a high melting point but is preferentially reduced at low potentials to form good SEI.[16–20] By combining cyclic and linear carbonates electrolytes with solvents facilitating high ionic conductivities, low viscosities and good SEI composition on the negative electrode can be achieved.

1 M $LiPF_6$ dissolved in such a solvent mixture is widely used as the electrolyte in LIBs. The hexafluorophosphate salt of Li exhibits good solubility in many solvents, good ionic conductivities in solution and can additionally form a passivating film on aluminium which is a common current collector for cathodes in LIBs. However, it also has poor thermal stability and reacts with trace amounts of water to form hydrofluoric acid (HF) which attacks the electrolyte and electrode surface, resulting in rapid LIB capacity fade.[72]

Layered NMC cathode materials are increasingly used in commercial LIBs owing to their

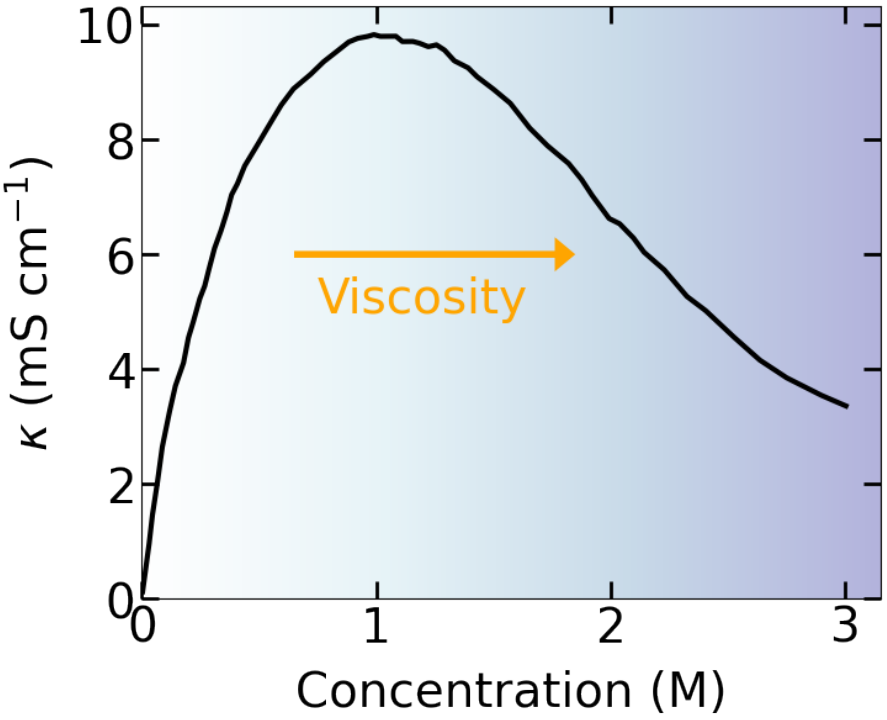

Figure 1.4: Example of the variation of ionic conductivity versus salt concentration for $LiPF_6$ in EC:EMC (3:7 w:w).[54] The optimal ionic conductivity usually lies around 1 M in commercial LIB electrolytes.

good specific capacities. Increasing Ni content increases capacity while reducing the Co content, which is both expensive and has ethical issues related to its acquisition.[6] Higher Ni contents also increase interfacial reactivities at high potentials with the electrolyte solvent, in particular EC.[9,10] The NMC layered structure is also destabilised at high potentials, resulting in oxygen release and the formation of a reduced surface layer (RSL) at the particle surface.[12,73–76] The oxygen release results in chemical oxidation of the solvent species at the cathode surface.[72,77] The RSL possesses poor ionic conductivity, which increases interfacial impedances,[12,74,78,79] that limits high cycling-rate performance. For NMC811 the onset of significant RSL formation occurs at lower potentials vs. Li/Li^+,[75,76] with the increasing amounts of reactive $^1O_2$ released resulting in chemical oxidation of solvent components of the electrolyte.[75,76,80–82]

Highly concentrated electrolytes are a promising means to combat these drawbacks, owing to the enhanced electrochemical stability they demonstrate in both aqueous[83–86] and organic[87,88] electrolytes. Whilst generally possessing improved electrochemical stabilities, highly concentrated electrolytes suffer from high viscosities and lower ionic conductivities, which limit rate capability. Locally concentrated electrolytes (LCE) have been proposed as a potential solution reaping the good electrochemical stabilities of highly concentrated electrolytes whilst maintaining the good transport properties of the more dilute

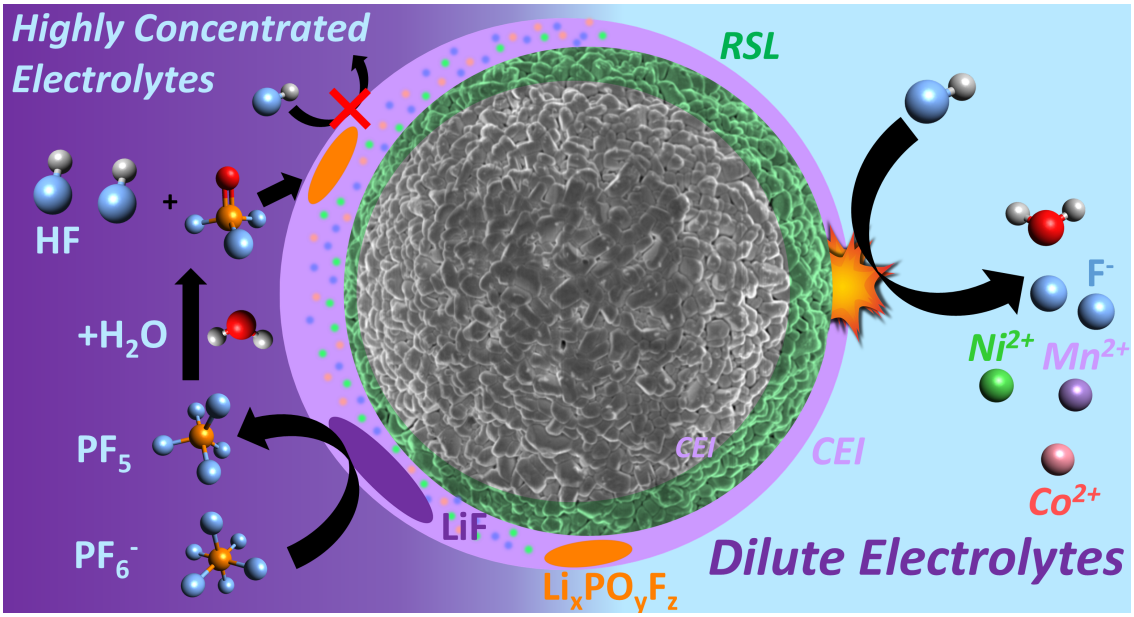

Figure 1.5: Schematic describing degradation mechanisms of $LiPF_6$ in EC:EMC (vol:vol 3:7) at NMC811 surfaces at hih potentials. A more $LiF/Li_xPO_yF_z$ rich CEI is observed to form in the more highly concentrated electrolytes, passivating against electrolyte decomposition and unwanted side reactions. Adapted with permission from Ref [11]. Copyright 2024 American Chemical Society.

electrolytes.[89–91] Optimising electrolyte formulations to balance good electrochemical stabilities at high voltage cathode surfaces, while retaining acceptable ionic conductivities to facilitate high rate performance is a challenging endeavour. Our understanding of the interplay between solvation structure, transport properties and electrochemical stability must be improved to facilitate the widespread adoption of high voltage cathode materials in electric vehicles and grid-scale energy storage systems.

1.6 Thesis Outline

This thesis will focus on (a) the effect of salt concentration on electrolyte stability at charged NMC811 interfaces, (b) relating electrolyte transport properties observed on the molecular scale to electrolyte behaviour under an applied current and (c) the relationship between electrolyte solvation structure and observed electrochemical stabilities. The electrolyte system of interest in this thesis is $LiPF_6$ in EC:EMC (vol:vol 3:7). Chapter 2 outlines the basics of the experimental and computational techniques used herein. Chapter 3 investigates the influence of $LiPF_6$ salt concentration on electrolyte stability at charged NMC811 interfaces. Reaction mechanisms are proposed to account for the observed changes in CEI composition, electrolyte degradation, RSL formation and TM dissolution with increasing salt concentration. It was determined that increasing salt concentration results in a more inorganic, $LiF/Li_xPO_yF_z$ rich CEI, passivating the surface against continuous solvent degradation resulting in improved electrochemical stabilities. HF forms in the highly concentrated electrolytes from the reaction of PF_6^- with trace amounts of water, also forming soluble PO_yF_z species. The thicker, $LiF/Li_xPO_yF_z$ rich CEI prevents acidic species such as HF from attacking the electrode surface resulting in less TM dissolution during cycling. This results in a buildup of HF in the electrolyte, which attacks components in the GF separators, resulting in increased separator degradation in the more highly concentrated electrolytes. The protection of the surface by the CEI resulted in thinner RSLs with lower charge transfer resistance (R_{ct}) values. The results also indicate that both the CEI and the electrolyte salt concentration contribute to improved electrochemical stability. Chapter 4 focuses on calculating $Đ_{ij}$ and Γ_{ij} values from MD and testing them against measured concentration profiles in the electrolyte under an applied current. The calculated $Đ_{ij}$ and Γ_{ij} accurately describe the transport behaviour of multi-component electrolytes under an applied current. These findings provide fundamental insight into the simulation of LIB electrolytes on the continuum scale, which will aid the development and optimization of LIB electrolytes for use with high voltage cathode materials. Chapter 5 investigates the relationship between electrolyte solvation structure and electrochemical stability. MD simulations reveal a decrease in the number of free EC and EMC molecules with increasing salt concentration, with almost all solvent molecules involved in direct Li^+ coordination. The number of PF_6^- ions in the first solvation shell increases owing to the higher salt concentration. Raman spectroscopy supports the disappearance of free solvent molecules with increasing salt concentration. The first peak in the XAS O K-edge of the solvent molecules shifts to higher excitation energies due to increasing solvent coordination from Li^+ ions. DFT density of states (DOS) calculations of the electrolytes demonstrate increasing overlap in terms of energy and density between the HOMO of PF_6^- ions and the solvent molecules, indicating PF_6^- becomes easier to

oxidise in the more highly concentrated electrolytes relative to the solvent molecules. This accounts for the improved electrochemical stability and CEI composition observed in Chapter 3. EC is observed to dominate the LUMO states in the electrolyte at all salt concentrations, rationalizing why it is reduced first on negative electrodes during SEI formation in LIBs. This new understanding of the effect of electrolyte salt concentration on electrochemical stability and CEI composition will aid the adoption of high voltage cathode materials in electric vehicles and grid-scale energy storage solutions.

Bibliography

[1] Department for Energy Security and Net Zero, "Net Zero Government Initiative," 2023.

[2] J. B. Goodenough and Y. Kim, "Challenges for rechargeable Li batteries," 2010.

[3] A. Barré, B. Deguilhem, S. Grolleau, M. Gérard, F. Suard, and D. Riu, "A review on lithium-ion battery ageing mechanisms and estimations for automotive applications," 2013.

[4] Y. Nishi, "Lithium ion secondary batteries; Past 10 years and the future," *Journal of Power Sources*, vol. 100, no. 1-2, 2001.

[5] N. Nitta, F. Wu, J. T. Lee, and G. Yushin, "Li-ion battery materials: Present and future," 2015.

[6] Amnesty International, "Democratic Republic of Congo: "This is what we die for": Human rights abuses in the Democratic Republic of the Congo power the global trade in cobalt," 2016.

[7] J. Liu, J. Wang, Y. Ni, K. Zhang, F. Cheng, and J. Chen, "Recent breakthroughs and perspectives of high-energy layered oxide cathode materials for lithium ion batteries," 2021.

[8] Y. Xia, J. Zheng, C. Wang, and M. Gu, "Designing principle for Ni-rich cathode materials with high energy density for practical applications," 2018.

[9] W. M. Dose, I. Temprano, J. P. Allen, E. Björklund, C. A. O'Keefe, W. Li, B. L. Mehdi, R. S. Weatherup, M. F. De Volder, and C. P. Grey, "Electrolyte Reactivity at the Charged Ni-Rich Cathode Interface and Degradation in Li-Ion Batteries," *ACS Applied Materials and Interfaces*, vol. 14, no. 11, 2022.

[10] W. M. Dose, W. Li, I. Temprano, C. A. O'Keefe, B. Layla Mehdi, M. F. L. De Volder, and C. P. Grey, "Onset Potential for Electrolyte Oxidation and Ni-Rich Cathode Degradation in Lithium-Ion Batteries," *ACS Energy Letters*, vol. 7, pp. 3524–3530, 9 2022.

[11] C. M. E. Phelan, E. Bjorklund, J. Singh, M. Fraser, P. N. Didwal, G. J. Rees, Z. Ruff, P. Ferrer, D. C. Grinter, C. P. Grey, and others, "Role of Salt Concentration in Stabilizing Charged Ni-Rich Cathode Interfaces in Li-Ion Batteries," *Chemistry of Materials*, vol. 36, no. 7, pp. 3334–3344, 2024.

[12] E. Björklund, C. Xu, W. M. Dose, C. G. Sole, P. K. Thakur, T. L. Lee, M. F. De Volder, C. P. Grey, and R. S. Weatherup, "Cycle-Induced Interfacial Degradation and Transition-Metal Cross-Over in LiNi0.8Mn0.1Co0.1O2-Graphite Cells," *Chemistry of Materials*, vol. 34, no. 5, 2022.

[13] C. Liu, Z. G. Neale, and G. Cao, "Understanding electrochemical potentials of cathode materials in rechargeable batteries," 2016.

[14] M. Gauthier, T. J. Carney, A. Grimaud, L. Giordano, N. Pour, H. H. Chang, D. P. Fenning, S. F. Lux, O. Paschos, C. Bauer, F. Maglia, S. Lupart, P. Lamp, and Y. Shao-Horn, "Electrode-Electrolyte Interface in Li-Ion Batteries: Current Understanding and New Insights," 2015.

[15] H. Cheng, Q. Sun, L. Li, Y. Zou, Y. Wang, T. Cai, F. Zhao, G. Liu, Z. Ma, W. Wahyudi, Q. Li, and J. Ming, "Emerging Era of Electrolyte Solvation Structure and Interfacial Model in Batteries," 2022.

[16] G. V. Zhuang, K. Xu, H. Yang, T. R. Jow, and P. N. Ross, "Lithium ethylene dicarbonate identified as the primary product of chemical and electrochemical reduction of EC in 1.2 M LiPF 6/EC:EMC electrolyte," *Journal of Physical Chemistry B*, vol. 109, no. 37, 2005.

[17] D. Aurbach, B. Markovsky, A. Shechter, Y. Ein-Eli, and H. Cohen, "A Comparative Study of Synthetic Graphite and Li Electrodes in Electrolyte Solutions Based on Ethylene Carbonate-Dimethyl Carbonate Mixtures," *Journal of The Electrochemical Society*, vol. 143, no. 12, 1996.

[18] D. Aurbach, Y. Ein-Eli, B. Markovsky, A. Zaban, S. Luski, Y. Carmeli, and H. Yamin, "The Study of Electrolyte Solutions Based on Ethylene and Diethyl Carbonates for Rechargeable Li Batteries: II . Graphite Electrodes," *Journal of The Electrochemical Society*, vol. 142, no. 9, 1995.

[19] D. Aurbach, Y. Gofer, M. Ben-Zion, and P. Aped, "The behaviour of lithium electrodes in propylene and ethylene carbonate: Te major factors that influence Li cycling efficiency," *Journal of Electroanalytical Chemistry*, vol. 339, no. 1-2, 1992.

[20] A. Kominato, E. Yasukawa, N. Sato, T. Ijuuin, H. Asahina, and S. Mori, "Analysis of surface films on lithium in various organic electrolytes," *Journal of Power Sources*, vol. 68, no. 2, 1997.

[21] D. Aurbach, M. D. Levi, E. Levi, and A. Schechter, "Failure and stabilization mechanisms of graphite electrodes," *Journal of Physical Chemistry B*, vol. 101, no. 12, 1997.

[22] L. Zhang and Y. Chen, "Electrolyte solvation structure as a stabilization mechanism for electrodes," *Energy Materials*, vol. 1, no. 1, 2022.

[23] J. Zheng, P. Yan, D. H. Mei, M. H. Engelhard, S. S. Cartmell, B. J. Polzin, C. M. Wang, J. G. Zhang, and W. Xu, "Highly Stable Operation of Lithium Metal Batteries Enabled by the Formation of a Transient High-Concentration Electrolyte Layer," *Advanced Energy Materials*, vol. 6, no. 8, 2016.

[24] J. Ming, M. Li, P. Kumar, A. Y. Lu, W. Wahyudi, and L. J. Li, "Redox Species-Based Electrolytes for Advanced Rechargeable Lithium Ion Batteries," *ACS Energy Letters*, vol. 1, no. 3, 2016.

[25] J. Ming, Z. Cao, W. Wahyudi, M. Li, P. Kumar, Y. Wu, J. Y. Hwang, M. N. Hedhili, L. Cavallo, Y. K. Sun, and L. J. Li, "New Insights on Graphite Anode Stability in Rechargeable Batteries: Li Ion Coordination Structures Prevail over Solid Electrolyte Interphases," *ACS Energy Letters*, vol. 3, no. 2, 2018.

[26] J. Ming, Z. Cao, Q. Li, W. Wahyudi, W. Wang, L. Cavallo, K. J. Park, Y. K. Sun, and H. N. Alshareef, "Molecular-Scale Interfacial Model for Predicting Electrode Performance in Rechargeable Batteries," *ACS Energy Letters*, vol. 4, no. 7, 2019.

[27] J. Ming, Z. Cao, Y. Wu, W. Wahyudi, W. Wang, X. Guo, L. Cavallo, J. Y. Hwang, A. Shamim, L. J. Li, Y. K. Sun, and H. N. Alshareef, "New Insight on the Role of Electrolyte Additives in Rechargeable Lithium Ion Batteries," *ACS Energy Letters*, vol. 4, no. 11, 2019.

[28] Q. Li, Z. Cao, W. Wahyudi, G. Liu, G. T. Park, L. Cavallo, T. D. Anthopoulos, L. Wang, Y. K. Sun, H. N. Alshareef, and J. Ming, "Unraveling the New Role of an Ethylene Carbonate Solvation Shell in Rechargeable Metal Ion Batteries," *ACS Energy Letters*, vol. 6, no. 1, 2021.

[29] G. Liu, Z. Cao, L. Zhou, J. Zhang, Q. Sun, J. Y. Hwang, L. Cavallo, L. Wang, Y. K. Sun, and J. Ming, "Additives Engineered Nonflammable Electrolyte for Safer Potassium Ion Batteries," *Advanced Functional Materials*, vol. 30, no. 43, 2020.

[30] J. Zhang, Z. Cao, L. Zhou, G. Liu, G. T. Park, L. Cavallo, L. Wang, H. N. Alshareef, Y. K. Sun, and J. Ming, "Model-Based Design of Graphite-Compatible Electrolytes in Potassium-Ion Batteries," *ACS Energy Letters*, vol. 5, no. 8, 2020.

[31] Y. Zou, Y. Shen, Y. Wu, H. Xue, Y. Guo, G. Liu, L. Wang, and J. Ming, "A Designed Durable Electrolyte for High-Voltage Lithium-Ion Batteries and Mechanism Analysis," *Chemistry - A European Journal*, vol. 26, no. 35, 2020.

[32] Q. Sun, Z. Cao, J. Zhang, H. Cheng, J. Zhang, Q. Li, H. Ming, G. Liu, and J. Ming, "Metal Catalyst to Construct Carbon Nanotubes Networks on Metal Oxide Microparticles towards Designing High-Performance Electrode for High-Voltage Lithium-Ion Batteries," *Advanced Functional Materials*, vol. 31, no. 22, 2021.

[33] L. Zhou, Z. Cao, J. Zhang, Q. Sun, Y. Wu, W. Wahyudi, J. Y. Hwang, L. Wang, L. Cavallo, Y. K. Sun, H. N. Alshareef, and J. Ming, "Engineering Sodium-Ion Solvation Structure to Stabilize Sodium Anodes: Universal Strategy for Fast-Charging and Safer Sodium-Ion Batteries," *Nano Letters*, vol. 20, no. 5, 2020.

[34] W. Wahyudi, V. Ladelta, L. Tsetseris, M. M. Alsabban, X. Guo, E. Yengel, H. Faber, B. Adilbekova, A. Seitkhan, A. H. Emwas, M. N. Hedhili, L. J. Li, V. Tung, N. Hadjichristidis, T. D. Anthopoulos, and J. Ming, "Lithium-Ion Desolvation Induced by Nitrate Additives Reveals New Insights into High Performance Lithium Batteries," *Advanced Functional Materials*, vol. 31, no. 23, 2021.

[35] L. Zhou, Z. Cao, J. Zhang, H. Cheng, G. Liu, G. T. Park, L. Cavallo, L. Wang, H. N. Alshareef, Y. K. Sun, and J. Ming, "Electrolyte-Mediated Stabilization of High-Capacity Micro-Sized Antimony Anodes for Potassium-Ion Batteries," *Advanced Materials*, vol. 33, no. 8, 2021.

[36] Y. Zou, Z. Cao, J. Zhang, W. Wahyudi, Y. Wu, G. Liu, Q. Li, H. Cheng, D. Zhang, G. T. Park, L. Cavallo, T. D. Anthopoulos, L. Wang, Y. K. Sun, and J. Ming, "Interfacial Model Deciphering High-Voltage Electrolytes for High Energy Density, High Safety, and Fast-Charging Lithium-Ion Batteries," *Advanced Materials*, vol. 33, no. 43, 2021.

[37] S. H. Lee, J. Y. Hwang, J. Ming, Z. Cao, H. A. Nguyen, H. G. Jung, J. Kim, and Y. K. Sun, "Toward the Sustainable Lithium Metal Batteries with a New Electrolyte Solvation Chemistry," *Advanced Energy Materials*, vol. 10, no. 20, 2020.

[38] X. Q. Zhang, X. Chen, L. P. Hou, B. Q. Li, X. B. Cheng, J. Q. Huang, and Q. Zhang, "Regulating Anions in the Solvation Sheath of Lithium Ions for Stable Lithium Metal Batteries," *ACS Energy Letters*, vol. 4, no. 2, 2019.

[39] W. Deng, W. Dai, X. Zhou, Q. Han, W. Fang, N. Dong, B. He, and Z. Liu, "Competitive Solvation-Induced Concurrent Protection on the Anode and Cathode toward a 400 Wh kg-1Lithium Metal Battery," *ACS Energy Letters*, vol. 6, no. 1, 2021.

[40] J. Holoubek, M. Yu, S. Yu, M. Li, Z. Wu, D. Xia, P. Bhaladhare, M. S. Gonzalez, T. A. Pascal, P. Liu, and Z. Chen, "An All-Fluorinated Ester Electrolyte for Stable High-Voltage Li Metal Batteries Capable of Ultra-Low-Temperature Operation," *ACS Energy Letters*, vol. 5, no. 5, 2020.

[41] H. Yang, X. Chen, N. Yao, N. Piao, Z. Wang, K. He, H. M. Cheng, and F. Li, "Dissolution-Precipitation Dynamics in Ester Electrolyte for High-Stability Lithium Metal Batteries," *ACS Energy Letters*, vol. 6, no. 4, 2021.

[42] J. W. Smith, R. K. Lam, A. T. Sheardy, O. Shih, A. M. Rizzuto, O. Borodin, S. J. Harris, D. Prendergast, and R. J. Saykally, "X-Ray absorption spectroscopy of LiBF4 in propylene carbonate: A model lithium ion battery electrolyte," *Physical Chemistry Chemical Physics*, vol. 16, no. 43, 2014.

[43] T. Hou, K. D. Fong, J. Wang, and K. A. Persson, "The solvation structure, transport properties and reduction behavior of carbonate-based electrolytes of lithium-ion batteries," *Chemical Science*, vol. 12, no. 44, 2021.

[44] N. Kumar and J. M. Seminario, "Lithium-ion model behavior in an ethylene carbonate electrolyte using molecular dynamics," *Journal of Physical Chemistry C*, vol. 120, no. 30, 2016.

[45] B. Ravikumar, M. Mynam, and B. Rai, "Effect of Salt Concentration on Properties of Lithium Ion Battery Electrolytes: A Molecular Dynamics Study," *Journal of Physical Chemistry C*, vol. 122, no. 15, 2018.

[46] J. Newman and T. W. Chapman, "Restricted diffusion in binary solutions," *AIChE Journal*, vol. 19, no. 2, 1973.

[47] J. Newman and W. Tiedemann, "Porous-electrode theory with battery applications," 1975.

[48] M. Doyle, T. F. Fuller, and J. Newman, "Modeling of Galvanostatic Charge and Discharge of the Lithium/Polymer/Insertion Cell," *Journal of The Electrochemical Society*, vol. 140, no. 6, 1993.

[49] J. Newman and K. E. Thomas-Alyea, *Electrochemical systems. Third edition*. 2004.

[50] J. Fawdon, J. Ihli, F. L. Mantia, and M. Pasta, "Characterising lithium-ion electrolytes via operando Raman microspectroscopy," *Nature Communications*, vol. 12, no. 1, 2021.

[51] J. Fawdon, G. J. Rees, F. La Mantia, and M. Pasta, "Insights into the Transport and Thermodynamic Properties of a Bis(fluorosulfonyl)imide-Based Ionic Liquid

Electrolyte for Battery Applications," *Journal of Physical Chemistry Letters*, vol. 13, no. 7, 2022.

[52] J. Zhao, B. Jagger, L. F. Olbrich, J. Ihli, S. Dhir, M. Zyskin, X. Ma, and M. Pasta, "Transport and Thermodynamic Properties of KFSI in TEP by Operando Raman Gradient Analysis," *ACS Energy Letters*, vol. 9, no. 4, 2024.

[53] A. A. Wang, A. B. Gunnarsdóttir, J. Fawdon, M. Pasta, C. P. Grey, and C. W. Monroe, "Potentiometric MRI of a Superconcentrated Lithium Electrolyte: Testing the Irreversible Thermodynamics Approach," *ACS Energy Letters*, vol. 6, no. 9, 2021.

[54] J. Landesfeind and H. A. Gasteiger, "Temperature and Concentration Dependence of the Ionic Transport Properties of Lithium-Ion Battery Electrolytes," *Journal of The Electrochemical Society*, vol. 166, no. 14, 2019.

[55] S. T. Dix, J. S. Lowe, M. R. Avei, and T. R. Garrick, "Leveraging Molecular Dynamics to Improve Porous Electrode Theory Modeling Predictions of Lithium-Ion Battery Cells," *Journal of The Electrochemical Society*, vol. 170, no. 8, 2023.

[56] F. Hanke, N. Modrow, R. L. C. Akkermans, I. Korotkin, F. C. Mocanu, V. A. Neufeld, and M. Veit, "Multi-Scale Electrolyte Transport Simulations for Lithium Ion Batteries," *Journal of The Electrochemical Society*, vol. 167, no. 1, 2020.

[57] B. Ghalami Choobar, H. Modarress, R. Halladj, and S. Amjad-Iranagh, "Multiscale Investigation on Electrolyte Systems of [(Solvent + Additive) + LiPF6] for Application in Lithium-Ion Batteries," *Journal of Physical Chemistry C*, vol. 123, no. 36, 2019.

[58] Y. Ugata, Y. Chen, S. Miyazaki, S. Sasagawa, K. Ueno, M. Watanabe, and K. Dokko, "High-concentration LiPF6/sulfone electrolytes: structure, transport properties, and battery application," *Physical Chemistry Chemical Physics*, vol. 25, no. 43, 2023.

[59] H. K. Bergstrom, K. D. Fong, and B. D. McCloskey, "Interfacial Effects on Transport Coefficient Measurements in Li-ion Battery Electrolytes," *Journal of The Electrochemical Society*, vol. 168, no. 6, 2021.

[60] A. A. Wang, S. Greenbank, G. Li, D. A. Howey, and C. W. Monroe, "Current-driven solvent segregation in lithium-ion electrolytes," *Cell Reports Physical Science*, vol. 3, no. 9, 2022.

[61] C. W. Monroe, "Does Oxygen Transport Affect the Cell Voltages of Metal/Air Batteries?," *Journal of The Electrochemical Society*, vol. 164, no. 11, 2017.

[62] R. Li, S. O'Kane, A. Wang, T. Jung, N. Kirkaldy, M. Marinescu, C. W. Monroe, and G. J. Offer, "Lithium-ion battery performance model including solvent segregation effects," *arXiv preprint arXiv:2311.05467*, 2023.

[63] T. Jung, A. A. Wang, and C. W. Monroe, "Overpotential from Cosolvent Imbalance in Battery Electrolytes: LiPF6 in EMC:EC," *ACS Omega*, vol. 8, no. 23, 2023.

[64] Ross Taylor and R. Krishna, *Multicomponent mass transfer I. Theory*. 1993.

[65] R. Krishna and J. M. Van Baten, "The darken relation for multicomponent diffusion in liquid mixtures of linear alkanes: An investigation using Molecular Dynamics (MD) simulations," *Industrial and Engineering Chemistry Research*, vol. 44, no. 17, 2005.

[66] X. Liu, T. J. Vlugt, and A. Bardow, "Predictive Darken equation for Maxwell-Stefan diffusivities in multicomponent mixtures," *Industrial and Engineering Chemistry Research*, vol. 50, no. 17, 2011.

[67] R. Fingerhut, G. Herres, and J. Vrabec, "Thermodynamic factor of quaternary mixtures from Kirkwood–Buff integration," *Molecular Physics*, vol. 118, no. 6, 2020.

[68] E. R. Logan, E. M. Tonita, K. L. Gering, J. Li, X. Ma, L. Y. Beaulieu, and J. R. Dahn, "A Study of the Physical Properties of Li-Ion Battery Electrolytes Containing Esters," *Journal of The Electrochemical Society*, vol. 165, no. 2, 2018.

[69] J. Self, B. M. Wood, N. N. Rajput, and K. A. Persson, "The Interplay between Salt Association and the Dielectric Properties of Low Permittivity Electrolytes: The Case of LiPF6 and LiAsF6 in Dimethyl Carbonate," *Journal of Physical Chemistry C*, vol. 122, no. 4, 2018.

[70] J. Kalhoff, G. G. Eshetu, D. Bresser, and S. Passerini, "Safer electrolytes for lithium-ion batteries: State of the art and perspectives," *ChemSusChem*, vol. 8, no. 13, 2015.

[71] D. S. Hall, J. Self, and J. R. Dahn, "Dielectric Constants for Quantum Chemistry and Li-Ion Batteries: Solvent Blends of Ethylene Carbonate and Ethyl Methyl Carbonate," *Journal of Physical Chemistry C*, vol. 119, no. 39, 2015.

[72] B. L. Rinkel, D. S. Hall, I. Temprano, and C. P. Grey, "Electrolyte oxidation pathways in lithium-ion batteries," *Journal of the American Chemical Society*, vol. 142, no. 35, 2020.

[73] L. Giordano, P. Karayaylali, Y. Yu, Y. Katayama, F. Maglia, S. Lux, and Y. Shao-Horn, "Chemical Reactivity Descriptor for the Oxide-Electrolyte Interface in Li-Ion Batteries," *Journal of Physical Chemistry Letters*, vol. 8, no. 16, 2017.

[74] F. Lin, I. M. Markus, D. Nordlund, T. C. Weng, M. D. Asta, H. L. Xin, and M. M. Doeff, "Surface reconstruction and chemical evolution of stoichiometric layered cathode materials for lithium-ion batteries," *Nature communications*, vol. 5, 2014.

[75] R. Jung, M. Metzger, F. Maglia, C. Stinner, and H. A. Gasteiger, " Oxygen Release and Its Effect on the Cycling Stability of LiNi x Mn y Co z O 2 (NMC) Cathode Materials for Li-Ion Batteries ," *Journal of The Electrochemical Society*, vol. 164, no. 7, 2017.

[76] D. Streich, C. Erk, A. Guéguen, P. Müller, F. F. Chesneau, and E. J. Berg, "Operando Monitoring of Early Ni-mediated Surface Reconstruction in Layered Lithiated Ni-Co-Mn Oxides," *Journal of Physical Chemistry C*, vol. 121, no. 25, 2017.

[77] B. L. D. Rinkel, J. P. Vivek, N. Garcia-Araez, and C. P. Grey, "Two electrolyte decomposition pathways at nickel-rich cathode surfaces in lithium-ion batteries," *Energy & Environmental Science*, vol. 15, no. 8, pp. 3416–3438, 2022.

[78] D. Dees, E. Gunen, D. Abraham, A. Jansen, and J. Prakash, "Alternating Current Impedance Electrochemical Modeling of Lithium-Ion Positive Electrodes," *Journal of The Electrochemical Society*, vol. 152, no. 7, p. A1409, 2005.

[79] W. M. Dose, J. K. Morzy, A. Mahadevegowda, C. Ducati, C. P. Grey, and M. F. De Volder, "The influence of electrochemical cycling protocols on capacity loss in nickel-rich lithium-ion batteries," *Journal of Materials Chemistry A*, vol. 9, no. 41, 2021.

[80] R. Jung, M. Metzger, F. Maglia, C. Stinner, and H. A. Gasteiger, "Chemical versus electrochemical electrolyte oxidation on NMC111, NMC622, NMC811, LNMO, and conductive carbon," *Journal of Physical Chemistry Letters*, vol. 8, no. 19, 2017.

[81] A. T. Freiberg, M. K. Roos, J. Wandt, R. De Vivie-Riedle, and H. A. Gasteiger, "Singlet Oxygen Reactivity with Carbonate Solvents Used for Li-Ion Battery Electrolytes," *Journal of Physical Chemistry A*, vol. 122, no. 45, 2018.

[82] J. Wandt, A. T. Freiberg, A. Ogrodnik, and H. A. Gasteiger, "Singlet oxygen evolution from layered transition metal oxide cathode materials and its implications for lithium-ion batteries," *Materials Today*, vol. 21, no. 8, 2018.

[83] L. Suo, O. Borodin, T. Gao, M. Olguin, J. Ho, X. Fan, C. Luo, C. Wang, and K. Xu, ""Water-in-salt" electrolyte enables high-voltage aqueous lithium-ion chemistries," *Science*, vol. 350, no. 6263, 2015.

[84] L. Suo, O. Borodin, W. Sun, X. Fan, C. Yang, F. Wang, T. Gao, Z. Ma, M. Schroeder, A. von Cresce, S. M. Russell, M. Armand, A. Angell, K. Xu, and C. Wang, "Ad-

vanced High-Voltage Aqueous Lithium-Ion Battery Enabled by “Water-in-Bisalt” Electrolyte,” *Angewandte Chemie - International Edition*, vol. 55, no. 25, 2016.

[85] L. Suo, O. Borodin, Y. Wang, X. Rong, W. Sun, X. Fan, S. Xu, M. A. Schroeder, A. V. Cresce, F. Wang, C. Yang, Y. S. Hu, K. Xu, and C. Wang, ““Water-in-Salt” Electrolyte Makes Aqueous Sodium-Ion Battery Safe, Green, and Long-Lasting,” *Advanced Energy Materials*, vol. 7, no. 21, 2017.

[86] M. R. Lukatskaya, J. I. Feldblyum, D. G. Mackanic, F. Lissel, D. L. Michels, Y. Cui, and Z. Bao, “Concentrated mixed cation acetate "water-in-salt" solutions as green and low-cost high voltage electrolytes for aqueous batteries,” *Energy and Environmental Science*, vol. 11, no. 10, 2018.

[87] J. Wang, Y. Yamada, K. Sodeyama, C. H. Chiang, Y. Tateyama, and A. Yamada, “Superconcentrated electrolytes for a high-voltage lithium-ion battery,” *Nature Communications*, vol. 7, 2016.

[88] R. Petibon, C. P. Aiken, L. Ma, D. Xiong, and J. R. Dahn, “The use of ethyl acetate as a sole solvent in highly concentrated electrolyte for Li-ion batteries,” *Electrochimica Acta*, vol. 154, 2015.

[89] W. Dai, N. Dong, Y. Xia, S. Chen, H. Luo, Y. Liu, and Z. Liu, “Localized concentrated high-concentration electrolyte enhanced stability and safety for high voltage Li-ion batteries,” *Electrochimica Acta*, vol. 320, 2019.

[90] X. Cao, H. Jia, W. Xu, and J.-G. Zhang, “Review—Localized High-Concentration Electrolytes for Lithium Batteries,” *Journal of The Electrochemical Society*, vol. 168, no. 1, 2021.

[91] S. Chen, J. Zheng, D. Mei, K. S. Han, M. H. Engelhard, W. Zhao, W. Xu, J. Liu, and J. G. Zhang, “High-Voltage Lithium-Metal Batteries Enabled by Localized High-Concentration Electrolytes,” *Advanced Materials*, vol. 30, no. 21, 2018.

Chapter 2

Experimental and Computational Methods

This chapter will discuss the basics of the experimental and computational techniques employed in this thesis. The use of each technique in the context of this thesis will also be provided.

2.1 Confocal Raman Microscpectroscopy

Confocal microscopy was invented in 1957 by Marvin Minsky, an American physicist and computer scientist. Confocal microscopy is a powerful imaging technique which provides high-resolution measurements of samples by using a pinhole to eliminate out-of-focus light. This results in sharper and clearer measurements compared to traditional microscopy techniques. Raman spectroscopy is a non-destructive technique used to study vibrational, rotational, and other low-frequency modes in a system.[1–3].

As demonstrated in Figure 2.1, the sample is illuminated with a monochromatic light source such as a laser. The laser passes through a beam splitter then onto the objective lens. The beam is then redirected from the vertical to the horizontal axis using a 90^o mirror where it strikes the optical cell through the laser transparent quartz window. The incident photons interact with molecular bonds, temporarily promoting the molecule to an excited state. The molecule then relaxes back to its ground state, re-emitting the photon. In "Rayleigh scattering" the molecule relaxes to the same mode from which it was excited. Occasionally, the molecule relaxes to a different mode and consequently emits a photon with a different wavelength to the incident light. This is called "Raman scattering". If the molecule relaxes to a mode with a higher energy than its initial mode, the energy of the emitted photon is smaller. This is called Stokes Raman scattering. Conversely, if the molecule relaxes to a mode with a lower energy than its initial one, the energy of the emitted photon is larger. This is called Anti-Stokes Raman scattering. The probability of Stokes scattering is the larger of the two, and results in more intense Raman peaks.[4] Molecules are only Raman active if they exhibit anisotropic polarizability i.e. Raman scattering only occurs if there is a change in polarizability of the molecule between the initial and final states. The emitted photons are reflected back through the objective lens and the beam splitter. The Rayleigh rejection filter removes the photons emitted due to Rayleigh scattering. The Raman photons are then directed onto a diffraction grating and diffracted onto a charged coupled device (CCD) camera for detection. The intensity of the observed Raman peak is given by:

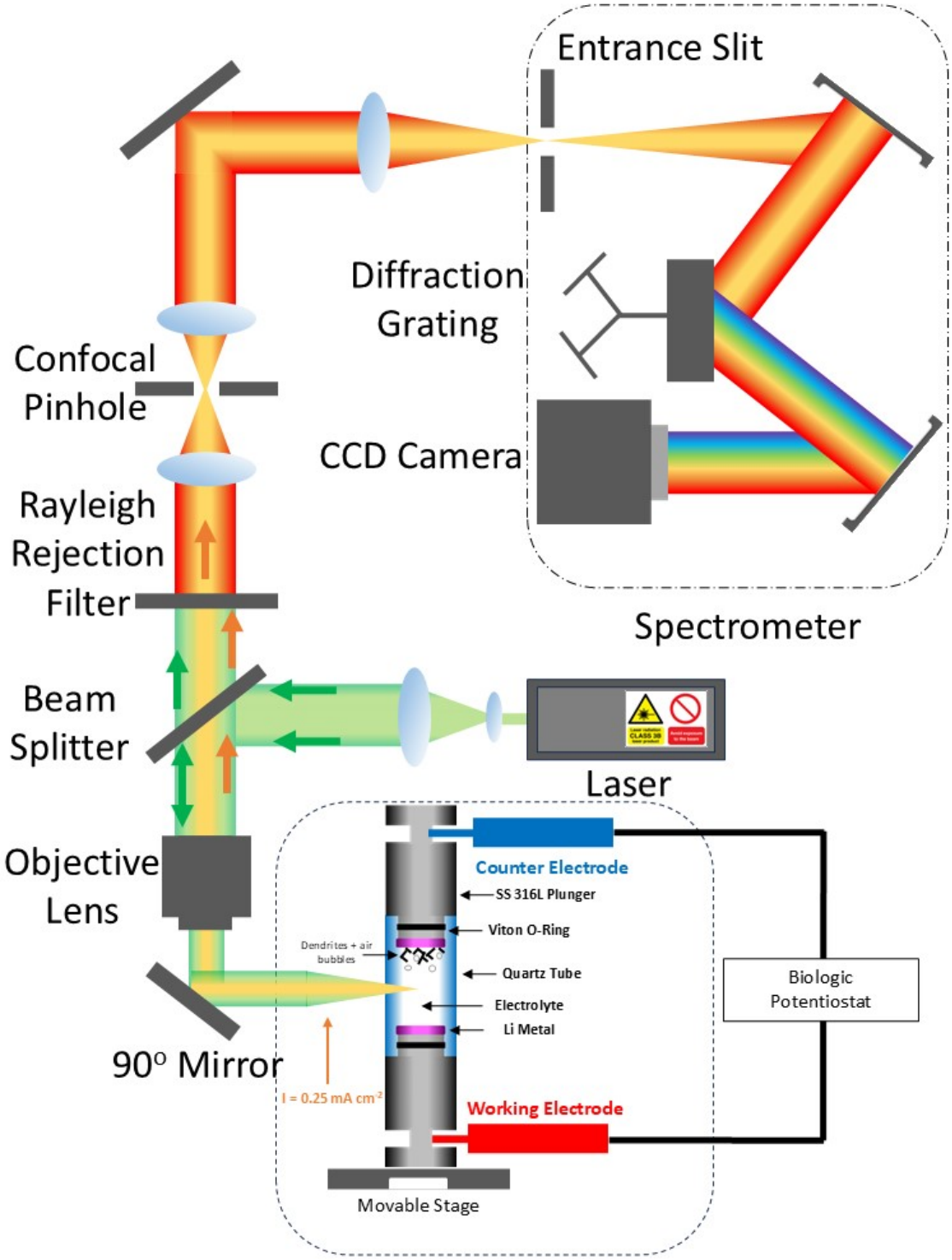

Figure 2.1: Schematic representation of the experimental setup for operando raman measurements used during concentration profiling.

$$I = c_i K_l \alpha^2 \omega^{-4} \tag{2.1}$$

I is the intensity of the Raman peak. c_i is the concentration of the molecule, K_l is a constant depending on factors such as the laser wavelength, the aperture of the optical system and the refractive index of the sample, α is the polarizability of the molecule i.e. representing its ability to be polarized by an external electric field. ω is the frequency of the incident light. Raman shifts are typically reported in wavenumbers ($\Delta\nu$), given by:[3]

$$\Delta\nu = \frac{1}{\lambda_{\text{in}}} - \frac{1}{\lambda_{\text{out}}} \tag{2.2}$$

The units of $\Delta\nu$ values are cm^{-1}. λ_{in} and λ_{out} are the wavelengths of the laser and the emitted photons respectively. The scattering efficiency of $LiPF_6$ based electrolytes has been reported to worsen with increasing salt concentration.[5] In order to maximise scattering efficiency and minimise any fluorescence backgrounds a 785 nm laser was used for all Raman measurements in this thesis. This technique was utilised to extract solvation information and measure concentration changes under applied currents for the electrolytes of interest.

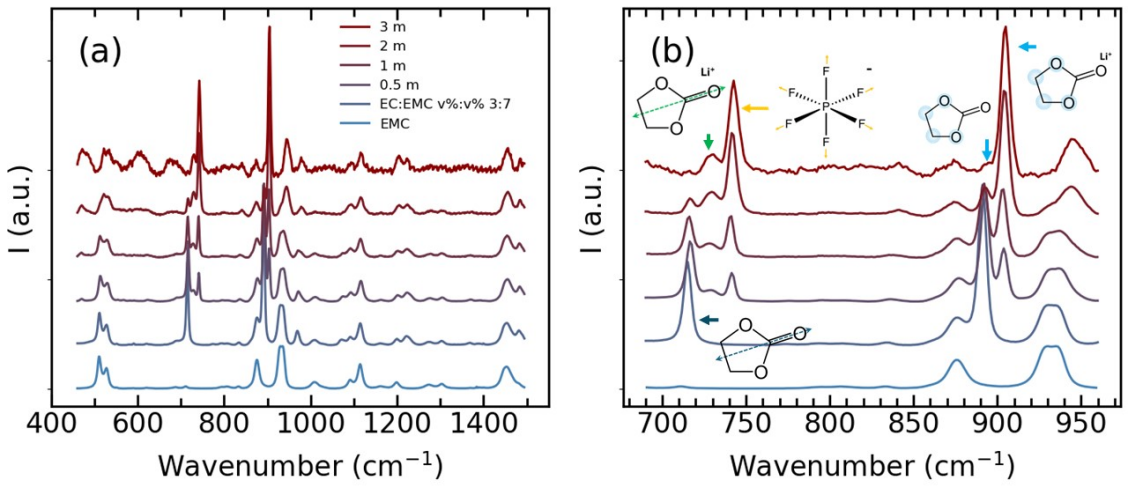

Figure 2.2: Example Raman spectra collected for $LiPF_6$ in EC:EMC based electrolytes at different salt concentrations using the experimental setup in Figure 2.1. (a) Raman spectrum recorded for $LiPF_6$ in EC:EMC (vol:vol 3:7) at different salt concentrations. (b) Zoomed in portion of the spectrum in (a).

2.2 Classical Molecular Dynamics

MD is a computational technique used to simulate the time evolution of a system of interacting particles. Its applications include chemistry, physics, and materials science with the aim of studying the behavior of atoms and molecules at the atomic level. In MD simulations, the motion of particles is described by Newton's equations of motion, which relate the forces acting on each particle to their positions and velocities. By numerically integrating these equations over small time steps, the trajectories of particles can be simulated over time.

The OPLS-AA (Optimized Potentials for Liquid Simulations-All Atom) force field is a widely used empirical potential energy function in classical MD simulations.[6] It is designed to accurately describe the interactions between atoms in organic and biomolecular systems. The OPLS-AA force field includes parameters for bonded and non-bonded interactions, such as bond lengths, bond angles, dihedral angles, and van der Waals interactions. These parameters are derived from experimental data and quantum mechanical calculations to ensure accurate representation of molecular properties. MD was used to simulate trajectories and solvation environments for $LiPF_6$ in EC:EMC (vol:vol 3:7) electrolytes which are investigated in chapters 4 and 5 of this thesis.

2.3 X-ray Absorption Spectroscopy (XAS)

XAS probes the ground state to excited state electronic transitions which arise due to the absorption of incident X-rays. It provides insight on the chemical state and environment of atoms in molecules. Synchrotrons, such as Diamond Light Source (DLS), provide a range of incident X-ray energies applicable to many elements of interest in LIB electrolytes and electrodes such as C, O, Mn, Ni, Co etc.

Core electrons absorb incident X-rays, inducing an electronic transition from the core level to the LUMO (known as X-ray absorption near edge structure (XANES)) and the continuum (extended X-ray absorption fine structure (EXAFS)). XANES is sensitive to the inter- and intramolecular environment of target atoms, making it ideal for investigating interfacial species on electrode surfaces[7,8] and the nature of solvation structures in LIB electrolytes.[9,10].

XAS can be measured in several modes. In this thesis, XAS is measured using total electron yield (TEY)[11], fluorescence yield (FY)[12] and inverse partial fluorescence yield (IPFY).[13]

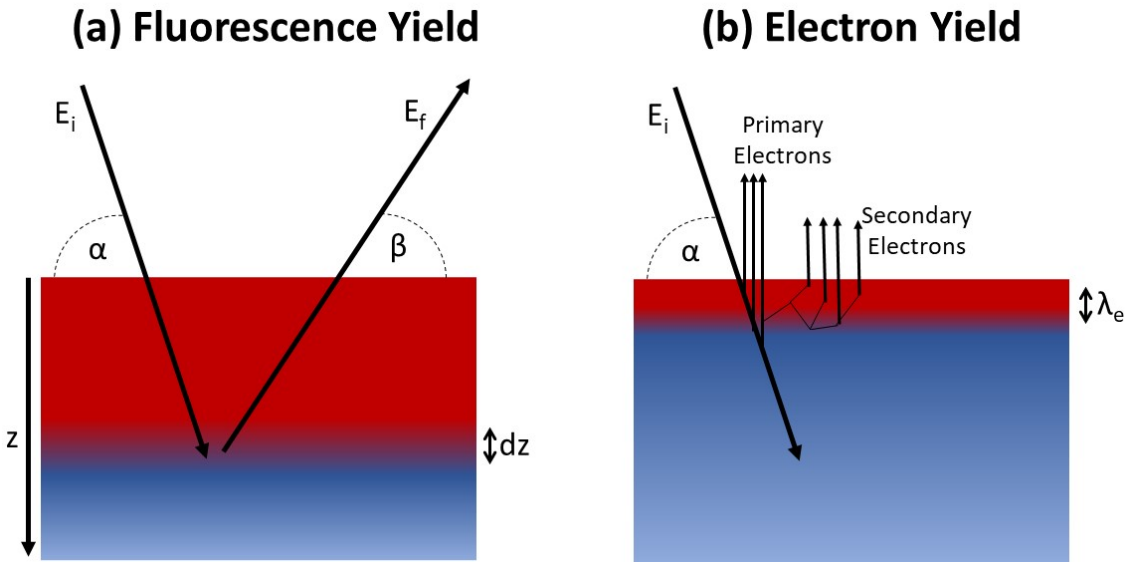

Figure 2.3: Schematic representation of (a) fluorescent photon and (b) electron emission.

TEY and FY work under the assumption that the absorption cross-section is proportional to the number of core holes created. Core holes are then filled by electrons with lower binding energies, resulting in the emission of photons and electrons. TEY is more surface sensitive as the probing depth is determined by the escape depth of electrons, which is typically around 10 nm.[14–16] The probing depth in FY is determined by the penetration depth of incident and emitted photons. In the soft X-ray region this corresponds to $\approx$ 200 nm.[13] In FY a photodiode is used to measure fluorescence for a range of emitted. FY

measurements suffer from self absorption effects, which occur when the incident photon penetration depth varies as they near a resonant absorption edge (i.e. when the incident photon energy matches the energy of a core shell electron transition).[17,18]

TEY can suffer from distortion due to saturation effects when the penetration depth of the incident photon is close to the escape depth of the emitted electrons,[19] though to a much lesser extent than FY. Achkar et al. introduced IPFY as an alternative means to measure XAS free from the drawbacks of self absorption and saturation effects.[13] The approach utilises an energy-selective detector to record the FY spectrum for a range of energies. The number of photons measured with energies lower than the resonant edge and falling within the energy range of a non resonant edge corresponding to a different species are integrated to extract a distortion free spectrum. Consider the X-ray emission intensity, $I(E_\mathrm{i}, E_\mathrm{f})$, as a function of incident (E_i) and emitted (E_f) photons, normalized to the incident photon intensity, $I_0(E_\mathrm{i})$.[13]

$$\frac{I(E_\mathrm{i}, E_\mathrm{f})}{I_0(E_\mathrm{i})} = C \sum_X \int_0^\infty \omega_X(E_\mathrm{i}, E_\mathrm{f}) \frac{\mu_X(E_\mathrm{i})}{\sin\alpha} e^{-(\frac{\mu(E_\mathrm{i})}{\sin\alpha} + \frac{\mu(E_\mathrm{f})}{\sin\beta})z} dz \tag{2.3}$$

$C = \frac{\eta(E_\mathrm{f})\Omega}{4\pi}$ where $\eta(E_\mathrm{f})$ is the detector efficiency and Ω is the solid angle of the detector. μ is the total linear attenuation coefficient of the material and is dependent on the energy of the photon undergoing attenuation. α and β are the angles of incidence and detection respectively. X corresponds to the core levels contributing photons to the total X-ray emission intensity (X = C 1s, O 1s, Mn 2p etc.) and $\mu_X(E_\mathrm{i})$ is the linear absorption coefficient contribution from X. $\omega_X(E_\mathrm{i}, E_\mathrm{f})$ is the fluorescence probability of X for given incident and emission photon energies. For an infinitely thick, homogeneous sample

$$\int_0^\infty e^{-(\frac{\mu(E_\mathrm{i})}{\sin\alpha} + \frac{\mu(E_\mathrm{f})}{\sin\beta})z} dz = \frac{-1}{\frac{\mu(E_\mathrm{i})}{\sin\alpha} + \frac{\mu(E_\mathrm{f})}{\sin\beta}} \left(\frac{1}{e^\infty} - \frac{1}{e^0}\right) = \frac{\sin\alpha}{\mu(E_\mathrm{i}) + \mu(E_\mathrm{f})\frac{\sin\alpha}{\sin\beta}} \tag{2.4}$$

Subbing this into equation (2.4) we find

$$\frac{I(E_\mathrm{i}, E_\mathrm{f})}{I_0(E_\mathrm{i})} = C \sum_X \frac{\omega_X(E_\mathrm{i}, E_\mathrm{f}) \mu_X(E_\mathrm{i})}{\mu(E_\mathrm{i}) + \mu(E_\mathrm{f})\frac{\sin\alpha}{\sin\beta}} \tag{2.5}$$

The photon absorption and emission can correspond to the excitation of a core level into free-electron like continuum of states (e.g. C 1s into continuum states for incident energies at the O K-edge) or the excitation of a core electron into unoccupied states near threshold (e.g. Mn 2p to Mn 3p unoccupied states for energies at the F K-edge). X-ray emission from these processes can be categorized as either a resonant X-ray emission spectrum (RXES) or a non-resonant X-ray emission spectrum (NXES). The importance

of this distinction lies in the fact that $\omega_X(E_i, E_f)$ and $\mu_X(E_i)$ vary strongly for RXES but weakly for NXES. Using the emission energy sensitive detector and scanning incident energies through an absorption edge (e.g. O K-edge) , the NXES from the element and core electron Y (e.g. Y = C K-edge emission) and not the RXES (e.g. O K-edge) this further simplifies to

$$\frac{I(E_\mathrm{i}, E_\mathrm{f})}{I_0(E_\mathrm{i})} = C\frac{\omega_Y(E_\mathrm{i}, E_\mathrm{f})\mu_Y(E_\mathrm{i})}{\mu(E_\mathrm{i}) + \mu(E_\mathrm{f})\frac{\sin\alpha}{\sin\beta}} \tag{2.6}$$

At E_i all of $\omega_Y(E_\mathrm{i}, E_\mathrm{f}) = \omega_Y(E_\mathrm{f})$, $\mu_Y(E_\mathrm{i}) = \mu_Y$ and $\mu(E_f)$ are approximately constant. Inverting the equation (2.6) yields

$$\mathrm{IPFY} = \frac{I_0(E_\mathrm{i})}{I(E_\mathrm{i}, E_\mathrm{f})} = A[\mu(E_\mathrm{i}) + B] \tag{2.7}$$

where $A = \frac{1}{C\omega_Y(E_\mathrm{i})\mu_Y}$, $B = \mu(E_\mathrm{f})\frac{\sin\alpha}{\sin\beta}$ and both are approximately constant over the scanned incident energy range. This demonstrates that IPFY varies linearly with the linear attenuation coefficient $\mu_i(E_i)$ and is not subject to self absorption or saturation effects. The constant background, AB, is minimized for small grazing angles α and large detection angles β. IPFY requires a detector with sufficiently small dark counts (background) and resolution to discern NXES from the RXES.

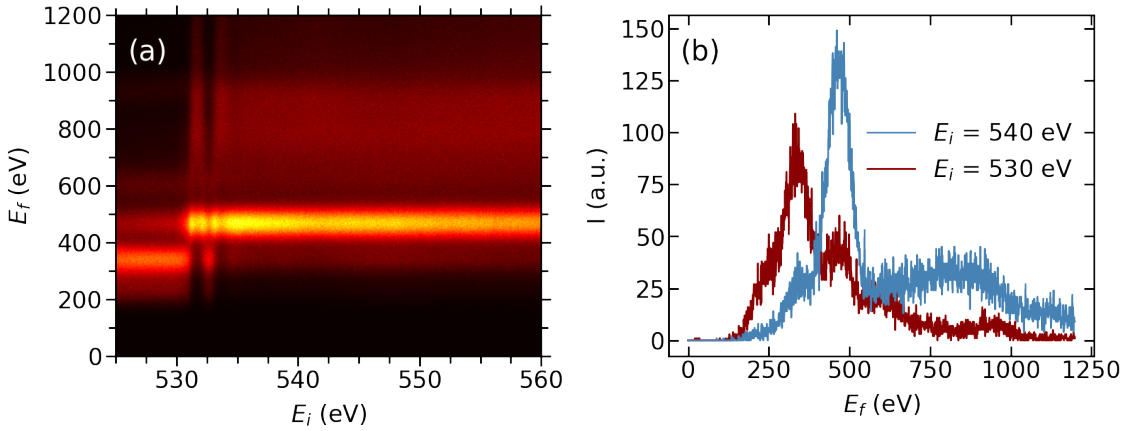

Figure 2.4: (a) Normalized PFY spectrum of 1.1 M $LiPF_6$ in EC:EMC as function of E_i and E_f as the incident photon energy is scanned through the O K-edge. (b) The emission spectra between 0-1250 eV for incident photon energies of 530 eV (red) and 540 eV (blue) demonstrating the change above and below the resonant energy in the O K-edge.

In Figure 2.4a FY spectrum for 1.1 M $LiPF_6$ in EC:EMC is plotted as function of E_i (525-560 eV) and E_f(0-1250eV). By either integrating the intensity in the NXES region or fitting a Gaussian function to the NXES and taking the area under the curve the IPFY spectrum for the O K-edge may be obtained. XAS in TEY and FY modes is used in chapter

3 to investigate the nature of the CEI on NMC811 after cycling in $LiPF_6$ in EC:EMC electrolytes at different salt concentrations. XAS in FY and IPFY modes are utilised in chapter 5 to extract bulk solvation information for different concentration for $LiPF_6$ in EC:EMC electrolytes.

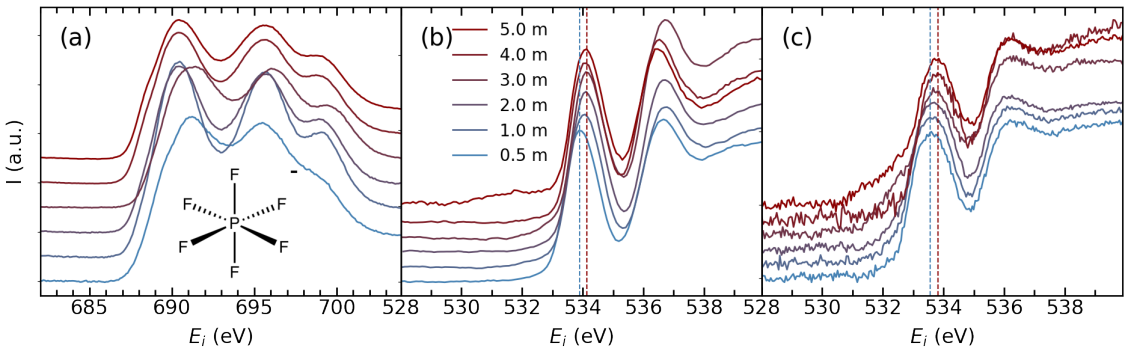

Figure 2.5: (a) FY of the F K-edge for $LiPF_6$ in EC:EMC (vol:vol 3:7) at different salt concentrations. (b) FY and (c) IPFY spectra of the O K-edge for $LiPF_6$ in EC:EMC at different salt concentrations.

2.4 X-ray Photoelectron Spectroscopy (XPS)

X-ray photoelectron spectroscopy (XPS), also known as electron spectroscopy for chemical analysis (ESCA),[20] is a type of electron spectroscopy which is commonly used to investigate the composition of interfaces owing to its surface sensitivity. The working principle of XPS is based on the photoelectric effect.[21] An incident X-ray irradiates the sample, exciting core electrons resulting in their emission from the sample surface. The kinetic energy (E_K) of the emitted electrons is related to the binding energy (E_B) of the core level they originated from.

$$hf = E_K + E_B + \phi_d \tag{2.8}$$

f is the frequency of the incident X-ray, h is Planck's constant and ϕ_d is the work function of the detector. The energy of the incident X-ray is usually known. In this thesis we use the $Al_{K\alpha}$ at the energy of 1486.6 eV. E_K of the electrons is measured and ϕ_d is known enabling us to calculate E_B. E_B is element specific and but also environment specific as the energy of the electron orbitals vary depending on their bonding environment enabling the identification of different chemical species. Shifts towards higher E_B values occur for atoms bonded to more electronegative atoms, as their electron density is drawn away causing the remaining electrons to be more tightly bound.

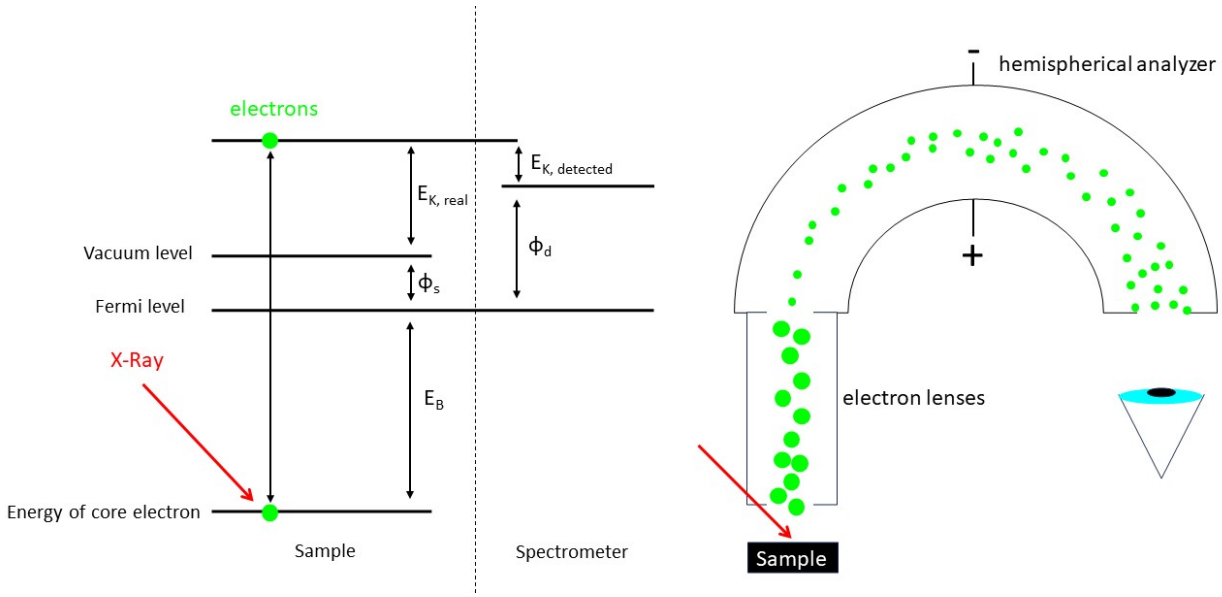

Figure 2.6: Schematic illustration of the detection of E_B using XPS.

As demonstrated in Figure (2.6), a concentric hemispherical analyzer is used to detect electrons by only allowing electrons with a certain energy to pass through. The pass

energy is dependent on the potential applied to the hemispheres. The resolution is determined by the hemisphere radius and the pass energy.[22] To avoid the need for large detectors and varying resolution depending on the electron energy, electrons are slowed as they approach the analyzer and the pass energy is fixed. XPS is used to investigate the composition of the CEI on NMC811 cathodes post cycling in $LiPF_6$ in EC:EMC electrolytes at different salt concentrations.

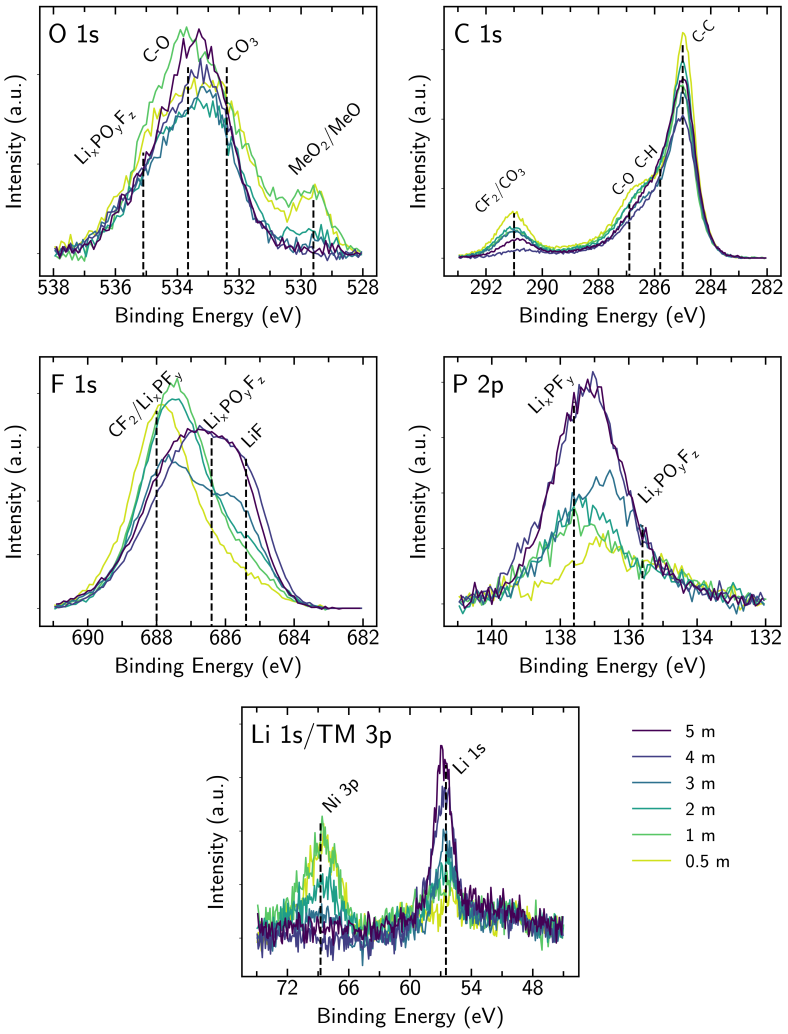

Figure 2.7: Example of data of post cycled NMC811 electrodes cycled vs. LTO in different $LiPF_6$ concentration electrolytes collected during this thesis for the O 1s, C 1s, F 1s, P 2p and Li 1s/TM 3p core levels with demonstrating element selectivity and chemical sensitivity of XPS. Reprinted with permission from Ref [30]. Copyright 2024 American Chemical Society.

2.5 Boundary Value Problem Solver

The continuum scale models investigated in this thesis were formulated as a boundary value problem (BVP) to facilitate their simulation. The formulated BVP was then solved using a multivariate Newton-Raphson method described by Newman.[23] Dual numbers have previously been incorporated for use in Newton-Raphson type BVP solvers to compute the Jacobian matrix required for the method[24] and in-depth reviews are available in the literature[25,26]. A dual number, μ, is a type of complex number expressed as

$$\mu = r + d\varepsilon \tag{2.9}$$

r and d are the real and imaginary components of μ respectively. It is assumed that $\varepsilon^2 = \varepsilon^3 = \cdots = 0$. Addition, subtraction and multiplication are found yield

$$\mu_i + \mu_j = (r_i + r_j) + (d_i + d_j)\varepsilon \tag{2.10}$$

$$\mu_i - \mu_j = (r_i - r_j) + (d_i - d_j)\varepsilon \tag{2.11}$$

$$\mu_i \cdot \mu_j = (r_i r_j) + (r_i d_j + r_j d_i)\varepsilon + (d_i d_j)\varepsilon^2 = (r_i r_j) + (r_i d_j + r_j d_i)\varepsilon \tag{2.12}$$

in terms of the dual components. If we take the Taylor expansion of μ we find

$$f(\mu) = f(r + d\varepsilon) = f(r) + f'(r)d\varepsilon + \frac{1}{2}f''(r)d^2\varepsilon^2 + \ldots \approx f(r) + f'(r)d\varepsilon + O(\varepsilon^2) \tag{2.13}$$

The right hand side of equation (2.13) may be expressed as another dual number,

$$\mu_f = r_f + d_f\varepsilon = f(r) + f'(r)d\varepsilon \tag{2.14}$$

If d is set to equal 1 we find that the dual component d_f after evaluating the function with a dual number as input is the first order derivative of the function, f, with respect to the real component of the input variable, r, evaluated at r. Using this arithmetic, both the value of a function and its derivative with respect to an input, evaluated at the input value, may be obtained. Using equation (2.14) elementary functions (exp, sin, cos, tan etc.) may be defined. Additionally, the division operation may be implemented by first considering an inversion function and then using the multiplication arithmetic defined in

2.12.

$$(\mu)^{-1} = \frac{1}{r} + f'(\frac{1}{r})d = \frac{1}{r} + (-\frac{1}{r^2}d) = \frac{1}{r} - \frac{1}{r^2}d \tag{2.15}$$

Using dual numbers (DN) arithmetic, a multivariate Newton-Raphson method was implemented in Python and used to solve the continuum scale BVP based on MS diffusion presented in chapter 4. The code implementation is provided in the appendix.

2.6 Electrochemical Impedance Spectroscopy (EIS)

Electrochemical impedance spectroscopy (EIS) can provide kinetic and mechanistic information in many kinds of electrochemical systems, including LIBs. A small sinusoidal wave of current or voltage is applied to the working electrode over a wide range of frequencies, and the induced voltage/current response is recorded. From applied and measured signals from the working electrode, the impedance can be obtained.

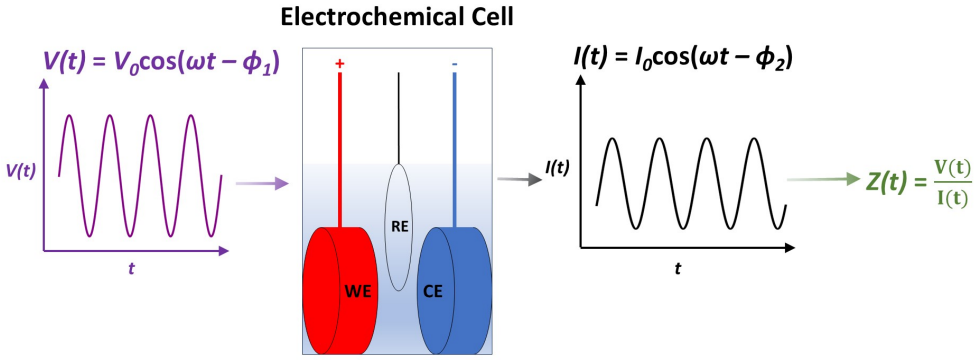

V_0 and I_0 are the maximum amplitudes of the applied voltage perturbation and measured current signal. ω is the angular frequency and ϕ_1 and ϕ_2 are the phase angles of the current and voltage respectively. In LIBs, redox reactions involving Li^+ ions occur between the electrodes and the electrolyte. From the intercalation kinetics of the battery electrodes, consider the Butler-Volmer equation:

$$i = i_0 \left[\exp\left(\frac{\alpha_a F(\phi_1 - \phi_2 - U)}{RT}\right) - \exp\left(-\frac{\alpha_c F(\phi_1 - \phi_2 - U)}{RT}\right) \right] \tag{2.16}$$

where i_0 is the exchange current density, ϕ_1 is the electrical potential in the cathode, ϕ_2 is the electrical potential in the electrolyte, U is the open circuit voltage of the cathode interface, F is Faraday's constant, R is the universal gas constant, α_a and α_c are the anodic and cathodic transfer coefficients, respectively. Newman and coworkers assumed the intercalation kinetics of battery electrodes to be a first-order process and thereby obtained an expression for i_0 in a liquid electrolyte:[23,27,28]

$$i_0 = Fk(c_{s,max} - c_s)^{\alpha_a} c_s^{\alpha_c} c_e^{\alpha_a} \tag{2.17}$$

where c_e is the local electrolyte lithium ion concentration, c_s is the concentration of lithium in the solid electrode, $(c_{s,max} - c_s)$ is the concentration of unoccupied sites in the electrode, and the rate constant k can be described by the Arrhenius equation with an appropriate reaction dependent pre-exponential factor and activation energy. This

expression assumes the number of intercalation sites in the active material particles is conserved.

For concentrated electrolytes, the limited Li solubility in the electrolyte must also be considered, as has been recently highlighted.[29] A similar approach to that employed by Newman and coworkers for polymer electrolytes can be taken,[28] by adapting the expression for i_0 to:

$$i_0 = Fk(c_{s,max} - c_s)^{\alpha_a} c_s^{\alpha_c} (c_{e,max} - c_e)^{\alpha_c} c_e^{\alpha_a} \tag{2.18}$$

where the solubility limit of the electrolyte is taken into account by $(c_{e,max} - c_e)$. Assuming small perturbations ($\leq$ 5 mV) of the overpotential, $\eta = \phi_1 - \phi_2 - U$, the expression for i may be linearized using exp(x) $\approx$ 1 + x and expressed as:

$$i = \frac{Fi_0}{RT}\eta \tag{2.19}$$

The charge transfer resistance, R_{ct}, from Butler-Volmer kinetics may then be expressed as:

$$R_{ct} = \lim_{\eta \to 0} \frac{\eta}{i} = \frac{RT}{Fi_0} = \frac{RT}{F^2 k(c_{s,max} - c_s)^{\alpha_a} c_s^{\alpha_c} (c_{e,max} - c_e)^{\alpha_c} c_e^{\alpha_a}} \tag{2.20}$$

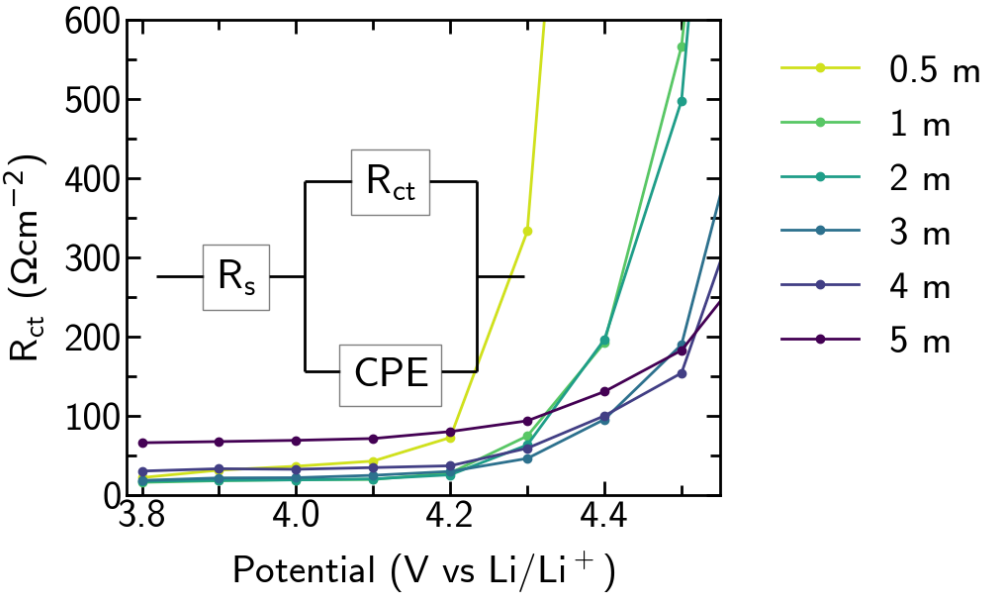

Figure 2.8: Demonstration of the variation in R_{ct} with potential for NMC811 electrodes in different salt concentration electrolytes following cycling.[30] Adapted with permission from Ref [30]. Copyright 2024 American Chemical Society.

R_{ct} values can be extracted from impedance measurements by modelling the system with an equivalent circuit. An equivalent circuit consists of simple electrical components, such as resistors, capacitors, inductors, constant phase elements (CPE) etc, in series and/or in parallel. A CPE models non-ideal capacitive behavior in an equivalent circuit. An ideal capacitor has a purely capacitive impedance, while a CPE accounts for frequency-dependent deviations from ideality due to factors such as surface roughness, inhomogeneities, and diffusion effects in electrochemical systems. The equivalent circuit models the separate capacitances and resistances in the system, giving rise to an analytic form for the impedance for that circuit. By fitting the analytic expression for the impedance to the measured values, the individual resistances and capacitances may be determined. In chapter 3, to model the NMC811 electrode interface we consider resistor, R_S, in parallel with a CPE. The parallel component is then in series with another resistor, R_S (see Figure 2.8). The CPE behaves as a non-ideal capacitor, modelling the electrical double layer at the interface between the NMC811 and the electrolyte. The R_{ct} component models the kinetic behaviour of the Li^+ redox process. The R_S component accounts for any solution resistances arising from the ionic conductivity limitations in the electrolyte. Such circuits have previously been used to extract R_{ct} values from NMC811 electrodes.[31,32] Figure (2.9) demonstrates the variation in R_{ct} with electrolyte molality (a) and molarity (b) for pristine NMC811 electrodes directly cycled to 3.8 V, 3.9 V, and then 4.0 V expected from equation 2.20. Equation 2.20 does not take into account any CEI contribution to the overpotential, though this contribution likely comes into play in the more highly concentrated electrolytes. Nevertheless, the behaviour of the extracted R_{ct} values demonstrates qualitatively similar behaviour to that predicted by equation 2.20.

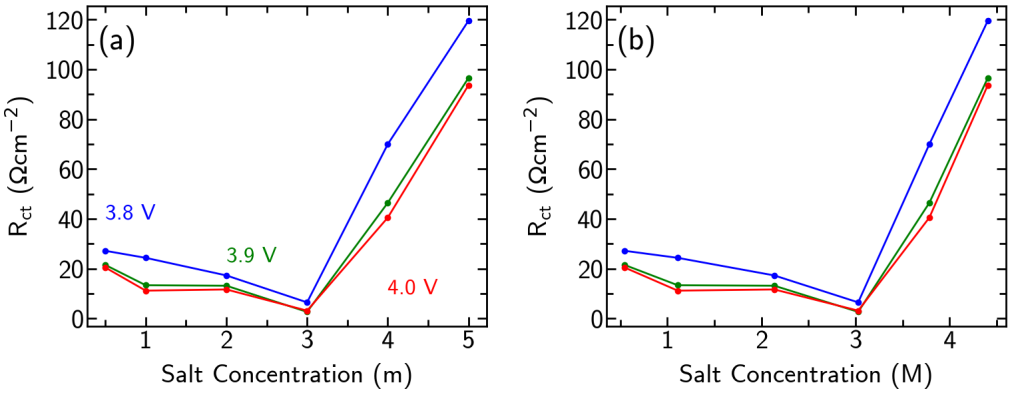

Figure 2.9: Demonstration of the variation in R_{ct} with (a) electrolyte molality and (b) electrolyte molarity for pristine NMC811 electrodes directly cycled to 3.8 V, 3.9 V, and then 4.0 V expected from equation 2.20. Adapted with permission from Ref [30]. Copyright 2024 American Chemical Society.

2.7 Nuclear Magnetic Resonance Spectroscopy (NMR)

Nuclear magnetic resonance spectroscopy (NMR) probes molecules by measuring the interaction of radiofrequency (rf) radiation with nuclei under a strong applied magnetic field. Nuclei of certain atoms possess a nuclear spin, which generates a small magnetic field around the nucleus. Nuclei with an odd number of protons or neutrons (hydrogen-1 (^{1}H), carbon-13 (^{13}C), phosphorus-31 (^{31}P), and fluorine-19 (^{19}F)) have a non-zero nuclear spin and possess a magnetic moment enabling them to be investigated using NMR.[33–35]

Before any magnetic field is applied, the nuclear spins in the sample are randomly oriented. There is no net macroscopic magnetization. The individual nuclear magnetic moments cancel each other out due to their random orientations. A strong external magnetic field (B_0) is applied, the nuclear spins align either parallel or anti-parallel to the direction of the magnetic field. The lower energy state (α state) corresponds to alignment parallel to the magnetic field, while the higher energy state (β state) corresponds to alignment anti-parallel to the field. This results in a slight excess of spins aligned with the magnetic field, creating a net macroscopic magnetization along the direction of the field. The nuclear magnetic moments cause the aligned nuclear spins to precess about the direction of the main magnetic field at the *Larmor frequency*, which is characteristic of each nucleus.

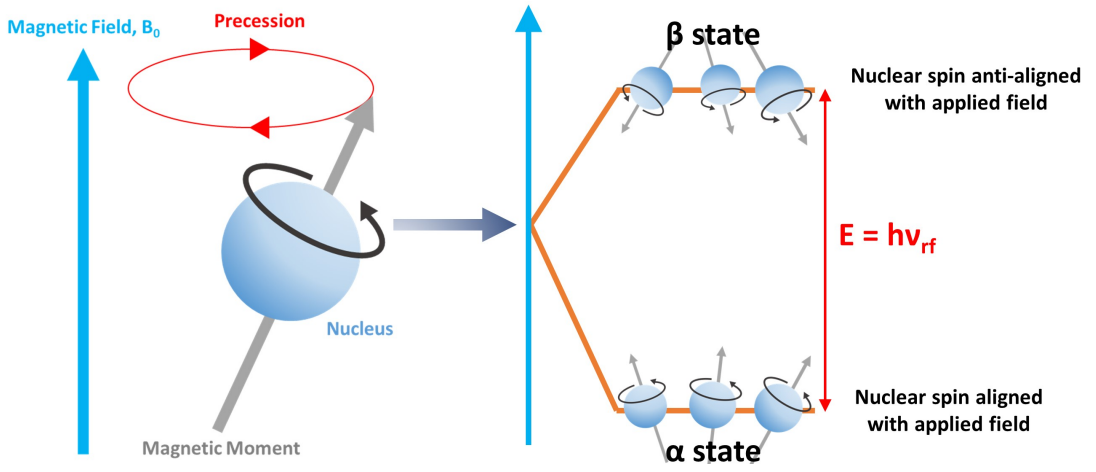

A short-duration rf pulse is applied perpendicular to the main magnetic field. If the rf pulse has a frequency, ν_{rf}, that matches the energy difference between the α and β states the pulse temporarily disrupts the alignment of the nuclear spins by tipping them away from the direction of the main magnetic field.

Nuclei in the lower energy state (α) absorb energy from the rf pulse and transition to the higher energy state (β), aligning anti-parallel in opposition to the main magnetic

field. This resonance absorption results in a net decrease in the macroscopic magnetization.

Post rf pulse the nuclear spins begin to relax back to their equilibrium state via two processes: Spin-lattice relaxation (T1) and spin-spin relaxation (T2). T1 is the process by which the nuclear spins return to thermal equilibrium with the surroundings, aligning with the main magnetic field. This process involves energy transfer between the spins and the lattice, i.e. the molecular environment. T2 is the process by which the phase coherence among the precession of the spins decay due to interactions between neighboring spins, leading to a loss of signal intensity.

The net macroscopic magnetization starts to recover along the direction of the main magnetic field with the rate of recovery depends on the relaxation times T1 and T2. This generates a weak rf signal which is detected by a receiver coil and converted into a NMR spectrum. The resulting spectrum provides information about the chemical environment and molecular structure of the sample, including chemical shifts, coupling constants, and peak intensities. NMR is employed in chapter 3 to investigate electrolyte soluble decomposition products of $LiPF_6$ in EC : EMC (vol:vol 3:7) at different salt concentrations post cycling in NMC811/LTO full cells.

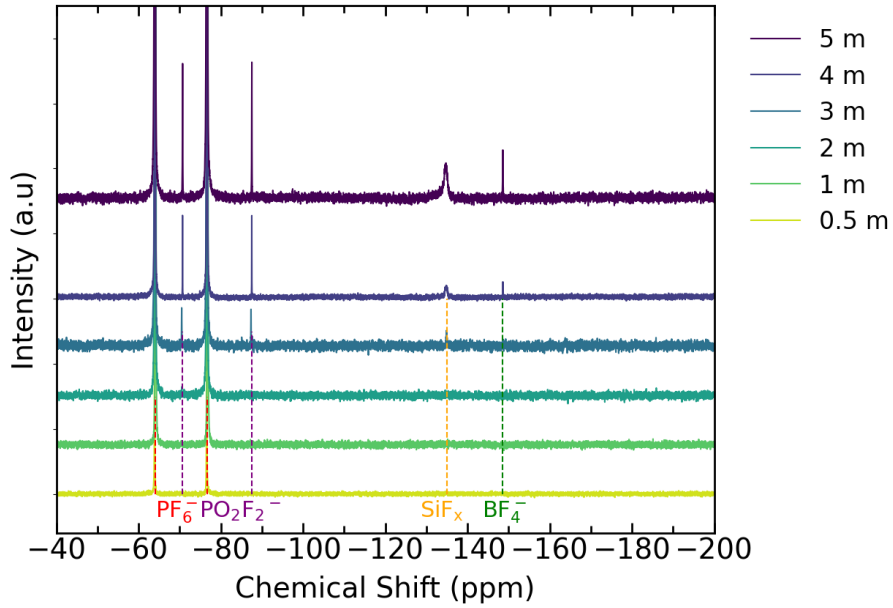

Figure 2.10: ^{19}F NMR spectra of $LiPF_6$ in EC:EMC based electrolytes post cycling for the different salt concentrations (0.5 m - 5 m), highlighting the usefulness of NMR in distinguishing between different chemical compounds. Reprinted with permission from Ref [32]. Copyright 2024 American Chemical Society.

2.8 Inductively Coupled Plasma Optical Emission Spectroscopy (ICP-OES)

ICP-OES is a convenient analytical technique that can provide elemental composition information on a wide array of samples. Initially, atomic emission spectroscopy was performed using flame-based methods, but these had limitations in sensitivity and spectral interference. In the 1960s, Sir Alan Walsh introduced the concept of ICP-OES as a high-temperature ionization source for atomic spectroscopy and spectrometers began receiving widespread use during the 1970s.[36]

ICP-OES is generated by passing a flow of inert gas such as argon through a rf coil, inducing a high-frequency electromagnetic field. The inert gas is ionized by the field, forming high-temperature plasma. The sample is introduced via the nebulizer, where it is aerosolized and moved to the plasma by an argon flow. The high plasma temperature vaporizes the sample, breaking molecular bonds and converting the elements into atoms which are excited by collisions with electrons and ions in the plasma, leading to the promotion of electrons to higher energy levels. Photons are emitted as the excited atoms return to their ground state which are collected and passed to a spectrometer. The spectrometer disperses the light based on wavelength, allowing the intensity of light at each wavelength to be measured by a CCD or photomultiplier tube (PMT). The wavelengths of the emitted photons are element specific and their intensities are proportional to atomic concentration. Typically, a particular wavelength is selected for the atom of interest. A calibration curve of atomic concentration versus light intensity is constructed using reference samples with known quantities of the atom of interest. The intensity measured from then quantified in terms of molar concentration.

Bibliography

[1] J. R. Ferraro, K. Nakamoto, and C. W. Brown, *Introductory Raman Spectroscopy: Second Edition*. 2003.

[2] L. Opilik, T. Schmid, and R. Zenobi, "Modern raman imaging: Vibrational spectroscopy on the micrometer and nanometer scales," *Annual Review of Analytical Chemistry*, vol. 6, 2013.

[3] E. Smith and G. Dent, *Modern raman spectroscopy: A practical approach*. 2019.

[4] T. Schmid and P. Dariz, "Raman microspectroscopic imaging of binder remnants in historical mortars reveals processing conditions," *Heritage*, vol. 2, no. 2, 2019.

[5] L. Cabo-Fernandez, A. R. Neale, F. Braga, I. V. Sazanovich, R. Kostecki, and L. J. Hardwick, "Kerr gated Raman spectroscopy of LiPF6 salt and LiPF6-based organic carbonate electrolyte for Li-ion batteries," *Physical Chemistry Chemical Physics*, vol. 21, no. 43, 2019.

[6] W. L. Jorgensen, D. S. Maxwell, and J. Tirado-Rives, "Development and testing of the OPLS all-atom force field on conformational energetics and properties of organic liquids," *Journal of the American Chemical Society*, vol. 118, no. 45, 1996.

[7] E. Björklund, E. Wikner, R. Younesi, D. Brandell, and K. Edström, "Influence of state-of-charge in commercial LiNi0.33Mn0.33Co0.33O2/LiMn2O4-graphite cells analyzed by synchrotron-based photoelectron spectroscopy," *Journal of Energy Storage*, vol. 15, 2018.

[8] E. Björklund, C. Xu, W. M. Dose, C. G. Sole, P. K. Thakur, T. L. Lee, M. F. De Volder, C. P. Grey, and R. S. Weatherup, "Cycle-Induced Interfacial Degradation and Transition-Metal Cross-Over in LiNi0.8Mn0.1Co0.1O2-Graphite Cells," *Chemistry of Materials*, vol. 34, no. 5, 2022.

[9] J. E. N. Swallow, M. W. Fraser, N.-J. H. Kneusels, J. F. Charlton, C. G. Sole, C. M. E. Phelan, E. Björklund, P. Bencok, C. Escudero, V. Pérez-Dieste, C. P. Grey, R. J. Nicholls, and R. S. Weatherup, "Revealing solid electrolyte interphase

formation through interface-sensitive Operando X-ray absorption spectroscopy," *Nature Communications*, vol. 13, no. 1, p. 6070, 2022.

[10] J. W. Smith, R. K. Lam, A. T. Sheardy, O. Shih, A. M. Rizzuto, O. Borodin, S. J. Harris, D. Prendergast, and R. J. Saykally, "X-Ray absorption spectroscopy of LiBF4 in propylene carbonate: A model lithium ion battery electrolyte," *Physical Chemistry Chemical Physics*, vol. 16, no. 43, 2014.

[11] W. Gudat and C. Kunz, "Close similarity between photoelectric yield and photoabsorption spectra in the soft-x-ray range," *Physical Review Letters*, vol. 29, no. 3, 1972.

[12] J. Jaklevic, J. A. Kirby, M. P. Klein, A. S. Robertson, G. S. Brown, and P. Eisenberger, "Fluorescence detection of exafs: Sensitivity enhancement for dilute species and thin films," *Solid State Communications*, vol. 23, no. 9, 1977.

[13] A. J. Achkar, T. Z. Regier, H. Wadati, Y. J. Kim, H. Zhang, and D. G. Hawthorn, "Bulk sensitive x-ray absorption spectroscopy free of self-absorption effects," *Physical Review B - Condensed Matter and Materials Physics*, vol. 83, no. 8, 2011.

[14] F. de Groot and A. Kotani, *Core level spectroscopy of solids*. 2008.

[15] F. M. De Groot, "X-ray absorption and dichroism of transition metals and their compounds," 1994.

[16] J. Stöhr, *NEXAFS spectroscopy*, vol. 25. Springer Science & Business Media, 2013.

[17] S. Eisebitt, T. Böske, J. E. Rubensson, and W. Eberhardt, "Determination of absorption coefficients for concentrated samples by fluorescence detection," *Physical Review B*, vol. 47, no. 21, 1993.

[18] L. Tröger, D. Arvanitis, K. Baberschke, H. Michaelis, U. Grimm, and E. Zschech, "Full correction of the self-absorption in soft-fluorescence extended x-ray-absorption fine structure," *Physical Review B*, vol. 46, no. 6, 1992.

[19] R. Nakajima, J. Stöhr, and Y. U. Idzerda, "Electron-yield saturation effects in l-edge x-ray magnetic circular dichroism spectra of fe, co, and ni," *Physical Review B - Condensed Matter and Materials Physics*, vol. 59, no. 9, 1999.

[20] M. Favaro, B. Jeong, P. N. Ross, J. Yano, Z. Hussain, Z. Liu, and E. J. Crumlin, "New Advances in Ambient Pressure X-Ray Photoelectron Spectroscopy: Operando Probing of the Electrical Double Layer at the Solid/Liquid Interfac," *ECS Meeting Abstracts*, vol. MA2016-02, no. 46, 2016.

[21] P. S. Bagus, E. S. Ilton, and C. J. Nelin, "The interpretation of XPS spectra: Insights into materials properties," 2013.

[22] B. Crist, "A Review of XPS Data-Banks," *XPS International*, vol. 1, 2007.

[23] J. Newman and K. E. Thomas-Alyea, *Electrochemical systems. Third edition*. 2004.

[24] N. W. Brady, M. Mees, P. M. Vereecken, and M. Safari, "Implementation of Dual Number Automatic Differentiation with John Newman's BAND Algorithm," *Journal of The Electrochemical Society*, vol. 168, no. 11, 2021.

[25] J. Angeles, "The Application of Dual Algebra to Kinematic Analysis," 1998.

[26] A. T. Yang and F. Freudenstein, "Application of dual-number quaternion algebra to the analysis of spatial mechanisms," *Journal of Applied Mechanics, Transactions ASME*, vol. 31, no. 2, 1964.

[27] T. F. Fuller, M. Doyle, and J. Newman, "Simulation and Optimization of the Dual Lithium Ion Insertion Cell," *Journal of The Electrochemical Society*, vol. 141, no. 1, 1994.

[28] M. Doyle, T. F. Fuller, and J. Newman, "Modeling of Galvanostatic Charge and Discharge of the Lithium/Polymer/Insertion Cell," *Journal of The Electrochemical Society*, vol. 140, no. 6, 1993.

[29] R. Morasch, H. A. Gasteiger, and B. Suthar, "Li-Ion Battery Active Material Impedance Analysis I: Comparison of Measured NCM 111 Kinetics with Butler-Volmer Equation Based Predictions," *Journal of The Electrochemical Society*, vol. 170, no. 8, 2023.

[30] C. M. E. Phelan, E. Bjorklund, J. Singh, M. Fraser, P. N. Didwal, G. J. Rees, Z. Ruff, P. Ferrer, D. C. Grinter, C. P. Grey, and others, "Role of Salt Concentration in Stabilizing Charged Ni-Rich Cathode Interfaces in Li-Ion Batteries," *Chemistry of Materials*, vol. 36, no. 7, pp. 3334–3344, 2024.

[31] W. M. Dose, I. Temprano, J. P. Allen, E. Björklund, C. A. O'Keefe, W. Li, B. L. Mehdi, R. S. Weatherup, M. F. De Volder, and C. P. Grey, "Electrolyte Reactivity at the Charged Ni-Rich Cathode Interface and Degradation in Li-Ion Batteries," *ACS Applied Materials and Interfaces*, vol. 14, no. 11, 2022.

[32] W. M. Dose, W. Li, I. Temprano, C. A. O'Keefe, B. Layla Mehdi, M. F. L. De Volder, and C. P. Grey, "Onset Potential for Electrolyte Oxidation and Ni-Rich Cathode Degradation in Lithium-Ion Batteries," *ACS Energy Letters*, vol. 7, pp. 3524–3530, 9 2022.

[33] D. D. Laws, H. M. L. Bitter, and A. Jerschow, "Solid-state NMR spectroscopic methods in chemistry," 2002.

[34] M. H. Levitt, "The Signs of Frequencies and Phases in NMR," *Journal of Magnetic Resonance*, vol. 126, no. 2, 1997.

[35] D. Apperley, R. Harris, and P. Hodgkinson, *Solid-State NMR: Basic Principles & Practice*. 2012.

[36] C. Vandecasteele and C. B. Block, *Modern methods for trace element determination*. John Wiley & Sons, 1997.

Chapter 3

The Role of Salt Concentration in Stabilizing Charged Ni-Rich Cathode Interfaces in Li-ion Batteries

3.1 Abstract

The CEI in LIBs plays a key role in suppressing undesired side reactions whilst facilitating Li-ion transport. Ni-rich layered cathode materials offer improved energy densities, but their high interfacial reactivities can negatively impact cycle life and rate performance. Here we investigate the role of electrolyte salt concentration in altering the interfacial reactivity of charged NMC811 cathodes in standard $LiPF_6$ in carbonate based electrolytes (EC:EMC vol:vol 3:7). Extended potential holds of NMC811/LTO cells reveal that the parasitic electrolyte oxidation currents observed are strongly dependent on the electrolyte salt concentration. XPS and XAS reveal that a thicker $Li_xPO_yF_z$-/LiF-rich CEI is formed in the more highly concentrated electrolytes. This suppresses reactions with solvent molecules resulting in a thinner, or less-dense, RSL with lower charge transfer resistance, and lower oxidation currents at high potentials. The thicker CEI also limits access of acidic species to the RSL suppressing transition metal dissolution into the electrolyte, as confirmed by NMR and ICP-OES. This provides insight into the main degradation processes occurring at Ni-rich cathode interfaces in contact with carbonate based electrolytes, and how electrolyte formulation can help to mitigate these.

3.2 Introduction

Layered NMC cathode materials are increasingly used in commercial LIBs, with the redox activity mainly associated with the Ni and Co centres. Increasing Ni content results in higher capacities with the additional benefit of lowering the content of Co, which is both expensive and has ethical concerns over its acquisition[1]. However, this is accompanied by increased interfacial reactivities, particularly at high potentials, limiting the upper cut-off potentials that can be safely used.[2,3] As NMC is delithiated at high potentials, its layered structure is destabilised, resulting in oxygen release and the formation of a RSL at the particle surface.[4–8] The RSL typically exhibits poor ionic conductivity, contributing to increased interfacial impedances,[5,8–10] and thus limiting high C-rate capability.

For more Ni rich NMCs such as NMC811, the onset of significant RSL formation occurs at lower potentials vs. Li/Li^+,[6,7] with the accompanying release of reactive $^1O_2$ implicated in chemical oxidation of solvent components of the electrolyte.[6,7,11–13] The associated formation of acidic species[6,14–20] has been linked to TM dissolution from the cathode into the electrolyte and subsequent incorporation into the SEI on the anode,[2,3,8,20–22] processes that are expected to be more prominent for Ni rich NMCs and EC containing electrolytes. Understanding the role of the electrolyte in these interfacial degradation mechanisms is critical to improving the cycle life of Ni-rich NMC cells to realize practical improvements in LIB energy density. The role of different organic carbonates in promoting certain degradation mechanisms at charged Ni-rich NMC cathodes has recently been explored[2,3]. Here, we now investigate the role of $LiPF_6$ concentration (0.5-5 m) using NMC811/LTO full-cells in EC:EMC (vol:vol 3:7).

Cells were cycled such that the NMC811 reached a potential of 4.5 V vs. Li/Li^+ and were then held at this potential for 60 h, before discharge to 3.8 V vs. Li/Li^+. The cells were then characterised using ex-situ XPS to determine CEI compositions, NMR spectroscopy to identify soluble electrolyte decomposition products, EIS to measure interfacial impedances, XAS to investigate the nature of the RSL and CEI on the NMC811, and ICP-OES to quantify the extent of TM dissolution. We thereby show that at higher electrolyte salt concentrations a thicker, more $Li_xPO_yF_z$-/LiF-rich CEI is formed which protects the NMC811 against attack by solvent molecules and acidic species. This results in thinner/less-dense RSLs with lower charge transfer resistances, less TM dissolution into the electrolyte and lower parasitic oxidation currents at high potentials. These findings provide insight into the role of the CEI in stabilising the interfaces of Ni-rich NMCs in carbonate electrolytes, helping to inform strategies to mitigate NMC degradation at high potentials, such as through rational selection of electrolyte additives.

3.3 Experimental and theoretical methods

3.3.1 Materials and Electrolyte Fabrication

NMC811 and LTO electrodes were purchased from NEI corporation with areal capacities of 1.15 and 1.5 mAh/cm^2 respectively. The specific surface areas for the NMC811 and LTO were $\approx$ 0.35 m^2/g and $\approx$ 7.0 m^2/g respectively. Both electrodes were composed of 90% active material, 5% carbon black, and 5% polyvinylidene fluoride (PVDF), with Al and Cu used as current collectors. Electrode discs were punched in an Ar filled glovebox and dried under vacuum at 100 ^{o}C for 24 hours in a Buchi oven.

Ethylene Carbonate (EC, 99+%, Acros Organics) and Ethyl Methyl Carbonate (EMC, 99.95+%, Solvionic) were mixed in a volume:volume ratio of 3:7 and dried for 24 hours using dried molecular sieves (3 Å, beads, 8-12 mesh , Sigma Aldrich). The EC:EMC mixture water content before mixing was measured using Karl Fischer titration and was found to be 3.3 ppm. Lithium Hexafluorophosphate ($LiPF_6$, 98+ %, Fisher Scientific) was dried under dynamic vacuum at 1-2 mbar at 30 ^{o}C for 24 hours using a Buchi oven. Electrolytes were mixed to differing molalities (0.5-5m), with the EC:EMC mixture considered as the solvent. Glass fiber (GF) separators (borosilicate, grade GF/A, Whatman) were dried at 100 ^{o}C under dynamic vacuum at 1-2 mbar for 24 hours prior to use.

3.3.2 Electrochemical Cell Assembly and Protocols

2032-type coin cells (316 stainless steel, Cambridge Energy Solutions) were assembled in an Ar filled glovebox from ⌀9.5 mm NMC811 cathodes, ⌀9.5 mm LTO anodes, and ⌀9.5 mm GF separators soaked in 60 μL of electrolyte. A constant current of C/20 was applied to the coin cells until the potential across the full cell was 3.0 V, corresponding to the NMC811 reaching $\approx$ 4.5 V vs. Li/Li$^+$. The cell was held at this potential for 60 hours then discharged down to 2.3V, corresponding to the NMC811 reaching 3.8 V vs. Li/Li$^+$. At least two cells were assembled for each measurement to ensure reproducibility. These coin cells were then disassembled and used in subsequent XPS, XAS, NMR and ICP-OES measurements.

Three electrode Swagelok-type PFA (Perfluoroalkoxy alkane) cells with 316 stainless steel (Taybroh Alloys) plungers were assembled with ⌀9.5 mm NMC811 cathode and ⌀9.5 mm LTO anode with a ⌀9.5 mm GF separator soaked in 60 μL of electrolyte between them. Li metal was used as the reference electrode and was separated from the anode and cathode with another ⌀9.5 mm GF separator soaked in 60 μL of electrolyte. The specific capacity of NMC811 was assumed to be 190 mAh g^{-1} when cycled between 3 and 4.3 V

vs. Li/Li^+ as indicated by the manufacturer. Upon assembly, a constant current of C/20 was applied to the Swagelok-type cells until the potential of the NMC811 was 4.5V vs. Li/Li^+. Each cell was held at this potential for 60 hours then discharged down to 3.8V vs. Li/Li^+. EIS was then performed with the NMC811 at increasing potentials between 3.8 and 4.6 V vs. Li/Li^+ in steps of 0.1 V. EIS was performed in a frequency range of 500 kHz to 10 mHz with a peak to peak sinusoidal voltage perturbation of 5 mV. During the EIS measurement the potential of the NMC811 was not held at a constant value owing to the low C rate was used when charging the electrodes. Indeed, a very small potential decay over the course of the measurement was observed.

We note that the potentials of Li incorporation are not fixed on the absolute potential scale and are expected to vary with salt concentration.[23] However, from the Nernst equation, these potentials should all shift by the same amount for a given Li-ion activity, i.e. salt concentration, leading to no relative change. Indeed, a constant potential difference between the Li and LTO electrodes was observed for all salt concentrations in our three-electrode cell measurements.

To investigate the effect of a preformed CEI, three electrode Swagelok-type PFA cells were assembled in the same way and were subjected to a 60 h potential hold in 3 m electrolyte. The NMC811 electrodes were recovered and reassembled into fresh three electrode Swagelok-type PFA cells vs. LTO in 0.5 m electrolyte then subjected to a second 60 h potential hold.

3.3.3 Materials Characterization

The NMC811/LTO coin cells were disassembled in an Ar filled glovebox. The GF separator was extracted and soaked in 1 ml of deuterated dimethyl sulfoxide (DMSO-d_6) for 10 mins. The solution was transferred into an airtight J. Young NMR tube, and measured using an Oxford Instruments XPulse NMR spectrometer equipped with a 1.41 T magnet (ν_0 ^{1}H = 60 MHz). ^{1}H and ^{19}F NMR spectra were acquired for each of the different electrolyte concentrations following the potential holds. All spectra were recorded, locked and referenced to DMSO-d6.

The NMC811 and LTO electrodes were extracted and rinsed with DMC (99.99% anhydrous, Sigma Aldrich). The electrodes were then vacuum-dried for 12 hours at ambient temperature prior to inert transfer to the XPS equipment. XPS was performed using a PHI Versaprobe III XPS system generating focused, monochromatic Al Kα X-rays at 1486.6 eV, under ultrahigh vacuum (UHV) conditions ($< 10^{-8}$ mbar). A Shirley type background was subtracted from all spectra except for the Li 1s/TM 3p region. The probing depth, d, corresponding to the intensity of 95% of the emitted photoelectrons was calculated

as

$$d = 3\lambda \sin\theta$$

where λ is the inelastic mean free path, and θ is the angle between the sample surface and the analyzer.[24] An inelastic mean free path of 3.2 nm was calculated for photoelectrons emitted from the O 1s core level, assuming they travel through a model interphase consisting of polyethylene.[25] This assumes the surface is flat and the chemical composition is homogeneous, which although not the case for the composite electrodes used in this study, nevertheless serves as a reasonable approximation. The binding energies for each NMC811 sample were calibrated such that the C1s peak of adventitious carbon (C-C) occurs at 285.0 eV.

Cycled NMC811 electrodes were inertly transferred to endstation 2 of beamline B07B DLS for XAS measurements in both FY and TEY mode.[26] FY involves the detection of photons with attenuation lengths of several hundred nm and thus provides more bulk-sensitive information on the electrode's oxidation states, while TEY involves detection of electrons emitted from the sample surface and thus a maximum probing depth of $\approx$10 nm.[27,28]. Samples were loaded onto a sample stage in an Ar glovebox prior to inert transfer to the endstation. Reference NMC electrode spectra from the literature were used to energy calibrate the TM L-edges.[8,29] The O and F K-edges were energy calibrated to NiO and LiF respectively.[30] Spectra are normalized to the incident photon flux, measured using a biased collector plate opposite the surface of the final refocusing mirror. For some low intensity edges, sudden steps in the spectra related to periodic storage ring top-ups were removed during data analysis.

Elemental analysis was performed using ICP-OES (Thermoscientific). The cycled LTO electrodes and GF separators were placed in borosilicate glass vials. 250 μL of concentrated nitric acid (66%–68%) and 750 μL of ultra-pure water (Millipore) were then added to the vials. After three days, the digested samples were diluted to 10 ml with additional ultra-pure water and (in the case of the GF separator) centrifuged before measuring with ICP-OES. Calibration lines were generated for each element of interest from a concentration series made from a multi-element standard solution at each wavelength of interest. Emission wavelengths are chosen such that there was no interference from other elements in the sample, the standard or the matrix solution (2% nitric acid). The separator was carefully peeled away from the NMC811 electrode to minimise the amount of transition metals accidentally transferred between them on removal.

3.4 Results

3.4.1 Electrochemistry

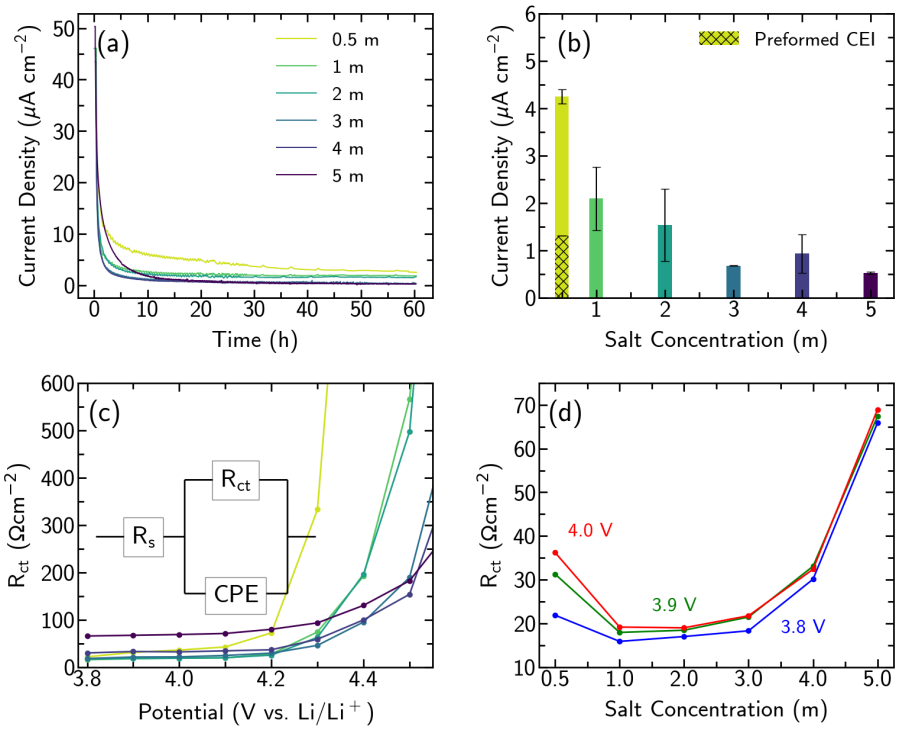

Figure 3.1: Comparison of electrochemical measurements conducted in three-electrode Swagelok-type cells with varying electrolyte salt concentrations ranging from 0.5 to 5m. (a) Depicts current density profiles observed during 60 hours of potential holds at 4.5 V versus Li/Li^+. (b) Illustrates the average oxidation current density recorded during the final 20 hours of potential holds across different electrolyte salt concentrations. The data are derived from two or more cells, with error bars representing the standard deviation. Additionally, data from a cell featuring a preformed CEI by holding in 3m electrolyte, subsequently subjected to 0.5m electrolyte, are included. (c) Shows the variation in R_{ct} with potential following 60 hours of potential holds. (d) Demonstrates the fluctuation of R_{ct} with salt concentration at different measurement potentials, using the same dataset as depicted in (c). Reprinted with permission from Ref [38]. Copyright 2024 American Chemical Society.

The potential of Li intercalation reactions is not fixed on the absolute potential scale and is expected to vary with salt concentration.[31] From the three-electrode cell measurements, whose results are displayed in Figure 3.1, it was observed that the relative potential differences for the Li reduction reaction between Li metal, LTO, and NMC811 were constant across all salt concentrations. Figure 3.1a shows the evolution of oxidation current density during 60 hours of potential holds (4.5 V vs. Li/Li^+) for three electrode Swagelok-type cells containing different salt concentrations (0.5 - 5m). The hold potential was selected to be above the onset of significant lattice oxygen release and accompanying RSL formation that is observed with $LiPF_6$ in EC:EMC (vol:vol 3:7) electrolytes.[6–8,11–13]

The initial current decay is largely attributable to relaxation of the electrolyte concentration polarization and the distribution of Li in the NMC811 particles as equilibrium is approached.[2] The current density is expected to become increasingly dominated by electrolyte oxidation reactions, and thus the average current density in the last 20 hours provides a measure of the electrolyte stability at the charged Ni-rich interface. Figure 3.1b shows that these average oxidation current densities decrease for the electrolytes with higher salt concentrations, indicating improved stability at the NMC811 interface.

To investigate how interfacial transport is affected by the electrolyte composition, potential-dependent EIS was conducted following the 60-hour potential holds in the same cells. The potential of the NMC811 versus Li/Li$^+$ was controlled using a Li metal reference electrode, with LTO serving as the counter electrode. An expression for R_{ct} at the NMC811 surface were derived from Nyquist plots by fitting the intermediate frequency portion to the simple equivalent circuit in Figure 3.1c as demonstrated in Figure 3.2.[2,10,32]

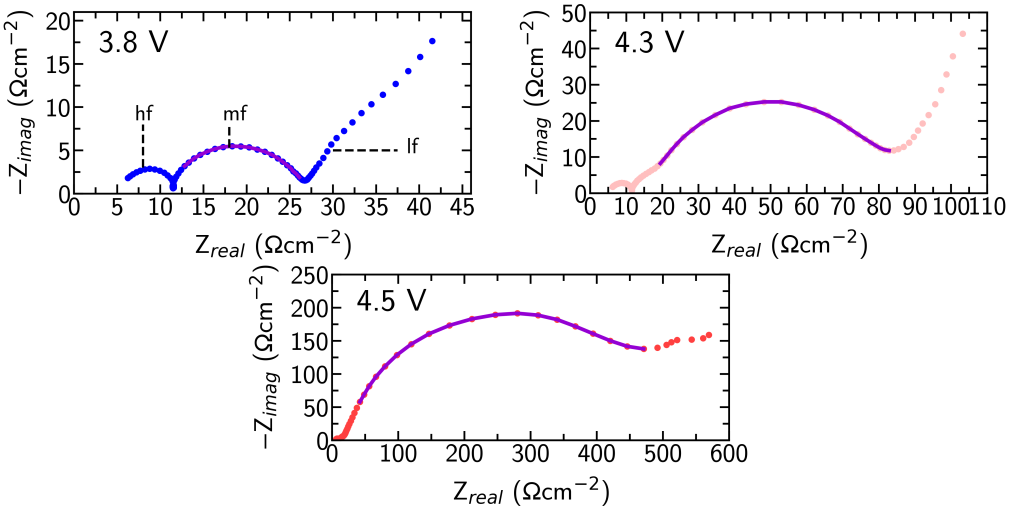

Figure 3.2: Nyquist plots of the NMC811 cathode are presented at various potentials versus Li/Li$^+$, measured in the three-electrode Swagelok cell configuration consisting of NMC811/LTO with Li metal serving as the reference electrode, utilizing a 1 m $LiPF_6$ in EC:EMC (vol:vol 3:7) electrolyte. To determine the charge transfer resistance, R_{ct}, from the measured Nyquist plots, the mid-frequency (mf) semicircle was fitted using the equivalent electrochemical circuit depicted in 3.1c. The purple line represents the fit of the equivalent circuit from 3.1c to the experimental data. Reprinted with permission from Ref [38]. Copyright 2024 American Chemical Society.

Figures 3.1c and 3.1d illustrate the dependence of R_{ct} on the electrode potential and electrolyte salt concentration, respectively. In interpreting these variations, expression 2.20 is useful.From Figure 3.1c, a clear dependence on state of charge (SoC) is evident, with R_{ct} significantly increasing at high potentials as the number of occupied lithium sites in the delithiated electrode (c_s) becomes negligible, typically referred to as a blocking condition. The potential at which R_{ct} dramatically increases varies for different electrolyte concentrations. For lower concentration electrolytes (0.5 m, 1 m, 2 m), this occurs

between 4.2 and 4.4 V versus Li/Li$^+$, while higher concentration electrolytes (3 m, 4 m, 5 m) maintain lower R_{ct} at high potentials, with the rapid increase in R_{ct} delayed to $\geq$ 4.4V. These trends stem from differences in the extent of RSL formation at the NMC811 surface. Oxygen loss and TM migration during RSL formation lead to increased occupation of lithium sites in the layered NMC by TM^{2+} ions,[33–36] thereby reducing the number of lithium-containing sites, $c_{s,max}$, such that the blocking condition is reached at lower potentials. Although k is typically assumed to be constant with potential, it may be affected by the nature of RSL and thereby also influence R_{ct}. Higher R_{ct} values are typically associated with more extensive RSL formation,[5,8–10,37] and thus the trends observed in Figure 3.1c indicate thinner/less-densified RSLs are formed in the more highly concentrated electrolytes.

Figure 3.1d examines the variation in R_{ct} with salt concentration at intermediate potentials where the SoC dependence is not expected to dominate. For each fixed potential, a U-shaped curve is evident, broadly following the behavior anticipated based on Equation 2.20,[32] with R_{ct} increasing for the lowest and highest salt concentrations. It is worth noting that some SoC dependent behavior is still noticeable for the 0.5m electrolyte. The rise in R_{ct} observed for the higher concentration electrolytes can be attributed to the electrolyte nearing its solubility limit, causing $(c_{e,max} - c_e)$ to become small, although Morasch et al. have observed changes in the rate constant k above $\approx$ 2.5m which may also contribute.[32] Similar trends in R_{ct} are observed for measurements of NMC811 that has undergone no potential hold to minimize RSL formation (see Figure 3.3). However, notable differences from Figure 3.1d are still present and may be attributed to the presence of the RSL and increased surface area associated with NMC particle cracking during the potential holds. Additionally, the larger CEI in the more highly concentrated electrolytes may contribute to the overpotential term in equation 2.20, thus affecting the measured R_{ct} values in the more highly concentrated electrolytes.

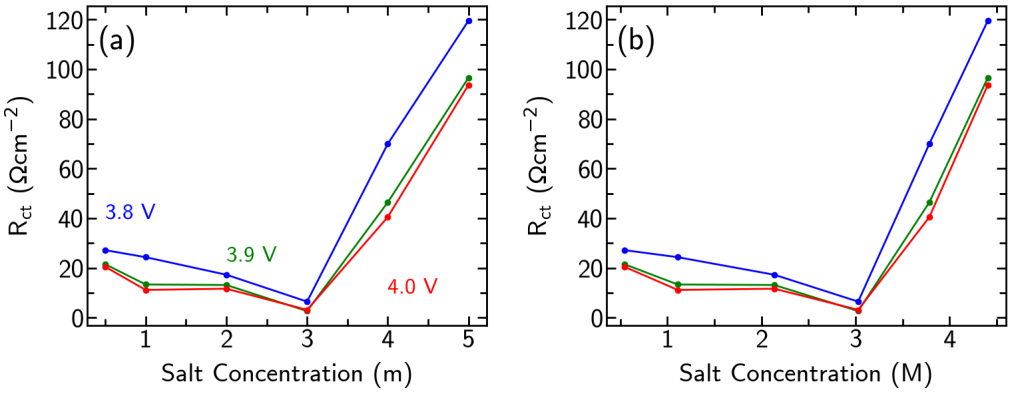

Figure 3.3: Variation in R_{ct} with electrolyte molality (a) and molarity (b) for pristine NMC811 electrodes directly cycled to 3.8V, 3.9V, and then 4.0V. Reprinted with permission from Ref [38]. Copyright 2024 American Chemical Society.

Furthermore, alongside the RSL, the CEI formed due to electrolyte decomposition is anticipated to impact the stability of the NMC811 interface.[8,24] To delve deeper into this phenomenon, 60-hour potential holds in a 3 m electrolyte were conducted to facilitate CEI formation, followed by subjecting the electrodes to a subsequent 60-hour potential hold in a 0.5 m electrolyte. In Figure 3.1b, a notably lower average oxidation current density is observed for the sample with the preformed CEI compared to those lacking this preforming step. Nevertheless, the oxidation current remains somewhat higher than in the case of the 3 m electrolyte. While some labile CEI components may be removed upon electrode retrieval and cell reassembly, this nonetheless implies strong suppression of the oxidation current by the preformed CEI. Hence, the reduced current densities observed at high salt concentrations are attributed to both the formation of the CEI and the enhanced stability of the electrolyte.

3.4.2 NMC811 Interfacial Characterisation

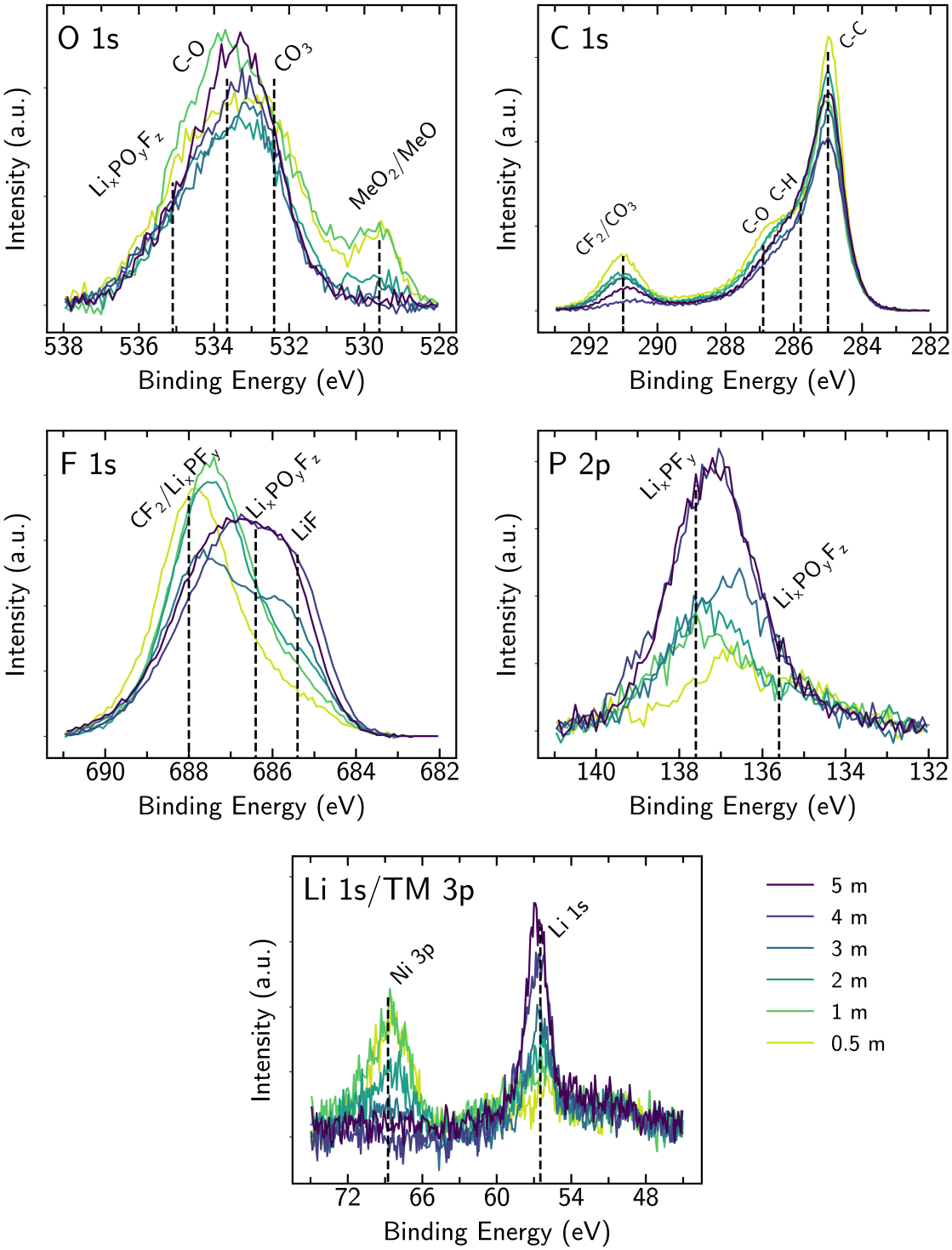

Figure 3.4: O 1s, C 1s, F 1s, P 2p and Li 1s/TM 3p core level spectra of NMC811 electrodes for the different salt concentrations (0.5 m - 5 m), following 60 h potential holds at 4.5 V and discharge to 3.8 V vs. Li/Li^+. Reprinted with permission from Ref [38]. Copyright 2024 American Chemical Society.

The composition of the CEI formed on the NMC811 electrodes after potential holds in various salt concentrations was analyzed using XPS, as depicted in Figure 3.4. Similar main spectral features are observed as those reported in our previous XPS investigation of cycled NMC811.[8]

The O 1s spectra show a clear decrease in the lattice oxygen peak (≈ 529.6 eV) with increasing salt concentration, indicating the formation of a thicker CEI.[8,38,39] We note this peak can have contributions from both the layered NMC811 (MeO_2, Me = Ni, Co, Mn) and RSL (MeO-like, Me = Ni, Co, Mn) which both show similar peak position. No clear trend with salt concentration is apparent for the other O 1s species. In the C 1s spectra, the intensities of peaks related to the PVDF binder (CF_2, ≈291.0 eV and C-H, ≈285.8 eV)[8] and carbon black (C-C, ≈285.0 eV)[38,40] also decrease with increasing salt concentration, indicating they are also attenuated by increasing CEI thickness. Similar to the O 1s spectra, the contributions of oxygen containing species to the C 1s spectra do not show clear trends, although the slight decrease in C-O contributions (≈286.9 eV) at higher salt concentrations is consistent with a thicker CEI attenuating C-O surface species associated with the carbon black or PVDF.

The F 1s spectra at lower electrolyte concentrations show strong PVDF binder contributions (CF_2 ≈ 688.0 eV).[8] Lower binding energy peaks, attributable to LiF (≈ 685.4 eV)[8,41] and $Li_xPO_yF_z$ (≈ 686.2 eV)[8], grow in intensity with increasing salt concentration, indicating more $LiPF_6$ decomposition occurs for the higher concentration electrolytes. This is also supported by the P 2p spectra where the intensities of both the Li_xPF_y feature (≈ 137.6 eV)[8,42,43] and $Li_xPO_yF_z$ feature (≈ 136.5 eV)[8,42,44] increase with salt concentration.

In the Li 1s/TM 3p core levels region, the Ni 3p peak (≈ 69.8 eV) intensity is seen to decrease with increasing salt concentration, whilst the Li 1s peak increases. This is consistent with a thicker CEI, rich in LiF/$Li_xPO_yF_z$ forming with increasing salt concentration, covering the NMC811. Although the Mn and Co 3p core levels are also expected in this region (≈50.0 eV and ≈61.0 eV respectively), they are not discernable above the noise due to their lower concentration in the cathode.

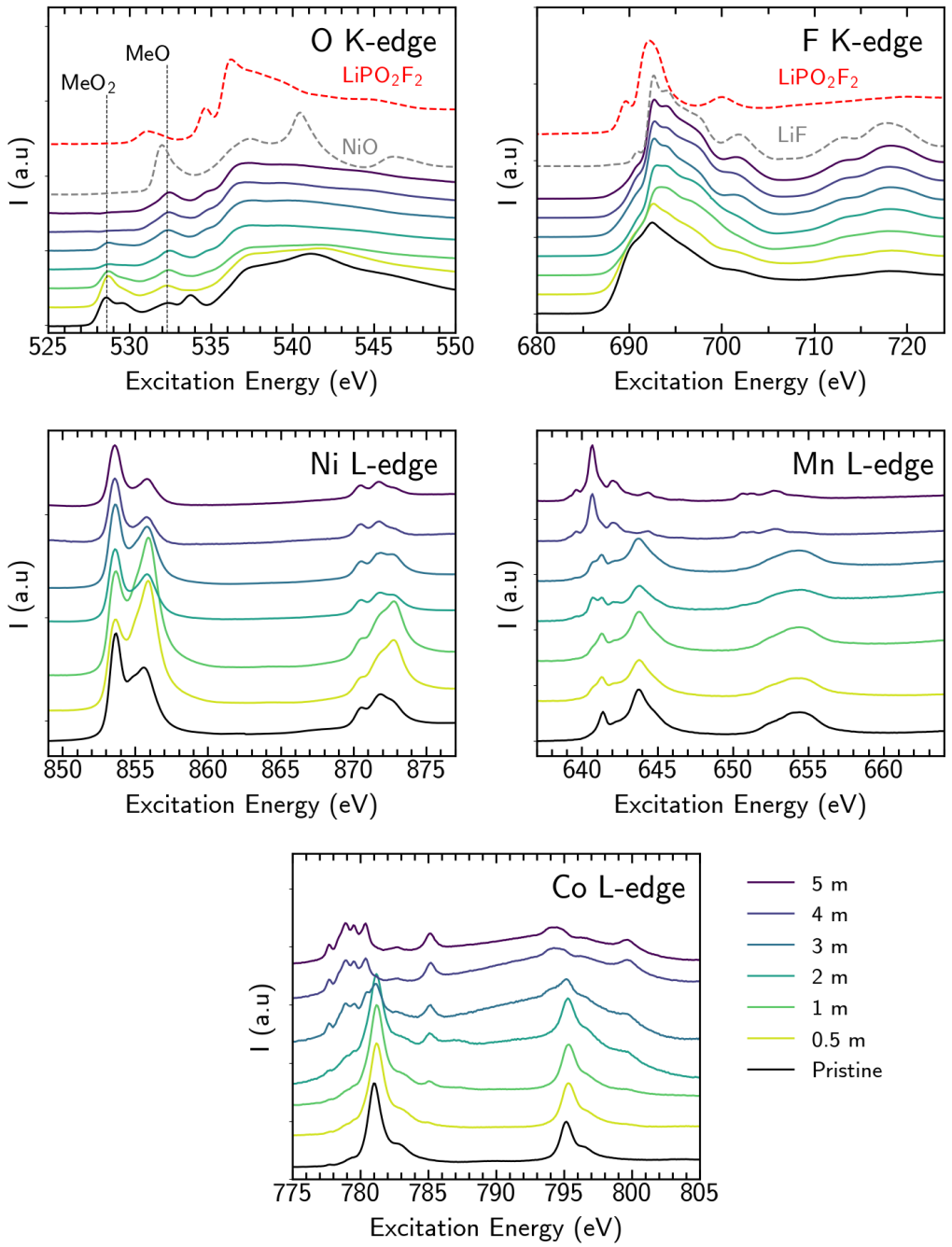

Figure 3.5: O K-edge, F K-edge, Ni L-edge, Mn L-edge and Co L-edge TEY-XAS spectra of NMC811 electrodes for the different salt concentrations (0.5 m - 5 m), following 60 h potential holds at 4.5 V and discharge to 3.8 V vs. Li/Li^+. The pristine NMC811 electrode spectra is also included for reference. Reprinted with permission from Ref [38]. Copyright 2024 American Chemical Society.

The nature of the CEI and RSL formed at the NMC811 surface at the different salt concentrations were further investigated using XAS. Interface-sensitive ($\approx$ 10 nm) TEY-XAS measurements of NMC811 electrodes in their pristine state and following 60 h potential holds in the different salt concentrations are shown in Figure 3.5. The pristine

electrodes exhibit pre-edge features at 528.6 and 529.6 eV associated with O 1s core electron excitations into hybridized TM 3d − O 2p orbitals of the layered NMC811 (MeO_2).[8,29,45] The peak at 532.3 eV is attributable to transitions to hybridized TM 3d − O 2p orbitals of the RSL (MeO-like),[8,46] and the peak at 533.8 eV is attributable to transitions to the π^* orbital of the C=O group of Li_2CO_3. Li_2CO_3 is a common surface contaminant formed as a result of residual CO_2 in the glovebox atmosphere, a reaction typically accompanied by some RSL formation.[8,29,45] The features above 536 eV are primarily associated with transitions to hybridized TM 4s − O 2p and higher unoccupied orbitals of NMC811, although there are also contributions from Li_2CO_3 in this region.[47,48] Simultaneously acquired bulk-sensitive FY-XAS (see Figure 3.6) shows only a weak RSL feature and no discernable Li_2CO_3 features, confirming these are surface species.

TEY-XAS following the potential holds shows no discernible feature at 533.8 eV for any electrolyte concentration, indicating Li_2CO_3 is electrochemically decomposed, chemically reacts with electrolyte decomposition products, or both.[15,49] Most notably, the intensity of the MeO_2 peaks is seen to decrease with increasing salt concentration, and is barely apparent at electrolyte concentrations of $\geq$4 m. Decreased intensity of these features has previously been attributed to oxygen loss from the NMC811,[41] however, as noted in our earlier work, thickening of the CEI layer must also be considered.[8] Based on the information depth of the TEY-XAS, we estimate a CEI thickness $\geq$ 10 nm is required for the disappearance of the MeO_2 peaks in the O K-edge and O 1s spectra.

The intensity of the MeO-like feature at 532.3 eV does not similarly decrease with increasing salt concentration, and even slightly grows. Although this could suggest RSL thickening, which is expected for NMC811 when cycled above 4.3 V vs. Li/Li^+ in standard 1 M electrolytes,[8,46] there is no corresponding increase in the MeO-like feature seen with FY-XAS (see Figure 3.6).

The XAS spectra of NMC811 electrodes after potential holds in the different salt concentrations are shown in Figure 3.6. The O K-edge spectra of the held electrodes exhibit a MeO_2 feature of similar intensity at all concentrations with no significant MeO feature. This confirms that the suppression of the MeO_2 feature at higher electrolyte concentrations seen in TEY-XAS (see Figure 3.5) is a near surface effect. Although the pristine electrode exhibits pre-edge features at 528.6 eV to the 529.6 eV, the 529.6 eV feature is less distinct in the potential held electrodes, consistent with their higher state of charge (discharged to 3.8 V vs. Li/Li^+ or $Li_{1-x}TMO_2$ x = 0.44). The F K-edge spectrum becomes more LiF-like with increasing salt concentration similar to the TEY spectra indicating a thick LiF layer forming on the NMC811 particle at the higher salt concentrations. The Ni and Co L-edges appear to remain predominantly in their oxidised state (+3) with increasing salt concentration, indicating the change in oxidation state observed in the TEY is due to

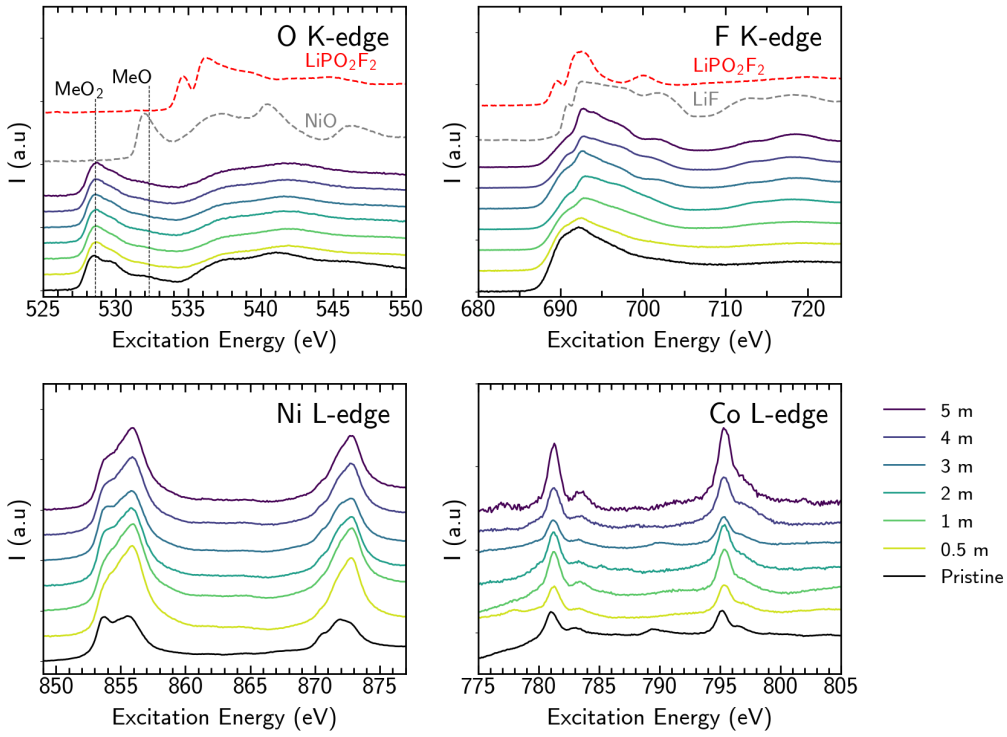

Figure 3.6: O K-edge, F K-edge, Ni L-edge and Co L-edge FY-XAS spectra of NMC811 electrodes for the different salt concentrations (0.5 m - 5 m), following 60 h potential holds at 4.5 V and discharge to 3.8 V vs. Li/Li$^+$. Reprinted with permission from Ref [38]. Copyright 2024 American Chemical Society.

reduced surface layer formation at the surface instead of bulk oxidation state changes. In the Ni L-edge, the 2 m and 3 m spectra have more pronounced low-energy shoulders at 853.7 eV compared to the 4 m and 5 m cases, suggesting a lower extent of RSL formation at the surface of the NMC811 in the more highly concentrated electrolytes. The Mn L-edge suffers from severe distortion associated with saturation and self-absorption effects in FY mode and has thus not been included.

XPS also shows attenuation of the O 1s peak associated with both MeO_2 and MeO with increasing salt concentration. Furthermore, additional contributions to the O K-edge particularly at 537.7, and 540.8 eV would be expected for RSL growth (see NiO reference spectrum). Instead the slight increase in intensity at 532.3 eV coincides with the emergence of features at 534.7 eV and 536.2 eV for electrolyte concentrations $\geq$2 m. These correspond closely to features seen in the $LiPO_2F_2$ reference spectrum and for other oxyfluorides.[50,51] Note that the peak at $\approx$ 531.0 eV in the $LiPO_2F_2$ TEY-XAS spectrum is not seen in the corresponding FY-XAS spectrum, indicating it relates to surface contamination. Phosphate containing species, which the XPS has indicated increasingly form at high salt concentrations, likely form alongside oxyfluorides and contribute to the peak at 532.3 eV.[52,53] These observations suggests that CEI rather than

RSL thickening is primarily responsible for the decreasing MeO_2 peak intensity, with the increased formation of $Li_xPO_yF_z$ species at high salt concentrations responsible for the growth in the features at 532.3, 535.0 and 537.0 eV.

The F K-edge spectrum of the pristine electrode can be assigned predominantly to PVDF, and this continues to contribute to the spectra measured for the low concentration electrolytes. For the 1 and 2 m electrolytes, additional broad features are apparent, particularly in the range 693-705 eV, that are qualitatively similar to reported line shapes for oxyfluorides,[51,54,55] and the $LiPO_2F_2$ reference spectrum. For higher salt concentrations, sharp features are increasingly apparent at 692.7, 694.1, and 701.6 eV, suggesting more LiF formation[30]. This further confirms the XPS interpretation that a thicker CEI, rich in $LiF/Li_xPO_yF_z$ forms at higher salt concentrations.

The Ni L-edge spectra exhibit sharp features in the L_3 edge at 853.7 eV and 856.4 eV. The lower-energy feature is primarily attributable to Ni^{2+}, and growth in the intensity of the higher-energy feature reflects higher Ni oxidation states, with this feature dominating for Ni^{4+}.[5,8,45,56,57]. In the Mn L-edge, the peaks at 641.4 eV and 643.8 eV are assigned to Mn^{4+}. The features observed at 639.6 and 642.1 eV have contributions from Mn^{3+} and Mn^{2+}, while the large feature at 640.7 eV indicates Mn^{2+}.[8,58,59] In the Co L-edge, the peak at 781.0 eV is attributed to Co^{3+} in the low spin state with the peaks at 777.7 eV, 778.9 eV, 779.5 eV and 780.4 attributable to Co^{2+} in the high spin state.[5,8,45,56] The Ni, Mn and Co L-edges thus suggest the TM species follow similar trends with increasing salt concentration. At lower salt concentrations the probed TM centres near the NMC811 surface are predominantly in their more oxidised form (+3 formal oxidation states for Ni and Co, +4 for Mn), while for higher salt concentrations Me^{2+} species increasingly contribute, with these dominating at the highest concentrations.

From Figure 3.4 it is apparent that the peaks associated with the NMC811 active material are strongly attenuated by CEI formation, and given the similar information depth of TEY-XAS (10 nm), the changes in the TM L-edges at higher electrolyte concentrations are attributable to more reduced TM species close to the surface of the NMC811, or incorporated into the CEI itself. More bulk sensitive ($\approx$ 100 nm) FY-XAS (see Figure 3.6) measurements show no corresponding increase in the MeO feature in the O K-edge, or more reduced species in the TM L-edges. Indeed the Ni L-edge measured in FY shows a noticeable drop in the intensity of the 853.7 eV feature for electrolyte concentrations above 3 m. This therefore suggests that rather than a more densified/thick RSL at higher electrolyte concentrations, as might be assumed based on the TEY-XAS alone, the TEY-XAS features arise from relatively low concentrations of TM^{2+} ions at the very surface of the NMC811 and dispersed within the thicker CEI, at concentrations where they are not readily detected in the XPS measurements.

Interestingly, the Co L-edge TEY-XAS of the high concentration electrolytes shows additional features at 785.2 eV and 799.7 eV (Figure 3.5), which are not seen in the FY-XAS (see Figure 3.6) or reference measurements of bulk CoO. These features have previously been attributed to Co coordinating certain ligand molecules and the associated metal-to-ligand charge transfer (MLCT).[60,61] The growth in intensity of these features with electrolyte concentration seen herein would potentially be consistent with trapping of dispersed Co^{2+} in the CEI and coordination with $P_xO_yF_z$ species. However, reports of similar features without the presence of Co have cast doubt on the attribution of these features,[62] and they may instead relate to the Ba $M_{4,5}$-edge which exhibits a very similar spin-orbit splitting.[63,64] Indeed, XPS measurements of the Ba 3d core level for the GF separator (see Figure 3.7) confirm the presence of Ba. Moreover, the growth in intensity of the 785.2 eV and 799.7 eV features with electrolyte concentration correlates closely with other evidence of separator degradation (see below).

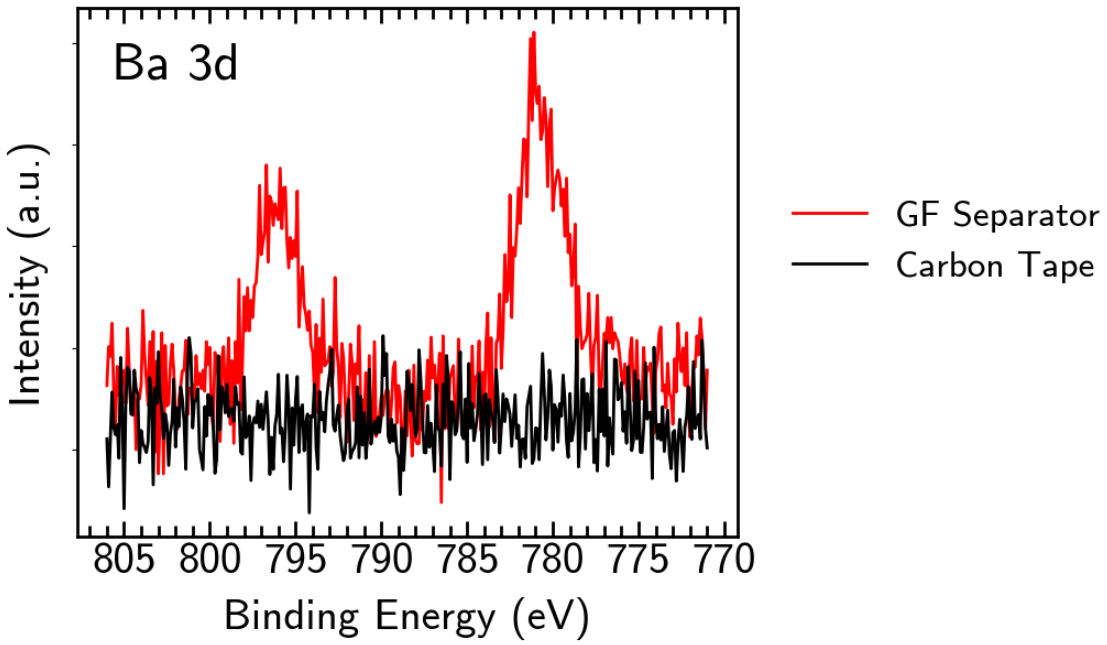

Figure 3.7: Ba 3d core level spectra of pristine GF separator and carbon tape support used to mount GF separator on sample stage. Reprinted with permission from Ref [38]. Copyright 2024 American Chemical Society.

3.4.3 Soluble Electrolyte Decomposition Products

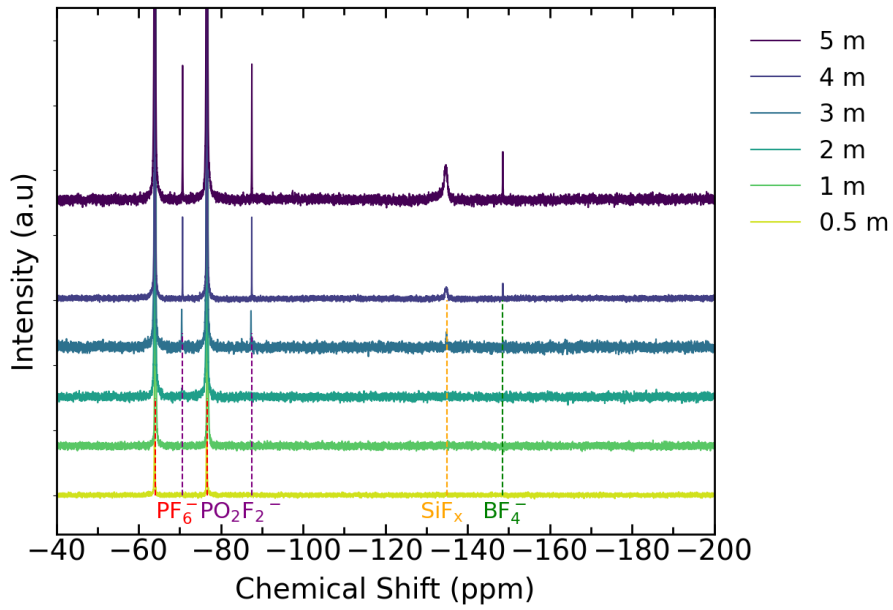

Figure 3.8: ^{19}F NMR spectra for the different salt concentrations (0.5 m - 5 m), following 60 h potential holds at 4.5 V and discharge to 3.8 V vs. Li/Li$^+$. Reprinted with permission from Ref [38]. Copyright 2024 American Chemical Society.

Soluble degradation products in the electrolyte extracted from NMC811/LTO cells after the 60 h potentiostatic holds were investigated by ^{19}F NMR spectroscopy. From Figure 3.8, a doublet centered at -70.5 ppm (d, $^1J_{P-F} = 710$ Hz) is seen for all salt concentrations which corresponds to the presence of the PF_6^- ions. At salt concentrations of $\geq$3 m, a doublet centered at -78.5 ppm (d, $^1J_{P-F} = 955$ Hz) alongside singlets at -134.9 ppm (s) and -148.6 ppm (s) emerge, attributable to $PO_2F_2^-$, SiF_x and BF_4^- respectively[15,65]. SiF_x and BF_4^- are expected to form by reaction of HF in the electrolyte with the GF separator.[15,65] The stronger intensity of these features reflects more separator degradation occurs in the more highly concentrated electrolytes, indicating more HF is generated in the electrolyte. We note that HF is not discernable in the ^{19}F (s, -171.7 ppm)[15,65,66] or ^{1}H (see Figure 3.9) NMR spectra for any of the electrolyte concentrations. This suggests that the HF formed is continuously consumed by reaction with species present in the cells rather than accumulating to high levels.

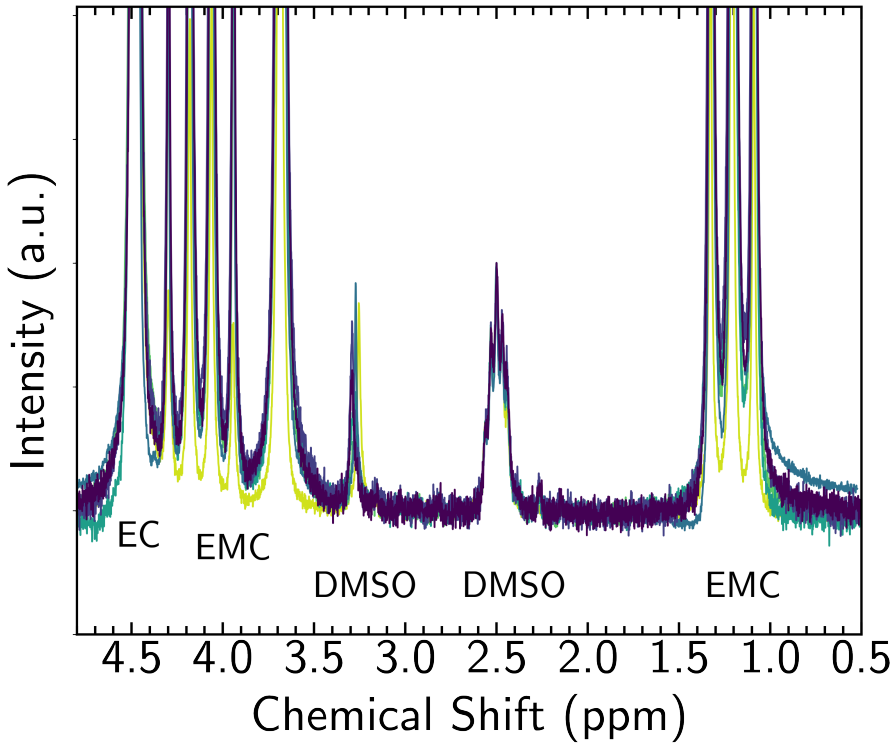

Figure 3.9: ^{1}H NMR spectra for the different salt concentrations (0.5 m - 5 m), following 60 h potential holds at 4.5 V and discharge to 3.8 V vs. Li/Li^{+}. Reprinted with permission from Ref [38]. Copyright 2024 American Chemical Society.

3.4.4 Transition Metal Dissolution and Crossover

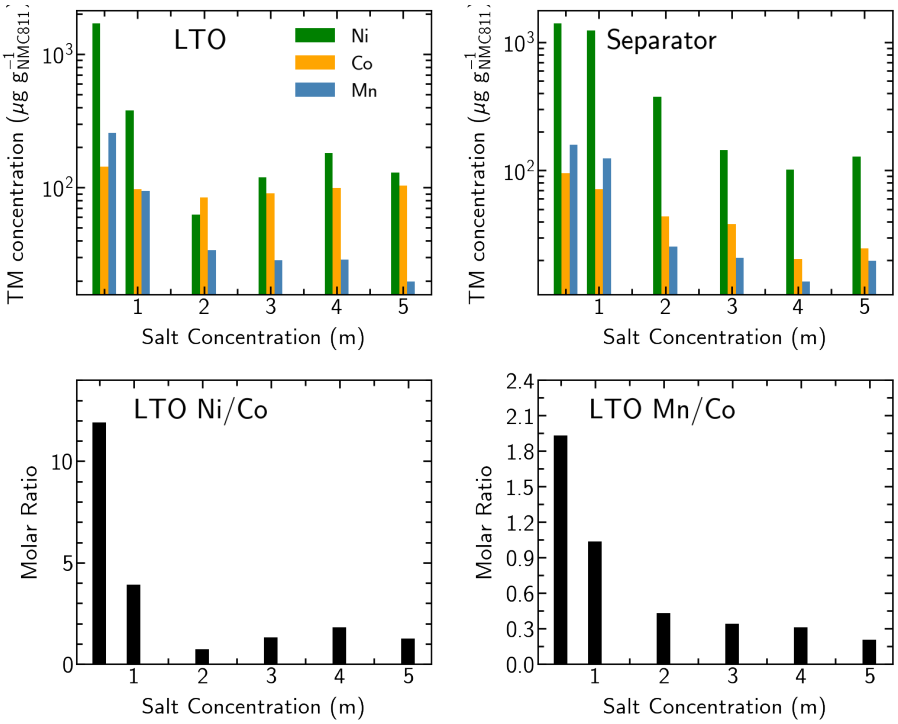

Figure 3.10: ICP-OES of LTO counter electrode and GF separator for the different salt concentrations (0.5 m - 5 m), following 60 h potential holds at 4.5 V and discharge to 3.8 V vs. Li/Li^+ and molar ratios for deposited TMs on the LTO electrode. Reprinted with permission from Ref [38]. Copyright 2024 American Chemical Society.

To investigate the extent of TM dissolution from the cathode as a result of the potential holds, the LTO anode and GF separator were extracted from the coin cells for ICP-OES measurements. Figure 3.10 shows the concentrations of Co, Mn and Ni deposited on the LTO electrode and accumulated in the separator. The concentrations of dissolved TMs in both the LTO electrode and the separator, are seen to decrease significantly for the higher-concentration electrolytes. The drop off in TM concentration with electrolyte salt concentration is more rapid for the LTO electrode than the GF separator, suggesting that the higher salt concentration not only suppresses TM dissolution from the cathode (sum of LTO and separator TM concentrations) but also influences TM deposition at the LTO electrode.

Considering the high molar ratios of Ni:Co and Mn:Co from the measured TM concentrations on the LTO electrodes, the amount of Ni and Mn crossover is found to be more strongly suppressed compared to Co at higher salt concentrations, with ratios well below the 8:1 and 1:1 expected based on the cathode composition. The molar ratios of TMs in the GF separator show a similar trend with lower Ni:Co and Mn:Co ratios for the higher concentration electrolytes as demonstrated in Figure 3.11, however the differences are less

pronounced than for the LTO. Thus, for the higher concentration electrolytes, not only do Ni and Mn appear to dissolve less readily from the cathode than Co, their incorporation from the electrolyte into the LTO electrode is also more suppressed.

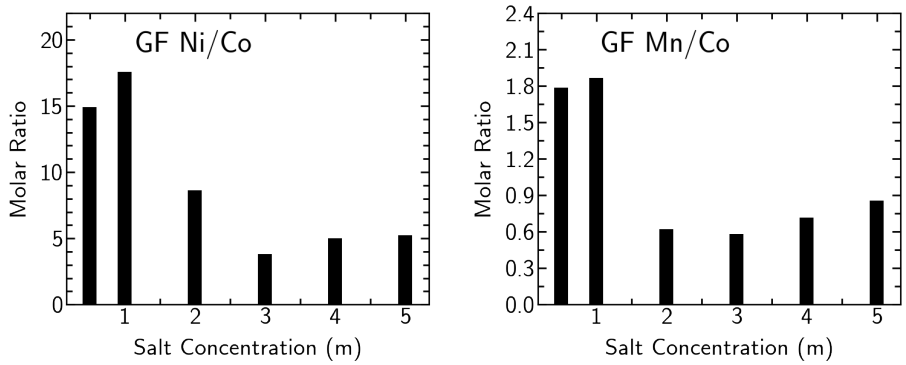

Figure 3.11: Molar ratios for accumulated TMs in the GF separator calculated based on Figure 3.10. Reprinted with permission from Ref [38]. Copyright 2024 American Chemical Society.

3.5 Discussion

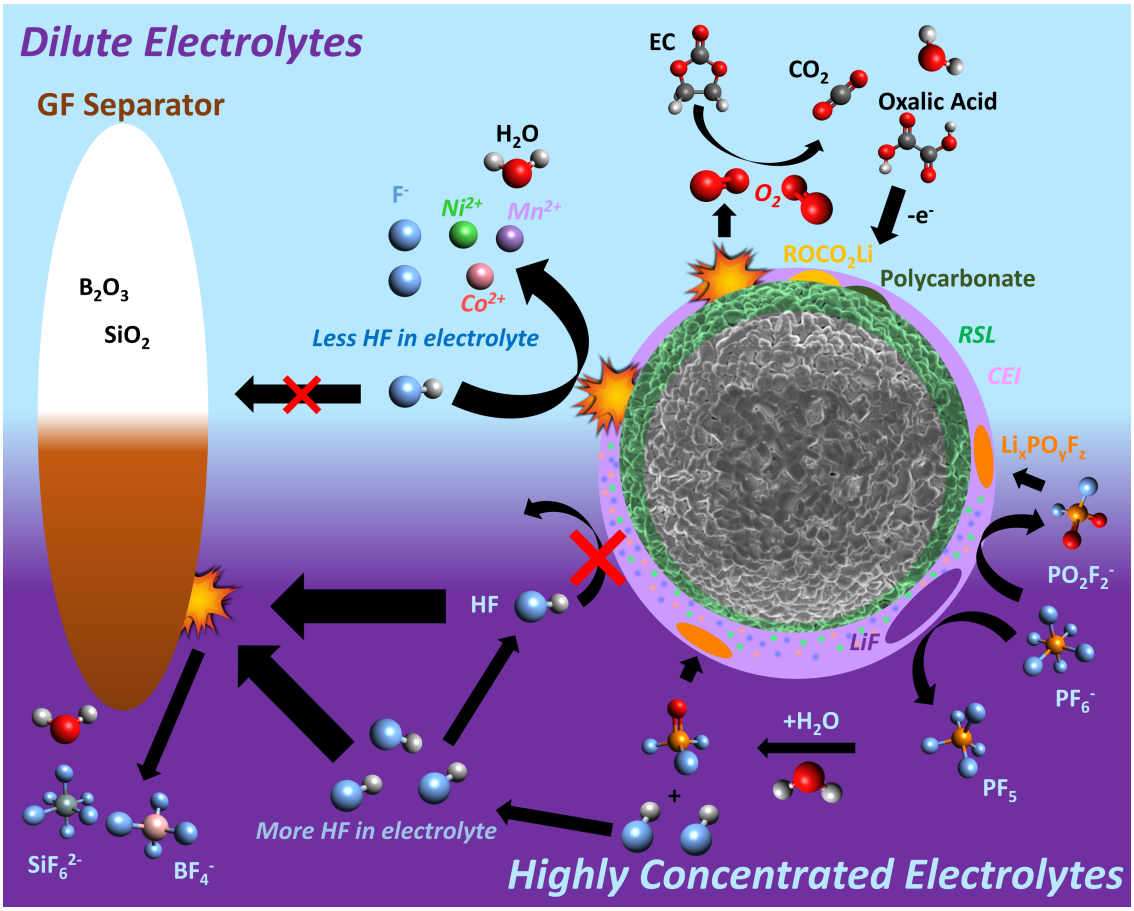

Figure 3.12: Illustration of the reaction mechanisms between NMC811 and the electrolyte. Reprinted with permission from Ref [38]. Copyright 2024 American Chemical Society.

The 60 h potential holds performed here reveal the dependence of electrolyte stability on salt concentration at high potentials (Figure 3.1), with the oxidation current associated with electrolyte decomposition suppressed at higher salt concentrations. From Figure 3.1 b, it is apparent that preforming the CEI in a higher concentration (3m) electrolyte partially suppresses the oxidation current observed in a 0.5 m electrolyte, confirming the important role of the CEI. However the current is still somewhat higher than that seen during the 3 m sample hold, suggesting that stabilisation of the solvent components in more highly concentrated electrolytes also plays a role. Furthermore, lower R_{ct} values are observed with the high concentration electrolytes at high voltages indicating less extensive RSL formation.

In order to rationalise these improvements in electrolyte stability, and R_{ct} values, we now consider the results of detailed chemical characterisation of the cathode, electrolyte, and species that crossover to the anode in the context of prior literature. Figure 3.12

summarises how the contributions from key chemical processes differ between the lower and higher concentration electrolytes.

For NMC811 in lower-concentration electrolytes, significant lattice oxygen release and accompanying RSL thickening is expected for the hold potentials used herein (4.5 V vs. Li/Li^+).[3,6–8,11–13] Consistent with this, TEY-XAS shows a MeO feature at 532.3 eV in the O K-edge, and potential-dependent EIS measurements show a rapid rise in R_{ct} at quite low potentials reflecting the limited availability of Li vacancies due to significant RSL formation.[5,9,10] Release of $^1O_2$ from NMC at high potentials[6–8,11–13] has been implicated in chemically oxidising EC and linear carbonate molecules to yield polycarbonate and $ROCO_2Li$ species atop the RSL.[15,65] The XPS measurements herein are consistent with the presence of such species for all electrolyte concentrations studied (Figure 3.4). At low $LiPF_6$ concentrations, XPS and XAS reveal that the CEI is relatively thin with limited LiF content, and NMR indicates minimal electrolyte salt degradation occurs. This thin, organic-rich CEI allows HF and other acidic species, such as H_3PO_4, to attack the RSL, leading to TM dissolution into the electrolyte and crossover to the anode as seen with ICP-OES. MeO can react with various acidic species forming water and Me^{+2} species:[67,68]

$$MeO + 2H^+ \longrightarrow Me^{2+} + H_2O \quad Me = Ni, Co, Mn \tag{3.1}$$

For higher $LiPF_6$ concentrations, XPS and XAS reveal a much thicker CEI is formed that is rich in $Li_xPO_yF_z$, and increasingly LiF at the highest concentrations. Strikingly similar CEI compositions are observed for the 4 m and 5 m electrolytes, distinct from those seen at lower salt concentrations. Since 4 m electrolyte is very close to the solubility limit of the salt, while the 5 m electrolyte is saturated with salt the similarity suggests the solubility limit lies just above 4 m. Furthermore, comparable degrees of oxidation current passivation are seen for the $\geq$3 m electrolytes suggesting a transition in behaviour around this concentration. This coincides with the concentration at which the proportion of free-solvent molecules becomes very low, with the formation of CIPs and AGGs dominating.[69,70] Li^+ coordination has been reported to lower the HOMO energies of solvent molecules, increasing their oxidative stability.[71–74] We therefore suggest that the change in the solvation structures present at $\geq$3 m favours PF_6^- anion decomposition over solvent decomposition, leading to a more $Li_xPO_yF_z$/LiF-rich CEI. The greater CEI thickness seen at higher concentrations is consistent with the increased chemical potential of the PF_6^- resulting in more LiF formation atop the RSL alongside the formation of PF_5:[15,75–77]

$$LiPF_6 \rightleftharpoons LiF + PF_5 \tag{3.2}$$

The attenuation of TM core levels in XPS for the higher salt concentrations electrolytes indicates the overall amount of TMs in the thicker CEIs is low, with TEY-XAS showing

an increasing proportion of Me^{2+} species. More bulk sensitive FY-XAS also indicates a lesser extent of RSL formation, consistent with the formation of MeF_2 and $Me_xPO_yF_z$ at the RSL surface or within the thick CEI. The formation of these components can be attributed to increased reaction of the RSL surface with $LiPF_6$ and PF_5, and other products of these reactions are indeed seen with XPS (LiF) and NMR ($PO_2F_2^-$):

$$MeO + LiPF_6 \longrightarrow MeF_2 + LiF + POF_3 \tag{3.3}$$

$$MeO + PF_5 \longrightarrow MeF_2 + POF_3 \tag{3.4}$$

$$2MeO + LiPF_6 \longrightarrow 2MeF_2 +$$

PO_yF_z-species can also be produced by increased $LiPF_6$ hydrolysis at the higher salt concentrations, related to trace moisture in the electrolyte, including that arising from solvent molecule oxidation:[15,77]

$$LiPF_6 + 2H_2O \longrightarrow LiPO_2F_2 + 4HF \tag{3.6}$$

$$PF_5 + H_2O \longrightarrow POF_3 + 2HF \tag{3.7}$$

These PO_yF_z-species can be further hydrolysed to produce other acidic species, such as H_3PO_4,[78] in addition to reacting with the cathode surface to yield insoluble $Li_xPO_yF_z$ components of the CEI. These acidic species, including HF, have already been discussed above in the context of TM dissolution.

Important to the improved stability seen for the higher-concentration electrolytes is the protection afforded by the thicker $Li_xPO_yF_z$- and LiF-rich CEI formed, that leads to thinner/less-densified RSLs with lower R_{ct} values, less TM dissolution and lower oxidation currents at high potentials. EC from the electrolyte has been suggested to enhance oxygen loss from NMC leading to more cathode surface degradation.[3] For higher concentration electrolytes, the lesser extent of RSL formation seen by FY-XAS may relate to the reduced access of EC to the NMC surface as well as the increased stabilisation of EC in high concentration electrolytes. The thicker CEI is also seen to limit RSL attack by acidic species, with much lower TM dissolution and crossover observed by ICP-OES. This inevitably means HF consumption at the cathode is suppressed, and thus more HF is available to degrade the GF separator in the more highly concentrated electrolytes, accounting for the higher concentrations of BF_4^- and SiF_x species observed in NMR.[15,65]

$$B_2O_3 + 8HF \longrightarrow 2BF_4^- + 3H_2O + 2H^+ \tag{3.8}$$

$$SiO_2 + xHF \longrightarrow H_{x-4}SiF_x + 2H_2O \quad (x = 4, 5, 6) \tag{3.9}$$

It should however be noted that GF separators are not widely used in commercial LIBs and thus in this context this form of degradation may be less relevant.

3.6 Conclusion

In this work, new understanding of the effect of $LiPF_6$ salt concentration on the interfacial reactivity of charged Ni-rich NMC cathodes in carbonate based electrolytes is unveiled by combining electrochemical measurements with chemical analysis of the cathodes interfaces and electrolyte. The degree of electrolyte oxidation at Ni-rich NMC electrodes is found to be suppressed by increasing salt concentration. The more highly concentrated electrolytes lead to a more $Li_xPO_yF_z$-/LiF-rich CEI which limits the access of solvent molecules and acidic species to the cathode surface resulting in thinner RSLs with lower charge transfer impedances, less TM dissolution into the electrolyte and lower parasitic oxidation currents observed at high potentials. The understanding developed of the composition and structure of the beneficial CEI formed is expected to inform the rational design of new electrolyte formulations which can stabilize the cathode electrolyte interface, a crucial step toward enabling the widespread adoption of high voltage Ni-rich cathodes in electric vehicles and grid-scale energy storage systems. This includes the identification of suitable, low cost additives to achieve similar improvements in stability to those observed with highly concentrated electrolytes, without sacrificing the benefits of lower concentration $LiPF_6$ based electrolytes i.e. lower salt cost, higher ionic conductivity, fewer negative environmental impacts.

Bibliography

[1] Amnesty International, "Democratic Republic of Congo: "This is what we die for": Human rights abuses in the Democratic Republic of the Congo power the global trade in cobalt," 2016.

[2] W. M. Dose, I. Temprano, J. P. Allen, E. Björklund, C. A. O'Keefe, W. Li, B. L. Mehdi, R. S. Weatherup, M. F. De Volder, and C. P. Grey, "Electrolyte Reactivity at the Charged Ni-Rich Cathode Interface and Degradation in Li-Ion Batteries," *ACS Applied Materials and Interfaces*, vol. 14, no. 11, 2022.

[3] W. M. Dose, W. Li, I. Temprano, C. A. O'Keefe, B. Layla Mehdi, M. F. L. De Volder, and C. P. Grey, "Onset Potential for Electrolyte Oxidation and Ni-Rich Cathode Degradation in Lithium-Ion Batteries," *ACS Energy Letters*, vol. 7, pp. 3524–3530, 9 2022.

[4] L. Giordano, P. Karayaylali, Y. Yu, Y. Katayama, F. Maglia, S. Lux, and Y. Shao-Horn, "Chemical Reactivity Descriptor for the Oxide-Electrolyte Interface in Li-Ion Batteries," *Journal of Physical Chemistry Letters*, vol. 8, no. 16, 2017.

[5] F. Lin, I. M. Markus, D. Nordlund, T. C. Weng, M. D. Asta, H. L. Xin, and M. M. Doeff, "Surface reconstruction and chemical evolution of stoichiometric layered cathode materials for lithium-ion batteries," *Nature communications*, vol. 5, 2014.

[6] R. Jung, M. Metzger, F. Maglia, C. Stinner, and H. A. Gasteiger, " Oxygen Release and Its Effect on the Cycling Stability of LiNi x Mn y Co z O 2 (NMC) Cathode Materials for Li-Ion Batteries ," *Journal of The Electrochemical Society*, vol. 164, no. 7, 2017.

[7] D. Streich, C. Erk, A. Guéguen, P. Müller, F. F. Chesneau, and E. J. Berg, "Operando Monitoring of Early Ni-mediated Surface Reconstruction in Layered Lithiated Ni-Co-Mn Oxides," *Journal of Physical Chemistry C*, vol. 121, no. 25, 2017.

[8] E. Björklund, C. Xu, W. M. Dose, C. G. Sole, P. K. Thakur, T. L. Lee, M. F. De Volder, C. P. Grey, and R. S. Weatherup, "Cycle-Induced Interfacial Degrada-

tion and Transition-Metal Cross-Over in LiNi0.8Mn0.1Co0.1O2-Graphite Cells," *Chemistry of Materials*, vol. 34, no. 5, 2022.

[9] D. Dees, E. Gunen, D. Abraham, A. Jansen, and J. Prakash, "Alternating Current Impedance Electrochemical Modeling of Lithium-Ion Positive Electrodes," *Journal of The Electrochemical Society*, vol. 152, no. 7, p. A1409, 2005.

[10] W. M. Dose, J. K. Morzy, A. Mahadevegowda, C. Ducati, C. P. Grey, and M. F. De Volder, "The influence of electrochemical cycling protocols on capacity loss in nickel-rich lithium-ion batteries," *Journal of Materials Chemistry A*, vol. 9, no. 41, 2021.

[11] R. Jung, M. Metzger, F. Maglia, C. Stinner, and H. A. Gasteiger, "Chemical versus electrochemical electrolyte oxidation on NMC111, NMC622, NMC811, LNMO, and conductive carbon," *Journal of Physical Chemistry Letters*, vol. 8, no. 19, 2017.

[12] A. T. Freiberg, M. K. Roos, J. Wandt, R. De Vivie-Riedle, and H. A. Gasteiger, "Singlet Oxygen Reactivity with Carbonate Solvents Used for Li-Ion Battery Electrolytes," *Journal of Physical Chemistry A*, vol. 122, no. 45, 2018.

[13] J. Wandt, A. T. Freiberg, A. Ogrodnik, and H. A. Gasteiger, "Singlet oxygen evolution from layered transition metal oxide cathode materials and its implications for lithium-ion batteries," *Materials Today*, vol. 21, no. 8, 2018.

[14] M. Metzger, B. Strehle, S. Solchenbach, and H. A. Gasteiger, " Origin of H 2 Evolution in LIBs: H 2 O Reduction vs. Electrolyte Oxidation ," *Journal of The Electrochemical Society*, vol. 163, no. 5, 2016.

[15] B. L. Rinkel, D. S. Hall, I. Temprano, and C. P. Grey, "Electrolyte oxidation pathways in lithium-ion batteries," *Journal of the American Chemical Society*, vol. 142, no. 35, 2020.

[16] S. Solchenbach, M. Metzger, M. Egawa, H. Beyer, and H. A. Gasteiger, " Quantification of PF 5 and POF 3 from Side Reactions of LiPF 6 in Li-Ion Batteries ," *Journal of The Electrochemical Society*, vol. 165, no. 13, 2018.

[17] S. Wiemers-Meyer, M. Winter, and S. Nowak, "Mechanistic insights into lithium ion battery electrolyte degradation-a quantitative NMR study," 2016.

[18] S. Wilken, M. Treskow, J. Scheers, P. Johansson, and P. Jacobsson, "Initial stages of thermal decomposition of LiPF6-based lithium ion battery electrolytes by detailed Raman and NMR spectroscopy," *RSC Advances*, vol. 3, no. 37, 2013.

[19] C. Jayawardana, N. Rodrigo, B. Parimalam, and B. L. Lucht, "Role of Electrolyte Oxidation and Difluorophosphoric Acid Generation in Crossover and Capacity Fade in Lithium Ion Batteries," *ACS Energy Letters*, vol. 6, no. 11, 2021.

[20] Y. Tesfamhret, H. Liu, E. J. Berg, and R. Younesi, "The role of ethylene carbonate (EC) and tetramethylene sulfone (SL) in the dissolution of transition metals from lithium-ion cathodes," *RSC Advances*, vol. 13, no. 30, 2023.

[21] J. A. Gilbert, I. A. Shkrob, and D. P. Abraham, "Transition Metal Dissolution, Ion Migration, Electrocatalytic Reduction and Capacity Loss in Lithium-Ion Full Cells," *Journal of The Electrochemical Society*, vol. 164, no. 2, 2017.

[22] J. C. Hestenes, J. T. Sadowski, R. May, and L. E. Marbella, "Transition Metal Dissolution Mechanisms and Impacts on Electronic Conductivity in Composite LiNi0.5Mn1.5O4 Cathode Films," *ACS Materials Au*, vol. 3, no. 2, 2023.

[23] S. Ko, Y. Yamada, and A. Yamada, "A 62 m K-ion aqueous electrolyte," *Electrochemistry Communications*, vol. 116, 2020.

[24] S. Malmgren, K. Ciosek, M. Hahlin, T. Gustafsson, M. Gorgoi, H. Rensmo, and K. Edström, "Comparing anode and cathode electrode/electrolyte interface composition and morphology using soft and hard X-ray photoelectron spectroscopy," *Electrochimica Acta*, vol. 97, 2013.

[25] L. R. Painter, E. T. Arakawa, M. W. Williams, and J. C. Ashley, "Optical properties of polyethylene: Measurement and applications," *Radiation Research*, vol. 83, no. 1, 1980.

[26] D. C. Grinter, F. Venturini, P. Ferrer, M. A. van Spronsen, R. Arrigo, W. Quevedo Garzon, K. Roy, A. I. Large, S. Kumar, and G. Held, "The Versatile Soft X-Ray (VerSoX) Beamline at Diamond Light Source," *Synchrotron Radiation News*, vol. 35, no. 3, 2022.

[27] M. Abbate, J. B. Goedkoop, F. M. de Groot, M. Grioni, J. C. Fuggle, S. Hofmann, H. Petersen, and M. Sacchi, "Probing depth of soft x-ray absorption spectroscopy measured in total-electron-yield mode," *Surface and Interface Analysis*, vol. 18, no. 1, 1992.

[28] B. H. Frazer, B. Gilbert, B. R. Sonderegger, and G. De Stasio, "The probing depth of total electron yield in the sub-keV range: TEY-XAS and X-PEEM," *Surface Science*, vol. 537, no. 1-3, 2003.

[29] C. Tian, D. Nordlund, H. L. Xin, Y. Xu, Y. Liu, D. Sokaras, F. Lin, and M. M. Doeff, " Depth-Dependent Redox Behavior of LiNi 0.6 Mn 0.2 Co 0.2 O 2 ," *Journal of The Electrochemical Society*, vol. 165, no. 3, 2018.

[30] J. E. N. Swallow, M. W. Fraser, N.-J. H. Kneusels, J. F. Charlton, C. G. Sole, C. M. E. Phelan, E. Björklund, P. Bencok, C. Escudero, V. Pérez-Dieste, C. P. Grey, R. J. Nicholls, and R. S. Weatherup, "Revealing solid electrolyte interphase formation through interface-sensitive Operando X-ray absorption spectroscopy," *Nature Communications*, vol. 13, no. 1, p. 6070, 2022.

[31] S. Ko, T. Obukata, T. Shimada, N. Takenaka, M. Nakayama, A. Yamada, and Y. Yamada, "Electrode potential influences the reversibility of lithium-metal anodes," *Nature Energy*, vol. 7, no. 12, 2022.

[32] R. Morasch, H. A. Gasteiger, and B. Suthar, "Li-Ion Battery Active Material Impedance Analysis I: Comparison of Measured NCM 111 Kinetics with Butler-Volmer Equation Based Predictions," *Journal of The Electrochemical Society*, vol. 170, no. 8, 2023.

[33] S. Zheng, R. Huang, Y. Makimura, Y. Ukyo, C. A. J. Fisher, T. Hirayama, and Y. Ikuhara, "Microstructural Changes in LiNi _{0.8} Co _{0.15} Al _{0.05} O ₂ Positive Electrode Material during the First Cycle," *Journal of The Electrochemical Society*, vol. 158, pp. A357–A362, 4 2011.

[34] S. Hwang, W. Chang, S. M. Kim, D. Su, D. H. Kim, J. Y. Lee, K. Y. Chung, and E. A. Stach, "Investigation of changes in the surface structure of LixNi 0.8Co0.15Al0.05O2 cathode materials induced by the initial charge," *Chemistry of Materials*, vol. 26, no. 2, 2014.

[35] P. Mukherjee, P. Lu, N. Faenza, N. Pereira, G. Amatucci, G. Ceder, and F. Cosandey, "Atomic Structure of Surface-Densified Phases in Ni-Rich Layered Compounds," *ACS Applied Materials and Interfaces*, vol. 13, no. 15, 2021.

[36] F. Kong, C. Liang, L. Wang, Y. Zheng, S. Perananthan, R. C. Longo, J. P. Ferraris, M. Kim, and K. Cho, "Kinetic Stability of Bulk LiNiO2 and Surface Degradation by Oxygen Evolution in LiNiO2-Based Cathode Materials," *Advanced Energy Materials*, vol. 9, no. 2, 2019.

[37] R. Weber, A. J. Louli, K. P. Plucknett, and J. R. Dahn, " Resistance Growth in Lithium-Ion Pouch Cells with LiNi 0.80 Co 0.15 Al 0.05 O 2 Positive Electrodes and Proposed Mechanism for Voltage Dependent Charge-Transfer Resistance ," *Journal of The Electrochemical Society*, vol. 166, no. 10, 2019.

[38] Y. Zhu, Y. Li, M. Bettge, and D. P. Abraham, "Positive Electrode Passivation by LiDFOB Electrolyte Additive in High-Capacity Lithium-Ion Cells," *Journal of The Electrochemical Society*, vol. 159, no. 12, 2012.

[39] E. Björklund, E. Wikner, R. Younesi, D. Brandell, and K. Edström, "Influence of state-of-charge in commercial LiNi0.33Mn0.33Co0.33O2/LiMn2O4-graphite cells analyzed by synchrotron-based photoelectron spectroscopy," *Journal of Energy Storage*, vol. 15, 2018.

[40] W. Zhao, J. Zheng, L. Zou, H. Jia, B. Liu, H. Wang, M. H. Engelhard, C. Wang, W. Xu, Y. Yang, and J. G. Zhang, "High Voltage Operation of Ni-Rich NMC Cathodes Enabled by Stable Electrode/Electrolyte Interphases," *Advanced Energy Materials*, vol. 8, no. 19, 2018.

[41] J. Zheng, P. Yan, J. Zhang, M. H. Engelhard, Z. Zhu, B. J. Polzin, S. Trask, J. Xiao, C. Wang, and J. Zhang, "Suppressed oxygen extraction and degradation of LiNixMnyCozO2 cathodes at high charge cut-off voltages," *Nano Research*, vol. 10, no. 12, 2017.

[42] L. Madec, L. Ma, K. J. Nelson, R. Petibon, J.-P. Sun, I. G. Hill, and J. R. Dahn, "The Effects of a Ternary Electrolyte Additive System on the Electrode/Electrolyte Interfaces in High Voltage Li-Ion Cells," *Journal of The Electrochemical Society*, vol. 163, no. 6, 2016.

[43] L. Madec, J. Xia, R. Petibon, K. J. Nelson, J. P. Sun, I. G. Hill, and J. R. Dahn, "Effect of sulfate electrolyte additives on LiNi1/3Mn1/3Co1/3O2/graphite pouch cell lifetime: Correlation between xps surface studies and electrochemical test results," *Journal of Physical Chemistry C*, vol. 118, no. 51, 2014.

[44] P. Niehoff and M. Winter, "Composition and growth behavior of the surface and electrolyte decomposition layer of/on a commercial lithium ion battery LixNi 1/3Mn1/3Co1/3O2 cathode determined by sputter depth profile X-ray photoelectron spectroscopy," *Langmuir*, vol. 29, no. 51, 2013.

[45] M. Mirolo, C. A. Vaz, P. Novák, and M. El Kazzi, "Multi-length-scale x-ray spectroscopies for determination of surface reactivity at high voltages of LiNi0.8Co0.15Al0.05O2vs Li4Ti5O12," *Journal of Chemical Physics*, vol. 152, no. 18, 2020.

[46] W. S. Yoon, O. Haas, S. Muhammad, H. Kim, W. Lee, D. Kim, D. A. Fischer, C. Jaye, X. Q. Yang, M. Balasubramanian, and K. W. Nam, "In situ soft XAS study on nickel-based layered cathode material at elevated temperatures: A novel approach to study thermal stability," *Scientific Reports*, vol. 4, 2014.

[47] R. Qiao, Y. D. Chuang, S. Yan, and W. Yang, "Soft X-Ray Irradiation Effects of Li2O2, Li2CO3 and Li2O Revealed by Absorption Spectroscopy," *PLoS ONE*, vol. 7, no. 11, 2012.

[48] E. De Clermont Gallerande, D. Cabaret, G. Lelong, C. Brouder, M. B. Attaiaa, L. Paulatto, K. Gilmore, C. J. Sahle, and G. Radtke, "First-principles modeling of x-ray Raman scattering spectra," *Physical Review B*, vol. 98, no. 21, 2018.

[49] N. Mahne, S. E. Renfrew, B. D. McCloskey, and S. A. Freunberger, "Electrochemical Oxidation of Lithium Carbonate Generates Singlet Oxygen," *Angewandte Chemie - International Edition*, vol. 57, no. 19, 2018.

[50] L. Calmels, P. E. Coulon, and S. Schamm-Chardon, "Calculated and experimental electron energy-loss spectra of La2 O3, la (OH)3, and LaOF nanophases in high permittivity lanthanum-based oxide layers," *Applied Physics Letters*, vol. 98, no. 24, 2011.

[51] K. Zhou, S. Zheng, F. Ren, J. Wu, H. Liu, M. Luo, X. Liu, Y. Xiang, C. Zhang, W. Yang, L. He, and Y. Yang, "Fluorination effect for stabilizing cationic and anionic redox activities in cation-disordered cathode materials," *Energy Storage Materials*, vol. 32, 2020.

[52] V. Drozd, G. Q. Liu, R. S. Liu, H. T. Kuo, C. H. Shen, D. S. Shy, and X. K. Xing, "Synthesis, electrochemical properties, and characterization of LiFePO4/C composite by a two-source method," *Journal of Alloys and Compounds*, vol. 487, no. 1-2, 2009.

[53] V. R. Galakhov, V. V. Mesilov, S. N. Shamin, N. V. Urusova, Y. A. Barykina, and D. G. Kellerman, "Magnetic and soft X-ray absorption spectroscopy characterization of Mn and Co doped lithium nickel phosphate LiNiPO4," *Physica Status Solidi (B) Basic Research*, vol. 254, no. 4, 2017.

[54] D. Chen, J. Ahn, E. Self, J. Nanda, and G. Chen, "Understanding cation-disordered rocksalt oxyfluoride cathodes," *Journal of Materials Chemistry A*, vol. 9, no. 12, 2021.

[55] Y. Yue, Y. Ha, R. Giovine, R. Clément, W. Yang, and W. Tong, "High-Voltage Reactivity and Long-Term Stability of Cation-Disordered Rocksalt Cathodes," *Chemistry of Materials*, vol. 34, no. 4, 2022.

[56] G. Cherkashinin, M. Motzko, N. Schulz, T. Späth, and W. Jaegermann, "Electron spectroscopy study of Li[Ni,Co,Mn]O2/electrolyte interface: Electronic structure, interface composition, and device implications," *Chemistry of Materials*, vol. 27, no. 8, 2015.

[57] H. Huang, Y. C. Chang, Y. C. Huang, L. Li, A. C. Komarek, L. H. Tjeng, Y. Orikasa, C. W. Pao, T. S. Chan, J. M. Chen, S. C. Haw, J. Zhou, Y. Wang, H. J. Lin, C. T. Chen, C. L. Dong, C. Y. Kuo, J. Q. Wang, Z. Hu, and L. Zhang, "Unusual double ligand holes as catalytic active sites in LiNiO2," *Nature Communications*, vol. 14, no. 1, 2023.

[58] I. N. Demchenko, K. Lawniczak-Jablonska, T. Tyliszczak, N. R. Birkner, W. C. Stolte, M. Chernyshova, and O. Hemmers, "XANES studies of modified and newly synthesized nanostructured manganese oxides," *Journal of Electron Spectroscopy and Related Phenomena*, vol. 171, no. 1-3, 2009.

[59] B. Gilbert, B. H. Frazer, A. Belz, P. G. Conrad, K. H. Nealson, D. Haskel, J. C. Lang, G. Srajer, and G. De Stasio, "Multiple scattering calculations of bonding and X-ray absorption spectroscopy of manganese oxides," *Journal of Physical Chemistry A*, vol. 107, no. 16, 2003.

[60] C. F. J. Flipse, C. B. Rouwelaar, and F. M. F. De Groot, "Magnetic properties of CoO nanoparticles," *The European Physical Journal D-Atomic, Molecular, Optical and Plasma Physics*, vol. 9, pp. 479–481, 1999.

[61] H. Liu, J. Guo, Y. Yin, A. Augustsson, C. Dong, J. Nordgren, C. Chang, P. Alivisatos, G. Thornton, D. F. Ogletree, F. G. Requejo, F. De Groot, and M. Salmeron, "Electronic structure of cobalt nanocrystals suspended in liquid," *Nano Letters*, vol. 7, no. 7, 2007.

[62] A. M. Hibberd, H. Q. Doan, E. N. Glass, F. M. De Groot, C. L. Hill, and T. Cuk, "Co polyoxometalates and a Co3O4 thin film investigated by L-edge X-ray absorption spectroscopy," *Journal of Physical Chemistry C*, vol. 119, no. 8, 2015.

[63] M. Welke, J. Gräfe, R. K. Govind, V. H. Babu, M. Trautmann, K. M. Schindler, and R. Denecke, "XMCD studies of thin Co films on BaTiO3," *Journal of Physics Condensed Matter*, vol. 27, no. 32, 2015.

[64] P. Müller, M. Meffert, H. Störmer, and D. Gerthsen, "Fast mapping of the cobalt-valence state in Ba0.5Sr 0.5Co0.8Fe0.2O3-d by electron energy loss spectroscopy," *Microscopy and Microanalysis*, vol. 19, no. 6, 2013.

[65] B. L. D. Rinkel, J. P. Vivek, N. Garcia-Araez, and C. P. Grey, "Two electrolyte decomposition pathways at nickel-rich cathode surfaces in lithium-ion batteries," *Energy & Environmental Science*, vol. 15, no. 8, pp. 3416–3438, 2022.

[66] I. G. Shenderovich, P. M. Tolstoy, N. S. Golubev, S. N. Smirnov, G. S. Denisov, and H. H. Limbach, "Low-temperature NMR studies of the structure and dynamics of a novel series of acid-base complexes of HF with collidine exhibiting scalar couplings

across hydrogen bonds," in *Journal of the American Chemical Society*, vol. 125, 2003.

[67] N. M. Al-Mansi and N. M. Abdel Monem, "Recovery of nickel oxide from spent catalyst," *Waste Management*, vol. 22, no. 1, 2002.

[68] Y. C. Chung and B. J. Wuensch, "Growth of nickel oxide single crystals and bicrystals via chemical vapor transport," *Journal of the American Ceramic Society*, vol. 79, no. 3, 1996.

[69] H. Haghkhah, B. Ghalami Choobar, and S. Amjad-Iranagh, "Effect of salt concentration on properties of mixed carbonate-based electrolyte for Li-ion batteries: a molecular dynamics simulation study," *Journal of Molecular Modeling*, vol. 26, no. 8, 2020.

[70] M. Mynam, B. Ravikumar, and B. Rai, "Molecular dynamics study of propylene carbonate based concentrated electrolyte solutions for lithium ion batteries," *Journal of Molecular Liquids*, vol. 278, 2019.

[71] M. Shakourian-Fard, G. Kamath, and S. K. Sankaranarayanan, "Evaluating the Free Energies of Solvation and Electronic Structures of Lithium-Ion Battery Electrolytes," *ChemPhysChem*, 2016.

[72] R. Tatara, Y. Yu, P. Karayaylali, A. K. Chan, Y. Zhang, R. Jung, F. Maglia, L. Giordano, and Y. Shao-Horn, "Enhanced Cycling Performance of Ni-Rich Positive Electrodes (NMC) in Li-Ion Batteries by Reducing Electrolyte Free-Solvent Activity," *ACS Applied Materials and Interfaces*, vol. 11, no. 38, 2019.

[73] K. Yoshida, M. Nakamura, Y. Kazue, N. Tachikawa, S. Tsuzuki, S. Seki, K. Dokko, and M. Watanabe, "Oxidative-stability enhancement and charge transport mechanism in glyme-lithium salt equimolar complexes," *Journal of the American Chemical Society*, vol. 133, no. 33, 2011.

[74] A. Heckmann, J. Thienenkamp, K. Beltrop, M. Winter, G. Brunklaus, and T. Placke, "Towards high-performance dual-graphite batteries using highly concentrated organic electrolytes," *Electrochimica Acta*, vol. 260, 2018.

[75] S. Solchenbach, M. Metzger, M. Egawa, H. Beyer, and H. A. Gasteiger, "Quantification of PF ₅ and POF ₃ from Side Reactions of LiPF ₆ in Li-Ion Batteries," *Journal of The Electrochemical Society*, vol. 165, pp. A3022–A3028, 9 2018.

[76] S. E. Sloop, J. K. Pugh, S. Wang, J. B. Kerr, and K. Kinoshita, "Chemical Reactivity of PF[sub 5] and LiPF[sub 6] in Ethylene Carbonate/Dimethyl Carbonate Solutions," *Electrochemical and Solid-State Letters*, vol. 4, no. 4, p. A42, 2001.

[77] C. L. Campion, W. Li, and B. L. Lucht, "Thermal Decomposition of LiPF[sub 6]-Based Electrolytes for Lithium-Ion Batteries," *Journal of The Electrochemical Society*, vol. 152, no. 12, p. A2327, 2005.

[78] W. Lange, R. Livingston, and R. Livingston, "Studies of Fluorophosphoric Acids and their Derivatives. XIV. Preparation of Anhydrous Difluorophosphoric Acid," *Journal of the American Chemical Society*, vol. 72, no. 3, 1950.

Chapter 4

Applying the MS diffusion framework to LIB electrolytes

4.1 Abstract

LIBs play a crucial role in the energy transition from fossil fuels towards intermittent, renewable energy sources. The DFN model is widely applied for the simulation of LIBs and derives equations from MS diffusion. Electrolytes used in most commercial LIBs are based on $LiPF_6$ salt dissolved in a mixture of cyclic and linear organic carbonates. Recent studies have demonstrated that salt and solvent concentrations vary across a LIB under an applied current. Given that interfacial reactions can be altered significantly by the surface concentrations of electrolyte species, accurate simulation is crucial to understanding battery performance and degradation. Here we develop a methodology to apply the MS diffusion model to multicomponent LIB electrolytes, simulating the concentrations of each electrolyte species separately. We employ confocal Raman microscpectroscopy to experimentally measure the concentration gradients of each electrolyte species. We parameterize the MS diffusion model directly from MD simulations. This work has provided fundamental insight into the simulation of multicomponent LIB electrolytes on the continuum scale. This work will enable the surface concentrations of all electrolyte species to be simulated in the DFN model, paving the way for more accurate descriptions of the complex electrochemical processes occurring at the electrode-electrolyte interface. This work provides fundamental insight into the simulation of LIB electrolytes on the continuum scale which will aid the development and optimization of LIB electrolytes for use with high voltage cathode materials.

4.2 Introduction

LIBs are the dominant technology in portable electronic devices[1] and increasingly used as power sources for electric vehicles,[2,3] and even grid-scale energy storage.[4] LIBs can be charged using intermittent renewable energy sources giving them a key role in the decarbonization of energy storage and electrification of vehicles. Electrolyte solvation structure and composition near electrode surfaces can alter the interfacial reactions that proceed, influencing the lifetime and long term cycling performance of LIBs.[5] A more complete understanding of battery degradation therefore requires accurate simulation of the local concentrations of each electrolyte species.[6–8] Parameterisation of the electrolyte phase within the DFN model has been informed in recent years by fitting to experimentally measured concentration profiles of electrolyte species under applied currents, which can be obtained with techniques such as Raman spectroscopy,[9–12] magnetic resonance imaging (MRI)[13–16] and optical imaging.[17] Commercial LIB electrolytes typically consist of lithium salts such as $LiPF_6$ in a mixture of non-aqueous solvents. These solvents are commonly composed of cyclic alkyl carbonates, most typically EC, but also fluoroethylene carbonate (FEC) and PC, combined with linear alkyl carbonates such DMC, EMC and diethyl carbonate (DEC). The single-solvent assumption has been proposed in an attempt to parameterise these electrolytes within the DFN model.[18–20] This assumption postulates that cosolvents collectively behave as a single entity with all constituents travelling with identical velocities. This approximation is implemented due to experimental limitations rather than conclusive experimental evidence, and its validity has recently been called into question.[21] Attempts to account for cosolvents have often had to assume they are dilute to enable their incorporation into the governing equations.[22–24] More recently, efforts have been made to incorporate additional cosolvent terms accounting explicitly for EC, in 1 M $LiPF_6$ in EC:EMC based electrolytes by building on the theoretical framework proposed by Monroe.[25,26] However, a the general MS diffusion framework capable of describing an n-component LIB electrolyte alongside a tractable approach to obtain the parameters required for simulation has yet to be presented and tested against experimetally measured concentration gradients. Recent studies of Ni rich NMC cathode materials have revealed the dependence of parasitic side reactions occurring at the NMC interfaces especially at high potentials on the nature of the electrolyte solvent[6,7] and salt[8] concentrations. In order to accurately model such side reactions, the surface concentrations of the electrolyte species on the electrodes must be considered. This requires the ability to more easily parameterize multicomponent electrolyte continuum models that provide separate concentrations of each electrolyte species.

With this in mind, herein we introduce a methodology to parameterize LIB electrolytes within the MS diffusion framework using MD. The calculated parameters are then com-

pared to experimentally measured concentration profiles. Using Raman-based concentration profiles,[9–12] and parameters obtained from MD calculations, we successfully simulate 1 M $LiPF_6$ in EC:EMC vol:vol 3:7, a widely-used LIB electrolyte composition. The ability to easily extract these parameters will enable the accurate application of kinetic expressions for the complex electrochemical processes occurring at the electrode-electrolyte interface. This work provides fundamental insight into the simulation of LIB electrolytes on the continuum scale which will aid the development of improved electrolytes and increase understanding solid-electrolyte interphase compositions via electrolyte decomposition for commercial LIBs.

4.3 Experimental Methods

4.3.1 Electrolyte Preparation

EC (99+%, Acros Organics) and EMC (99.95+%, Solvionic) were mixed in a volume:volume ratio of 3:7 and dried for 24 hours using dried molecular sieves (3 Å, beads, 8-12 mesh , Sigma Aldrich). The EC:EMC mixture water content before mixing was measured using Karl Fischer titration and was found to be 3.3 ppm. $LiPF_6$ (98+ %, Fisher Scientific) was dried under dynamic vacuum at 1-2 mbar at 30 ^{o}C for 24 hours. Electrolytes were mixed to various molarities (0.5 - 2 M).

4.3.2 Raman Spectroscopy

The optical cell is composed of two stainless steel (grade 316) plungers, a ⌀6 mm quartz tube and two Viton O-rings. ⌀6 mm Li metal disks were attached to each plunger in a glovebox. The first plunger was inserted into the quartz tube, the internal volume of the tube was filled with electrolyte then sealed by inserting the second plunger (see Figure 4.10d). Care was taken to ensure no gas bubbles were trapped in the tube upon sealing the cell. The cell was stood vertically in the Raman microscope on a movable stage and a constant current of 0.25 mA cm^{-2} was applied using a Biologic SP-300 potentiostat. Line scans were performed by moving the stage vertically during operation and recording spectra at different points along the optical cell under the applied current.

A Renishaw inVia Reflex laser confocal Raman microscope using a 785nm near-IR Laser, a 5× magnification objective (Leica, 0.12 NA, 14 mm WD), a 1200 gr/mm grating and a 90^o mirror yielding a spot size of ∼4 μm was used to acquire the Raman spectra. Spectra were recorded with 5% laser power (15 mW) with a 1 s exposure time and were repeated 30 times at each point. Spectra were recorded at 51 different points in the sample along the optical cell. A linear background was subtracted and normalisation against the area under

the $-CH_2$ bending modes for EMC and EC at 1440 cm^{-1} and 1480 cm^{-1} respectively. The integrated areas of peaks were extracted by fitting Voigt functions to each peak, and then numerically integrating under the fitted peak.

To extract the concentration gradients, the areas of the PF_6^- stretching band (741 cm^{-1}) and EC skeletal breathing band (891 cm^{-1}) were found to vary linearly with mole fraction in the range of interest. A linear calibration curve was constructed from the following concentrations: 0.0 , 0.5 , 1.1 and 2.0 m, which was used to convert integrated areas to mole fractions, which were then converted to molarities. Measurements were conducted with different inter electrode spacings (6mm, 7.3mm, 13.3mm) to investigate the accuracy of calculated model parameters.

4.3.3 Molecular Dynamics

MD simulations were performed using the Large Scale Atomic/ Molecular Massively Parallel Simulator (LAMMPS).[27] The non-polarizable optimized potential for liquid simulations all-atom (OPLSAA) forcefield was used to describe atomic interactions in the organic electrolytes.[28] Arithmetic mixing rules were used i.e. $\varepsilon_{ij} = \sqrt{\varepsilon_{ii}\varepsilon_{jj}}$, $\sigma_{ij} = \frac{\sigma_{ii}+\sigma_{jj}}{2}$. The bonded interactions were modelled as harmonic functions.[29] The non-bonded and bonded parameters for EC and EMC were obtained from the OPLSAA forcefield[28,30] and have recently been used in similar systems.[29] Restrained Electrostatic Potential (RESP) fitted atomic charges for EC and EMC were taken from Hou et al.[29] The LJ parameters for the Li^+ ions were taken from Jensen et al.[31] The parameters for the PF_6^- anions are from Kumar and Seminario,[32] and Jorn et al.[33] For $LiPF_6$ electrolytes the cation charge was set to +1 and the anion charge was set to -1.

1 m $LiPF_6$ in EC:EMC vol:vol 3:7 was simulated. The system consisted of 432 EMC molecules and 277 EC molecules and 71 $LiPF_6$ salt ion pairs. Topologies of individual molecules were generated using the Avogadro software.[34] Initial configurations of the electrolyte system were generated using the Packing Optimization for Molecular Dynamics Simulations (PACKMOL) software.[35] Forcefield parameters were assigned to each atom using Moltemplate.[36] Periodic boundary conditions are applied in a cubic simulation box to represent the electrolyte bulk solution. The simulations were performed on an in-house machine utilising GPU acceleration from a Geforce GTX 1660 graphics card.[37–42] A Nose-Hoover thermostat and barostat are applied to maintain the desired temperatures and pressures. A timestep of 1 fs is used. The system is equilibrated in the isothermal–isobaric ensemble (constant NPT conditions) at 303.15 K for 2 ns, heated to 400 K over 1 ns, held there for 1 ns then cooled down to 303.15 K over 1 ns. The system is equilibrated for a further 1 ns at 303.15 K. Cell volumes and densities were then recorded for 5 ns and the equilibrium values at 303.15 K are extracted. A new

cell was constrained to the equilibrium density in the canonical ensemble (constant NVT conditions) and equilibrated in the same way. Atomistic velocities were recorded every 1 fs for 10 ns at 303.15 K. The activity factors for EC and EMC were calculated using the Osmotic Pressure Activity of Solvent (OPAS) method.[43] A periodic cell composed of two adjacent chambers was constructed. The first chamber contained the electrolyte of interest constrained to its equilibrated density under constant NVT conditions. The second chamber contained 500 molecules of either EC or EMC constrained to their MD equilibrated density for the neat solvent ($\rho_{\text{EC, MD}}$ =1.298 g cm^{-3}, $\rho_{\text{EMC,MD}}$ =1.026 g cm^{-3}). A semi permeable membrane was implemented in LAMMPS using the *fix oneway* command to prevent Li^+, PF_6^- and the other solvent species from crossing into the neat solvent chamber. The solvent molecule of interest could move freely between both chambers. The system was equilibrated in the same way as above. The average pressure of each chamber over a 20 ns production run and the osmotic pressure difference is recorded. The osmotic pressure difference was ccalculated for different electrolyte salt concentrations by varying the number of $LiPF_6$ salt ion pairs from 35 to 278. The same procedure as described above was used to simulate the electrolytes at the different salt concentrations.

4.4 MS Diffusion Framework

In Maxwell-Stefan diffusion, a local equilibrium is assumed between the driving forces such as chemical and electrostatic potential gradients, and the frictional forces arising from molecular interactions.[44] If electroneutrality is assumed:

$$\sum_{j=1}^{n} \frac{x_i N_j - x_j N_i}{c_t Đ_{ij}} = \sum_{j=1}^{n-1} \Gamma_{ij} \nabla x_j + \frac{F}{RT} z_i x_i \nabla \phi \quad i = 1,2,...n-1 \tag{4.1}$$

$$\sum_{i=1}^{n} z_i x_i = 0 \tag{4.2}$$

x_i is the mole fraction of species i, c_t is the total molar concentration of the mixture, R is the universal gas constant, T is temperature, F is Faraday's constant, z_i is the charge of species i, $Đ_{ij}$ are the MS pair diffusivities, N_i is the molar flux density in mol m^{-2} s^{-1} of species i, and ϕ is the electrostatic potential in the electrolyte. Γ_{ij} is the thermodynamic activity factor defined as $\Gamma_{ij} = \delta_{ij} + x_i \frac{\partial ln \gamma_i}{\partial x_j}\Big|_{T,P,\Sigma}$ where γ_i is the activity of species i, and δ_{ij} is the Kronecker delta function.[44] For a n-component electrolyte, we can write $n-1$ generalized driving force balance equations. The final driving force balance is replaced by asserting that the sum of all mole fractions must be 1, and that n mass balances

apply:

$$\sum_{i=1}^{n} x_i = 1 \tag{4.3}$$

$$\frac{\partial c_i}{\partial t} = -\nabla \cdot N_i + R_i \quad i = 1,2,...n \tag{4.4}$$

where R_i is the rate of generation of species i. At each interface we assert that the flux of species i is equal to the rate of production of species i at that interface.

$$N_i = R_i \tag{4.5}$$

The term on the left of equation 4.1 represents the sum of the dynamic frictional forces ($f_{i,fric}$) opposing the motion of species i past all other species j. Examples of the origins of such friction are molecular collisions or intermolecular interactions. The terms on the right of equation 4.1 are the driving forces which arise from the chemical ($f_{i,\mu}$) and electrostatic ($f_{i,\phi}$) potential gradients . Equation 4.1 may thus be expressed as

$$f_{i,fric} = c_t RT \sum_{j=1}^{n} \frac{x_i N_j - x_j N_i}{c_t Đ_{ij}} \tag{4.6}$$

$$f_{i,\mu} = -c_t RT \sum_{j=1}^{n-1} \Gamma_{ij} \nabla x_j \tag{4.7}$$

$$f_{i,\phi} = -c_t RT \frac{z_i x_i F}{RT} \nabla \phi \tag{4.8}$$

$$f_{i,fric} + f_{i,\mu} + f_{i,\phi} = 0 \quad i = \mathrm{Li}^+, \mathrm{PF}_6^-, \mathrm{EC}, \mathrm{EMC} \tag{4.9}$$

A positive value of f indicates the force is acting from the anode towards the cathode, with the direction reversed for a negative value. $f_{i,fric}$ always acts in the opposite direction to the net driving force resulting from $f_{i,\phi}$ and $f_{i,\mu}$.

4.5 Governing Equations for Raman Cell

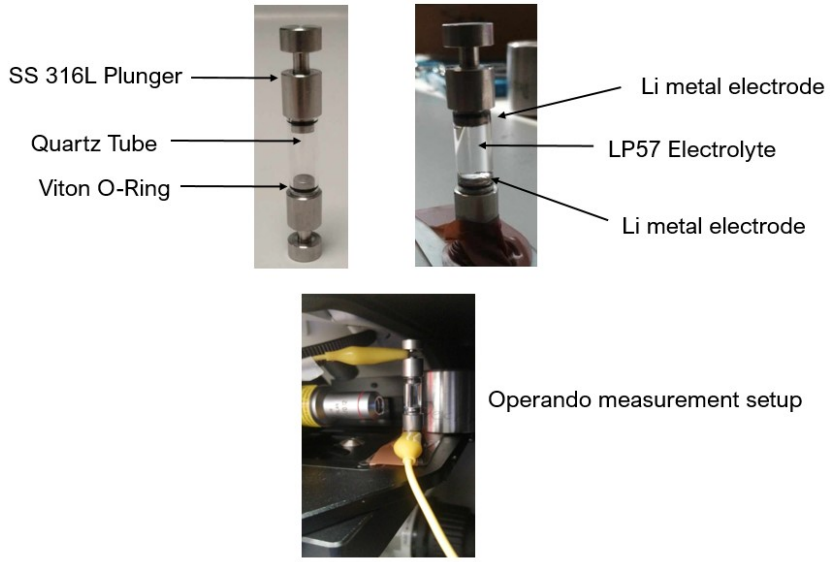

Figure 4.1: Optical cell used for operando Raman measurements.

The Raman cell is setup as shown in Figure (4.1). In the case of 1 M $LiPF_6$ in EC:EMC vol:vol 3:7 electrolyte, we have 4 components: Li^+, PF_6^-, EC and EMC. At each interface, the applied current $I = N_{Li^+}AF$, where A is the surface area of the electrode, F is Faradays constant i.e. $R_{Li^+} = \frac{I}{AF}$. For all other species, N_i=0 at the interface. In the bulk electrolyte, R_i=0 for all species. Applying these conditions to the model developed in this section yields a set of nonlinear simultaneous equations listed in table 4.1. The temperature was set to 30 ^{o}C. c_t was detemined to be 12.98 M. The density of the electrolyte was measured to be 1.225 g cm^{-3}. The initial mole fractions of Li^+ and PF_6^- were set to 0.077. The initial mole fractions of EC and EMC were set to 0.338 and 0.508 respectively.

Li Metal (x = 0)	Electrolyte (0 < x < L)	Li Metal (x = L)
$N_1 = \frac{-I}{AF}$	$\frac{\partial c_1}{\partial t} = -\nabla \cdot N_1$	$N_1 = \frac{-I}{AF}$
$N_2 = 0$	$\frac{\partial c_2}{\partial t} = -\nabla \cdot N_2$	$\phi = \phi_0$
$N_3 = 0$	$\frac{\partial c_3}{\partial t} = -\nabla \cdot N_3$	$N_3 = 0$
$N_4 = 0$	$\frac{\partial c_4}{\partial t} = -\nabla \cdot N_4$	$N_4 = 0$
$\sum_{j=1}^{n=4} \frac{x_i N_j - x_j N_i}{c_t D_{ij}} = \sum_{j=1}^{3} \Gamma_{ij} \nabla x_j + \frac{x_i z_i F}{RT} \nabla \phi \qquad i = 1$		
$\sum_{j=1}^{n=4} \frac{x_i N_j - x_j N_i}{c_t D_{ij}} = \sum_{j=1}^{3} \Gamma_{ij} \nabla x_j + \frac{x_i z_i F}{RT} \nabla \phi \qquad i = 2$		
$\sum_{j=1}^{n=4} \frac{x_i N_j - x_j N_i}{c_t D_{ij}} = \sum_{j=1}^{3} \Gamma_{ij} \nabla x_j + \frac{x_i z_i F}{RT} \nabla \phi \qquad i = 3$		
$, \sum_{i=1}^{n=4} x_i = 1$		
$\sum_{i=1}^{n=4} x_i z_i = 0$		

Table 4.1: Boundary conditions and governing equations used to apply the MS diffusion to the LIB electrolyte. Indices 1, 2, 3 and 4 correspond to Li^+, PF_6^-, EC and EMC respectively.

4.6 MS diffusivity calculation

MS diffusivities, $Đ_{ij}$, were calculated using the velocity autocorrelation function (VACF) method from atomistic velocities in the MD simulation. The Onsager transport coefficients Λ_{ij} may be determined directly from the motion of molecules[45,46]

$$\Lambda_{ij} = \frac{1}{3N}\int_0^\infty dt \langle \sum_{l=1}^{N_l} v_{l,i}(0) \cdot \sum_{k=1}^{N_k} v_{k,j}(t) \rangle \tag{4.10}$$

In equation (4.10), N is the total number of molecules in the simulation, N_l is the number of molecules of species i, and $v_{l,i}(t)$ is the velocity of l^{th} molecule of species i at time t.

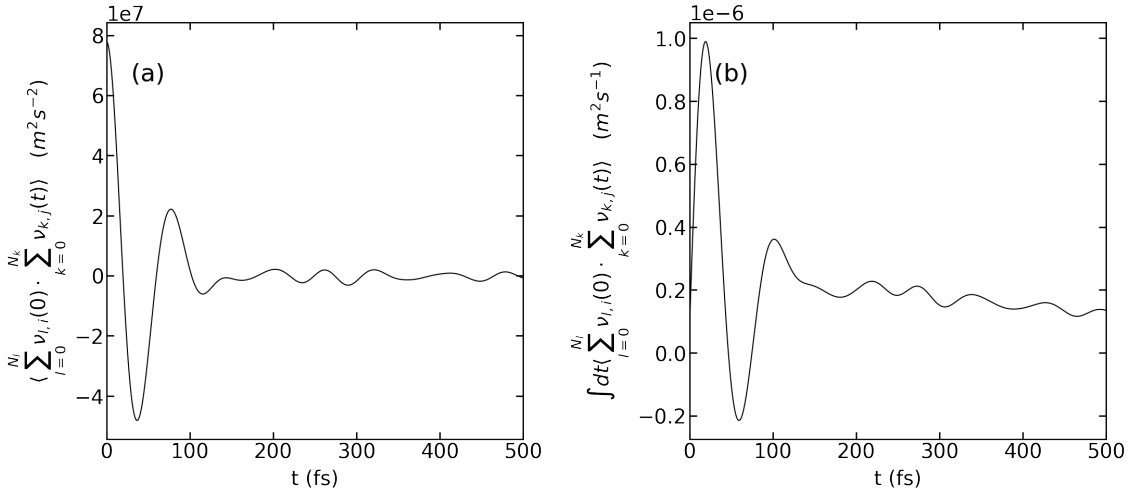

Figure 4.2: (a) VACF and (b) running integral of the VACF for $i = Li^+$ and $j = Li^+$ calculated using velocities recorded every 1 fs for 10 ns. For long time lags the running integral of the VACF converges to a constant value. The average value of the running integral was taken for t between 50,000 fs and 1,000,0000 fs. and then used to calculate Λ_{ij} in equation 4.10

Let n be the number of different species in the MD simulation. We define a $(n-1)$ dimensional matrix [Δ] is then defined such that[45,46]

$$\Delta_{ij} = (1-x_i)(\frac{\Lambda_{ij}}{x_j} - \frac{\Lambda_{in}}{x_n}) - x_i \sum_{k=1;k\neq i}^{k=n} (\frac{\Lambda_{kj}}{x_j} - \frac{\Lambda_{kn}}{x_n}) \quad (i,j = 1,2,3,...,n-1) \tag{4.11}$$

In the above equation x_i is the mole fraction of species i. The matrix $[B]$ is defined as[45,46]

$$[\Delta] = [B]^{-1} \tag{4.12}$$

The $Đ_{ij}$ values may be calculated from the B matrix and mole fractions from the following relationships, where n is the total number of species in the mixture:

$$Đ_{in} = \frac{1}{B_{ii} + \sum_{k=1,k\neq i}^{n-1} \frac{x_k}{x_i} B_{ik}} \tag{4.13}$$

$$Đ_{ij} = \frac{1}{\frac{1}{Đ_{in}} - \frac{B_{ij}}{x_i}} \tag{4.14}$$

The $Đ_{ij}$ values calculatd in this thesis are listed in table 4.4.

Table 4.2: MS diffusivity values calculated using equations 4.13 and 4.14

Diffusivity	Value
$Đ_{Li^+,PF_6^-}$	0.940
$Đ_{Li^+,EC}$	2.378
$Đ_{Li^+,EMC}$	2.069
$Đ_{PF_6^-,EC}$	0.362
$Đ_{PF_6^-,EMC}$	0.577
$Đ_{EC,EMC}$	2.340
Units	$1\times10^{-10}\ m^2s^{-1}$

4.7 Γ_{ij} Calculation

The osmotic pressure difference between the electrolyte and pure solvent chambers calculated using the OPAS method, Π, may be related directly to the activity of the solvent in the electrolyte, a_i.[43,47]

$$\log(a_i) = -\frac{\Pi}{c_i k_B T} \quad i = \text{EC, EMC} \tag{4.15}$$

c_i is the molar concentration of the solvent in the chamber containing only solvent molecules. T is the temperature in Kelvin. k_B is Boltzmann's constant. The activities of EC and EMC were calculated for various salt concentrations. The activity factor, γ_i is defined as

$$\gamma_i = \frac{a_i}{x_i} \tag{4.16}$$

x_i is the mole fraction of species i. γ_{EC} and γ_{EMC} were fitted as a function of the number of Li^+ ions in the electrolyte according to:

$$\gamma_i = \frac{AN_{Li^+}}{1 + BN_{Li^+} + CN_{Li^+}^2 + DN_{Li^+}^3} \quad i = \text{EC, EMC} \tag{4.17}$$

By assuming constant NPT conditions, the Gibbs-Duhem reads:

$$N_{Li^+} d(\ln a_{Li^+}) + N_{PF_6^-} d(\ln a_{PF_6^-}) + N_{\text{EC}} d(\ln a_{\text{EC}}) + N_{\text{EMC}} d(\ln a_{\text{EMC}}) = 0 \tag{4.18}$$

In the electrolytes investigated here, $N_{Li^+} = N_{PF_6^-}$, so we may write

$$d(\ln a_{Li^+}) + d(\ln a_{PF_6^-}) = -\left(\frac{N_{\text{EC}} d(\ln a_{\text{EC}}) + N_{\text{EMC}} d(\ln a_{\text{EMC}})}{N_{Li^+}}\right) \tag{4.19}$$

Here, we assume $d(\ln a_{Li^+}) = d(\ln a_{PF_6^-})$ giving:

$$d(\ln a_{Li^+}) = d(\ln a_{PF_6^-}) = -\left(\frac{N_{\text{EC}} d(\ln a_{\text{EC}}) + N_{\text{EMC}} d(\ln a_{\text{EMC}})}{2N_{Li^+}}\right) \tag{4.20}$$

Using equations 4.17-4.20, γ_{Li^+} and $\gamma_{PF_6^-}$ were determined for each salt concentration by integrating the right hand side of equation 4.20. The fits of equation 4.17 are shown in Figure 4.3. Next, we propose that $\log(\gamma_i)$ is a function of the mole fractions of Li^+, PF_6^- and EC.

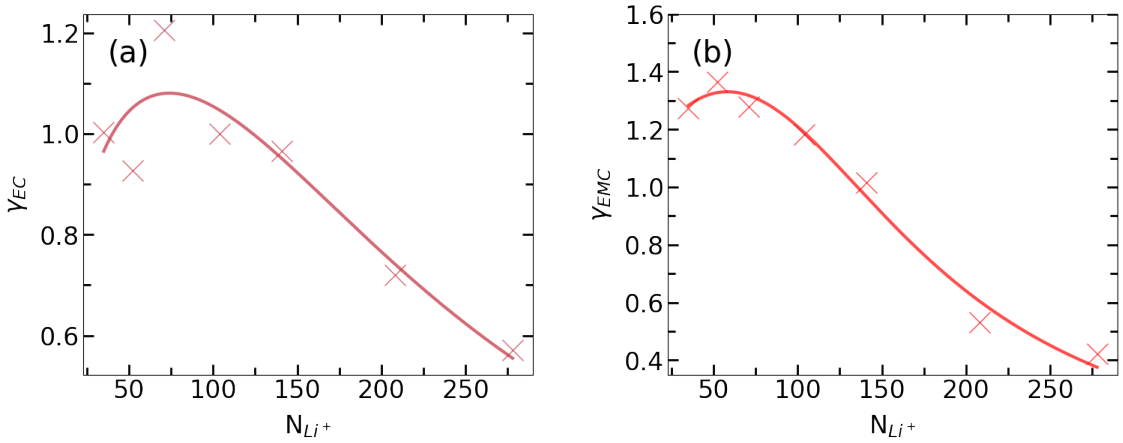

Table 4.3: γ_i as a function of N_{Li^+} for (a) EC and (b) EMC. The crosses are the calculated values using the OPAS method. The continuous lines are the fitted values using equation 4.17.

$$\begin{aligned}\log(\gamma_i) = {} & A_0 + A_1 x_{\mathrm{Li}^+} + A_2 x_{\mathrm{Li}^+}^2 + A_3 x_{\mathrm{PF}_6^-} + A_4 x_{\mathrm{PF}_6^-}^2 \\ & + A_5 x_{\mathrm{EC}} + A_6 x_{\mathrm{EC}}^2 + A_7 x_{\mathrm{Li}^+} x_{\mathrm{PF}_6^-} \\ & + A_8 x_{\mathrm{Li}^+} x_{\mathrm{EC}} + A_9 x_{\mathrm{PF}_6^-} x_{\mathrm{EC}}\end{aligned} \tag{4.21}$$

Since the sum of all mole fractions is 1 we exclude the mole fraction of EMC from the expression. By differentiating equation 4.21 with respect to x_j, Γ_{ij} may be calculated from

$$\Gamma_{ij} = \delta_{ij} + x_i \left(\frac{\partial \log(\gamma_i)}{\partial x_j} \right)_{T,P,\Sigma} \tag{4.22}$$

Table 4.4: Γ_{ij} values calculated for the 1 m $LiPF_6$ in EC:EMC vol:vol 3:7 using the procedure described in this section.

Γ_{ij}	Value
$\Gamma_{\mathrm{Li}^+,\mathrm{Li}^+}$	0.975
$\Gamma_{\mathrm{Li}^+,\mathrm{PF}_6^-}$	-0.025
$\Gamma_{\mathrm{Li}^+,\mathrm{EC}}$	-0.061
$\Gamma_{\mathrm{PF}_6^-,\mathrm{Li}^+}$	-0.025
$\Gamma_{\mathrm{PF}_6^-,\mathrm{PF}_6^-}$	0.975
$\Gamma_{\mathrm{PF}_6^-,\mathrm{EC}}$	-0.061
$\Gamma_{\mathrm{EC},\mathrm{Li}^+}$	-0.237
$\Gamma_{\mathrm{EC},\mathrm{PF}_6^-}$	0.237
$\Gamma_{\mathrm{EC},\mathrm{EC}}$	0.280
Units	-

4.8 Measured and predicted concentration profiles

6 mm Concentration Gradient Validation

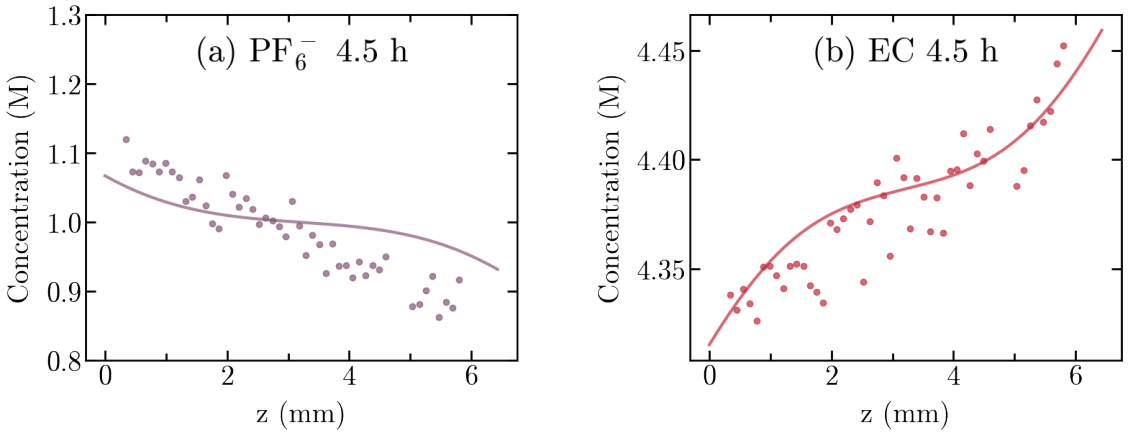

Figure 4.3: Concentration gradients after applying a constant current of 0.25 mA cm^{-2} for 4.5 h in the 6 mm optical cell for (a) PF_6^-, (b) EC.

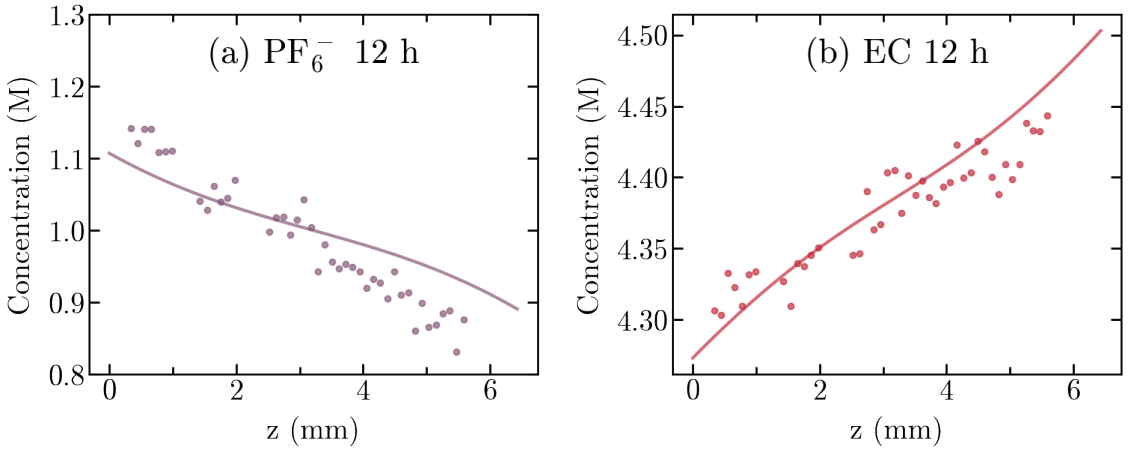

Figure 4.4: Concentration gradients after applying a constant current of 0.25 mA cm^{-2} for 12 h in the 7 mm optical cell for (a) PF_6^-, (b) EC.

7.7 mm Concentration Gradient Validation

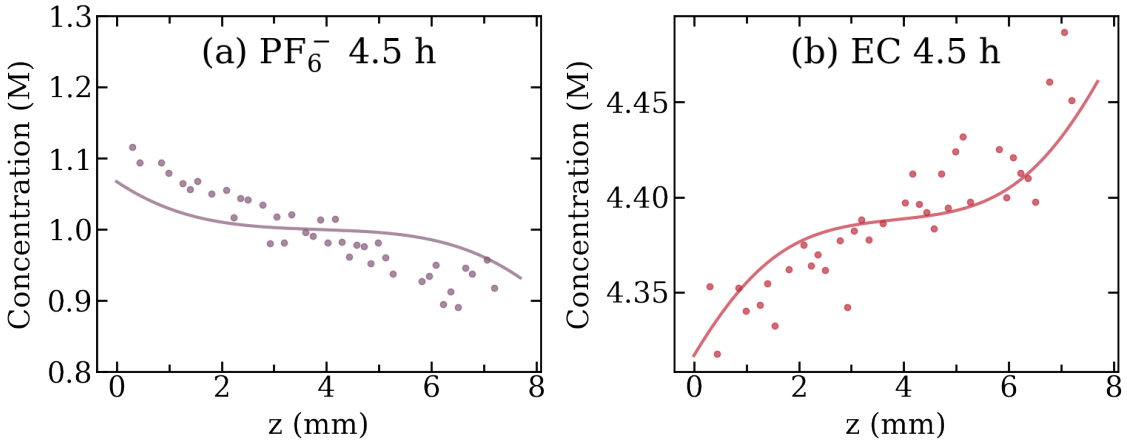

Figure 4.5: Concentration gradients after applying a constant current of 0.25 mA cm^{-2} for 4.5 h in the 7.7 mm optical cell for (a) PF_6^-, (b) EC.

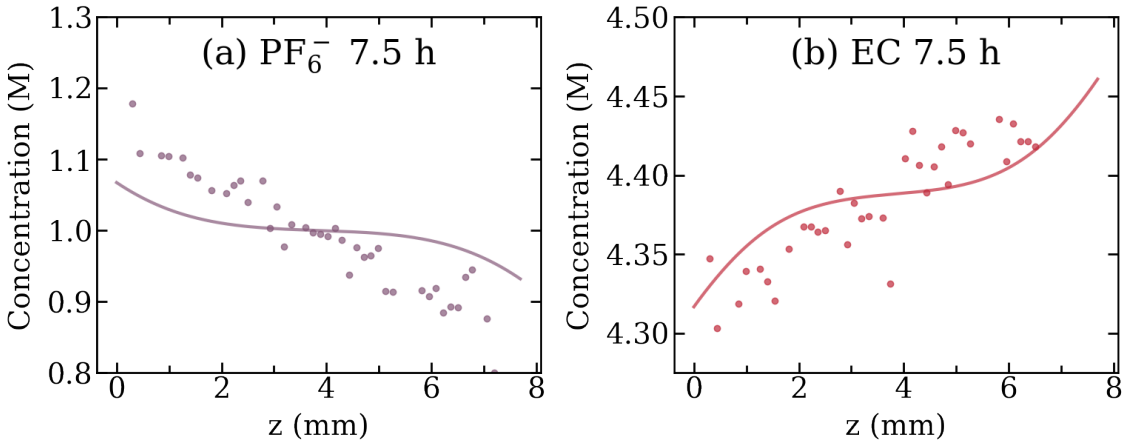

Figure 4.6: Concentration gradients after applying a constant current of 0.25 mA cm^{-2} for 7.5 h in the 7.7 mm optical cell for (a) PF_6^-, (b) EC

13.7 mm Concentration Gradient Validation

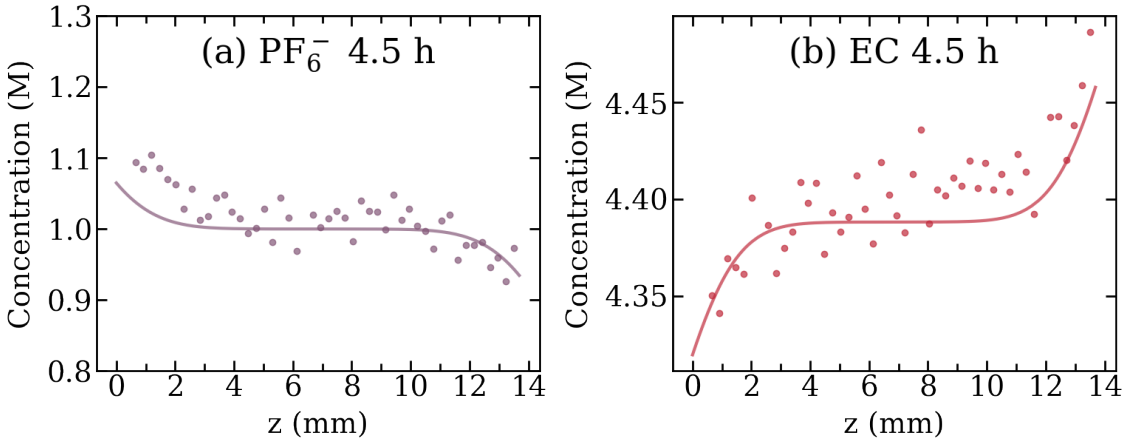

Figure 4.7: Concentration gradients after applying a constant current of 0.25 mA cm^{-2} for 4.5 h in the 13.7 mm optical cell for (a) PF_6^-, (b) EC.

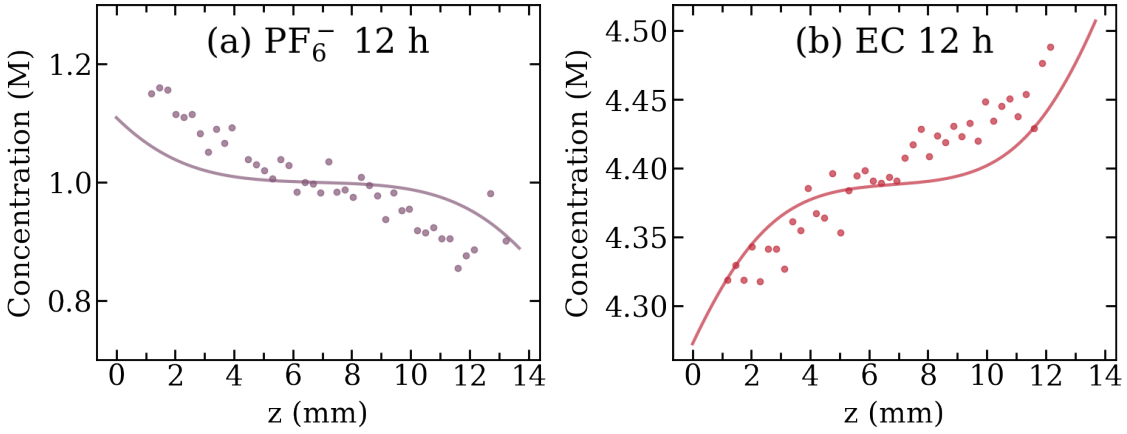

Figure 4.8: Concentration gradients after applying a constant current of 0.25 mA cm^{-2} for 12 h in the 13.7 mm optical cell for (a) PF_6^-, (b) EC.

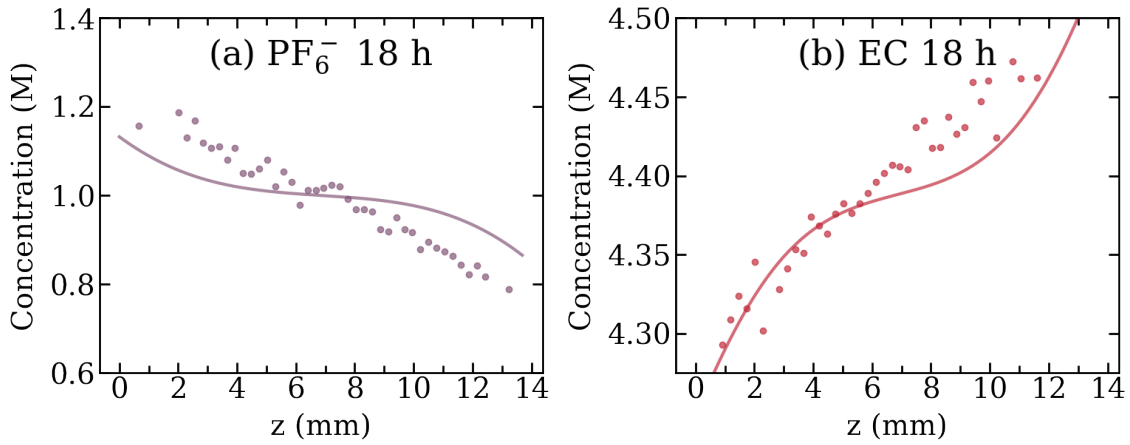

Figure 4.9: Concentration gradients after applying a constant current of 0.25 mA cm^{-2} for 18 h in the 13.7 mm optical cell for (a) PF_6^-, (b) EC.

4.9 Results

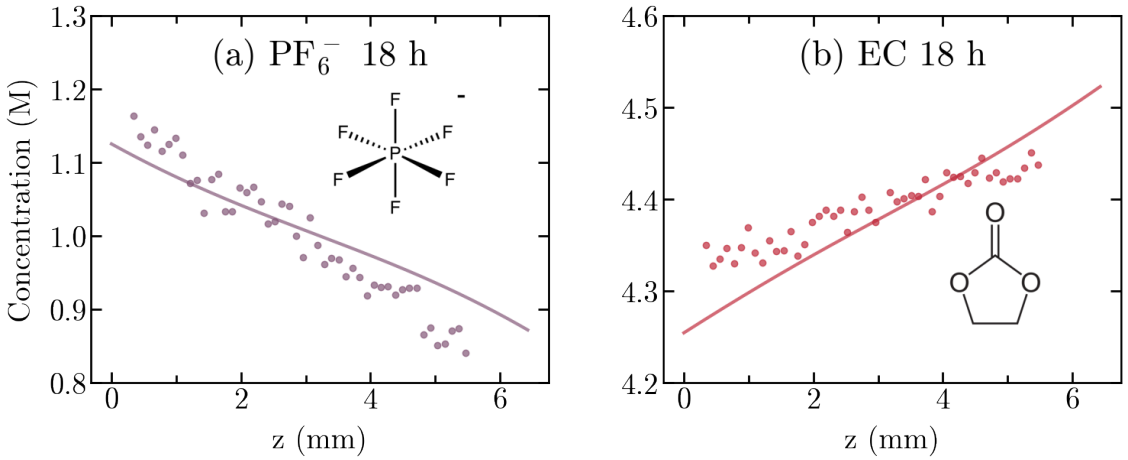

Figure 4.10: Concentration gradients after applying a constant current of 0.25 mA cm^{-2} for 18 h with a 6 mm distance between electrodes for (a) PF_6^-, (b) EC. The experimental data is displayed as points while the modelled concentration profiles are continuous lines.

Figure 4.10 shows the concentration gradients of PF_6^- and EC obtained from the optical cell using Raman spectroscopy measurements, and the modelled gradients using the parameters calculated from MD. Li^+ concentration gradients were taken to be identical to those of the PF_6^-, based on the assumption of local charge neutrality.[48] The modelled profiles show good agreement with the experimentally measured concentration gradients in Figure 4.10, providing support for the methodology employed in this work. Further comparisons between experimental data and model predictions for 6 mm, 7.7 mm and 13.7 mm cells at different times may be found in section 4.8 where good agreement is observed across all measurements.

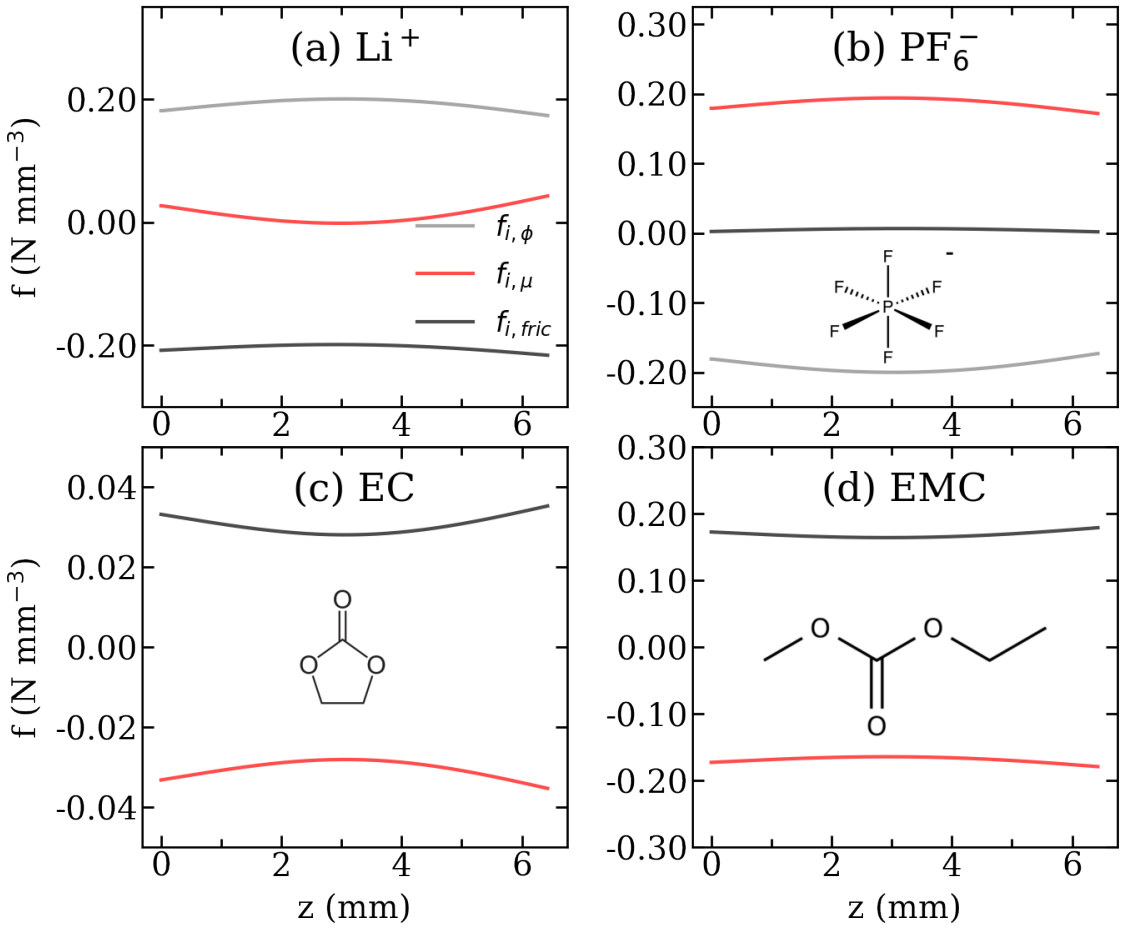

Figure 4.11: Simulated driving forces arising from friction, $f_{i,fric}$, chemical potential gradients, $f_{i,\mu}$ and electrostatic potential gradients, $f_{i,\phi}$ acting on the species in the electrolytes after applying a constant current of 0.25 mA cm^{-2} with a 6 mm distance between electrodes for 18 h in 1 M $LiPF_6$ in EC:EMC vol:vol 3:7. $f_{i,fric}$, $f_{i,\mu}$ and $f_{i,\phi}$ for (a) Li^+ and (b) PF_6^-. The driving forces acting on EC and EMC in the electrolyte are plotted in (c) and (d). EC and EMC do not experience an electrostatic driving force as they are charge neutral.

To understand the physical origins of the generated concentration gradients, we consider the driving forces acting on the electrolyte under the applied current. An external electrostatic potential is applied by the potentiostat to drive the specified current through the cell. From Figure 4.11a, Li^+ ions experience driving forces towards the cathode (z=6mm) from both electrostatic ($f_{i,\phi}$) and chemical ($f_{i,\mu}$) potential gradients due to the applied electrostatic potential and the consequent insertion and removal of Li^+ at the anode (z=0mm) and cathode. The concentration profile of Li^+ will continue to change until the driving forces from the chemical and electrostatic potential gradients equal the dynamic frictional forces ($f_{i,fric}$) arising from species surrounding the Li^+ ions that oppose their motion, including through molecular collisions and intermolecular interactions. From Figure 4.11b, $f_{i,\phi}$ and $f_{i,\mu}$ act in opposite directions for PF_6^-. The electrostatic potential applied by the potentiostat drives PF_6^- from the cathode to the anode due to its negative

charge. This generates a concentration gradient of PF_6^- across the cell creating a chemical potential gradient. $f_{i,\mu}$ acts to oppose the chemical potential gradient and consequently opposes $f_{i,\phi}$. The PF_6^- concentration profile continues to change until the net driving force resulting from the electrotatic and chemical potential gradients is cancelled out by the dynamic frictional force arising from collisions and interactions with the other electrolyte species. $f_{i,\mu}$ observed for EC and EMC in Figure 4.11c and d opposes the chemical potential gradients for EC and EMC arising from their concentration profiles, as shown in Figure 4.10. The concentration profiles observed for EC and EMC can be considered to arise from the solvent molecules in first solvation shells of Li^+ ions being dragged along with the migrating Li^+ ions as they move from the anode to the cathode.[29] The dragging of coordinated EC and EMC may also collide with their uncoordinated counterparts contributing to the concentration gradient. EMC may be dragged more strongly by Li^+ than EC due to its greater presence in the first solvation sheath. Consequently, larger concentration gradients are observed for EMC relative to EC due to Li^+ dragging. Their profiles continue to change until the chemical potential gradient arising from the concentration gradient equals the dragging force exerted on EC and EMC by Li^+ ions during its migration and consequent collisions between the coordinated and uncoordinated solvent molecules.

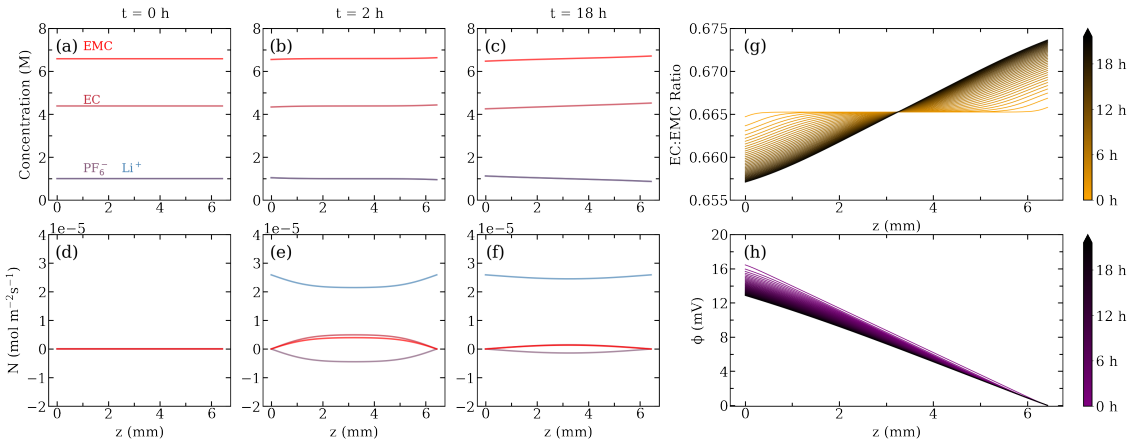

Figure 4.12: Predicted concentration gradients formed by applying a constant current of 0.25 mA cm^{-2} with a 6 mm distance between electrodes for (a) 0 h, (b) 2 h, (c) 18 h. Predicted molar flux densities in the electrolyte after applying the same current for (d) 0 h, (e) 2 h and (f) 18 h. (g) Variation of EC:EMC ratio across the electrolyte under the applied current density. (h) Electrostatic potential formed across the electrolyte due to the build up of Li^+ and PF_6^- concentration gradients.

The calculated parameters were used to predict how the concentration profiles, c_i=$x_i c_t$, and molar flux densities of each electrolyte species alongside the electrostatic potential vary with time. This is shown in Figure 4.12 for a constant current of 0.25 mA cm^{-2} with a 6 mm distance between electrodes. From Figure 4.12a-f, the concentration gradients and molar flux densities follow from the discussion on driving forces. Li^+, EC and EMC have positive molar flux densities indicating they migrate from the anode to the cathode. The opposite is true for PF_6^-. Ionic current in the electrolyte is carried by a combination of Li^+ and PF_6^- ions. The molar flux densities of EC and EMC are in the same direction of current flow due to the dragging effect of Li^+ ions resulting in uphill diffusion and the formation of their respective concentration gradients. Figure 4.12g shows the changes in the concentration ratio of EC:EMC across the length of the cell under the applied current. Solvent segregation is observed indicating the widely used single solvent approximation[18–20] does not hold for electrolyte systems containing cosolvents in agreement with recent literature.[21] From Figure 4.12h the electrostatic potential decreases across the cell driving Li^+ from the anode to the cathode and PF_6^- from the cathode to the anode in agreement with the earlier discussion on the driving forces. The magnitude of the applied current density determines the magnitude of the concentration gradients formed and consequently the surface concentrations of the electrolyte species at each electrode.

4.10 Discussion

The successful prediction of experimental concentration profiles from MD calculated MS diffusion parameters has provided key insights into the driving forces affecting molar flux densities and concentration gradients formed when a constant current is applied to an electrolyte. The applied electrostatic potential required for the specified current induces chemical ($f_{i,\mu}$) and electrostatic ($f_{i,\phi}$) forces both of which drive the cations being inserted into the electrolyte from the anode to the cathode where they're removed. Anions experience an electrostatic force driving against their chemical potential gradient from the cathode to the anode. At longer times, all the ionic current in the electrolyte is carried by the migration of Li^+ from the anode to the cathode and the concentration profiles stop changing. The solvent molecules are displaced in the direction of ionic current flow experiencing uphill diffusion owing to their solvation of the cations on the molecular scale.

4.11 Conclusions

The general MS diffusion framework was successfully applied to a 1 M $LiPF_6$ in EC:EMC vol:vol 3:7. We present a methodology to calculate the required diffusion coefficients and thermodynamic factors from MD in the MS diffusion framework which can then be tested against experimental concentration profiles measured using Raman spectroscopy, achieving a more accurate electrolyte model which can be readily incorporated into battery continuum scale modelling. This general, accurate description of the electrolyte can provide the surface concentrations of all electrolyte species to be simulated in the DFN model, paving the way for more accurate descriptions of the complex electrochemical processes occurring at the electrode-electrolyte interface. This work provides fundamental insight into the simulation of LIB electrolytes on the continuum scale which will aid the development and optimization of LIB electrolytes to enable the use of high voltage cathode materials in commercial LIBs.

Bibliography

[1] J. B. Goodenough and K. S. Park, "The Li-ion rechargeable battery: A perspective," 2013.

[2] Y. Miao, P. Hynan, A. Von Jouanne, and A. Yokochi, "Current li-ion battery technologies in electric vehicles and opportunities for advancements," 2019.

[3] S.-T. Myung, F. Maglia, K.-J. Park, C. Seung Yoon, P. Lamp, S.-J. Kim, and Y.-K. Sun, "Nickel-Rich Layered Cathode Materials for Automotive Lithium-Ion Batteries: Achievements and Perspectives," *ACS Energy Letters*, vol. 2, pp. 196–223, 12 2016.

[4] T. Chen, Y. Jin, H. Lv, A. Yang, M. Liu, B. Chen, Y. Xie, and Q. Chen, "Applications of Lithium-Ion Batteries in Grid-Scale Energy Storage Systems," 2020.

[5] H. Cheng, Q. Sun, L. Li, Y. Zou, Y. Wang, T. Cai, F. Zhao, G. Liu, Z. Ma, W. Wahyudi, Q. Li, and J. Ming, "Emerging Era of Electrolyte Solvation Structure and Interfacial Model in Batteries," 2022.

[6] W. M. Dose, I. Temprano, J. P. Allen, E. Björklund, C. A. O'Keefe, W. Li, B. L. Mehdi, R. S. Weatherup, M. F. De Volder, and C. P. Grey, "Electrolyte Reactivity at the Charged Ni-Rich Cathode Interface and Degradation in Li-Ion Batteries," *ACS Applied Materials and Interfaces*, vol. 14, no. 11, 2022.

[7] W. M. Dose, W. Li, I. Temprano, C. A. O'Keefe, B. Layla Mehdi, M. F. L. De Volder, and C. P. Grey, "Onset Potential for Electrolyte Oxidation and Ni-Rich Cathode Degradation in Lithium-Ion Batteries," *ACS Energy Letters*, vol. 7, pp. 3524–3530, 9 2022.

[8] C. M. E. Phelan, E. Bjorklund, J. Singh, M. Fraser, P. N. Didwal, G. J. Rees, Z. Ruff, P. Ferrer, D. C. Grinter, C. P. Grey, and others, "Role of Salt Concentration in Stabilizing Charged Ni-Rich Cathode Interfaces in Li-Ion Batteries," *Chemistry of Materials*, vol. 36, no. 7, pp. 3334–3344, 2024.

[9] J. Fawdon, J. Ihli, F. L. Mantia, and M. Pasta, "Characterising lithium-ion electrolytes via operando Raman microspectroscopy," *Nature Communications*, vol. 12, no. 1, 2021.

[10] J. Fawdon, G. J. Rees, F. La Mantia, and M. Pasta, "Insights into the Transport and Thermodynamic Properties of a Bis(fluorosulfonyl)imide-Based Ionic Liquid Electrolyte for Battery Applications," *Journal of Physical Chemistry Letters*, vol. 13, no. 7, 2022.

[11] S. Dhir, B. Jagger, A. Maguire, and M. Pasta, "Fundamental investigations on the ionic transport and thermodynamic properties of non-aqueous potassium-ion electrolytes," *Nature Communications*, vol. 14, no. 1, 2023.

[12] J. Zhao, B. Jagger, L. F. Olbrich, J. Ihli, S. Dhir, M. Zyskin, X. Ma, and M. Pasta, "Transport and Thermodynamic Properties of KFSI in TEP by Operando Raman Gradient Analysis," *ACS Energy Letters*, vol. 9, no. 4, 2024.

[13] A. A. Wang, A. B. Gunnarsdóttir, J. Fawdon, M. Pasta, C. P. Grey, and C. W. Monroe, "Potentiometric MRI of a Superconcentrated Lithium Electrolyte: Testing the Irreversible Thermodynamics Approach," *ACS Energy Letters*, vol. 6, no. 9, 2021.

[14] M. Klett, M. Giesecke, A. Nyman, F. Hallberg, R. W. Lindström, G. Lindbergh, and I. Furó, "Quantifying mass transport during polarization in a Li Ion battery electrolyte by in situ 7Li NMR imaging," *Journal of the American Chemical Society*, vol. 134, no. 36, 2012.

[15] A. K. Sethurajan, S. A. Krachkovskiy, I. C. Halalay, G. R. Goward, and B. Protas, "Accurate Characterization of Ion Transport Properties in Binary Symmetric Electrolytes Using In Situ NMR Imaging and Inverse Modeling," *Journal of Physical Chemistry B*, vol. 119, no. 37, 2015.

[16] S. A. Krachkovskiy, A. D. Pauric, I. C. Halalay, and G. R. Goward, "Slice-selective NMR diffusion measurements: A robust and reliable tool for in situ characterization of ion-transport properties in Lithium-ion battery electrolytes," *Journal of Physical Chemistry Letters*, vol. 4, no. 22, 2013.

[17] M. Schalenbach, B. Hecker, B. Schmid, Y. E. Durmus, H. Tempel, H. Kungl, and R. A. Eichel, "Ionic transport modeling for liquid electrolytes - Experimental evaluation by concentration gradients and limited currents," *Electrochemical Science Advances*, vol. 3, no. 2, 2023.

[18] Y. Ugata, Y. Chen, S. Miyazaki, S. Sasagawa, K. Ueno, M. Watanabe, and K. Dokko, "High-concentration LiPF6/sulfone electrolytes: structure, transport properties, and battery application," *Physical Chemistry Chemical Physics*, vol. 25, no. 43, 2023.

[19] H. K. Bergstrom, K. D. Fong, and B. D. McCloskey, "Interfacial Effects on Transport Coefficient Measurements in Li-ion Battery Electrolytes," *Journal of The Electrochemical Society*, vol. 168, no. 6, 2021.

[20] J. Landesfeind and H. A. Gasteiger, "Temperature and Concentration Dependence of the Ionic Transport Properties of Lithium-Ion Battery Electrolytes," *Journal of The Electrochemical Society*, vol. 166, no. 14, 2019.

[21] A. A. Wang, S. Greenbank, G. Li, D. A. Howey, and C. W. Monroe, "Current-driven solvent segregation in lithium-ion electrolytes," *Cell Reports Physical Science*, vol. 3, no. 9, 2022.

[22] C. Delacourt, "Modeling Li-Ion Batteries with Electrolyte Additives or Contaminants," *Journal of The Electrochemical Society*, vol. 160, no. 11, 2013.

[23] C. Kupper and W. G. Bessler, " Multi-Scale Thermo-Electrochemical Modeling of Performance and Aging of a LiFePO 4 /Graphite Lithium-Ion Cell ," *Journal of The Electrochemical Society*, vol. 164, no. 2, 2017.

[24] C. Kupper, B. Weißhar, S. Rißmann, and W. G. Bessler, "End-of-Life Prediction of a Lithium-Ion Battery Cell Based on Mechanistic Aging Models of the Graphite Electrode," *Journal of The Electrochemical Society*, vol. 165, no. 14, 2018.

[25] C. W. Monroe, "Does Oxygen Transport Affect the Cell Voltages of Metal/Air Batteries?," *Journal of The Electrochemical Society*, vol. 164, no. 11, 2017.

[26] R. Li, S. O'Kane, A. Wang, T. Jung, N. Kirkaldy, M. Marinescu, C. W. Monroe, and G. J. Offer, "Lithium-ion battery performance model including solvent segregation effects," *arXiv preprint arXiv:2311.05467*, 2023.

[27] S. Plimpton, "Fast parallel algorithms for short-range molecular dynamics," *Journal of Computational Physics*, vol. 117, no. 1, 1995.

[28] W. L. Jorgensen, D. S. Maxwell, and J. Tirado-Rives, "Development and testing of the OPLS all-atom force field on conformational energetics and properties of organic liquids," *Journal of the American Chemical Society*, vol. 118, no. 45, 1996.

[29] T. Hou, K. D. Fong, J. Wang, and K. A. Persson, "The solvation structure, transport properties and reduction behavior of carbonate-based electrolytes of lithium-ion batteries," *Chemical Science*, vol. 12, no. 44, 2021.

[30] G. A. Kaminski, R. A. Friesner, J. Tirado-Rives, and W. L. Jorgensen, "Evaluation and reparametrization of the OPLS-AA force field for proteins via comparison with accurate quantum chemical calculations on peptides," *Journal of Physical Chemistry B*, vol. 105, no. 28, 2001.

[31] K. P. Jensen and W. L. Jorgensen, "Halide, ammonium, and alkali metal ion parameters for modeling aqueous solutions," *Journal of Chemical Theory and Computation*, vol. 2, no. 6, 2006.

[32] N. Kumar and J. M. Seminario, "Lithium-ion model behavior in an ethylene carbonate electrolyte using molecular dynamics," *Journal of Physical Chemistry C*, vol. 120, no. 30, 2016.

[33] R. Jorn, R. Kumar, D. P. Abraham, and G. A. Voth, "Atomistic modeling of the electrode-electrolyte interface in Li-ion energy storage systems: Electrolyte structuring," *Journal of Physical Chemistry C*, vol. 117, no. 8, 2013.

[34] M. D. Hanwell, D. E. Curtis, D. C. Lonie, T. Vandermeerschd, E. Zurek, and G. R. Hutchison, "Avogadro: An advanced semantic chemical editor, visualization, and analysis platform," *Journal of Cheminformatics*, vol. 4, no. 8, 2012.

[35] L. Martinez, R. Andrade, E. G. Birgin, and J. M. Martínez, "PACKMOL: A package for building initial configurations for molecular dynamics simulations," *Journal of Computational Chemistry*, vol. 30, no. 13, 2009.

[36] A. I. Jewett, D. Stelter, J. Lambert, S. M. Saladi, O. M. Roscioni, M. Ricci, L. Autin, M. Maritan, S. M. Bashusqeh, T. Keyes, R. T. Dame, J. E. Shea, G. J. Jensen, and D. S. Goodsell, "Moltemplate: A Tool for Coarse-Grained Modeling of Complex Biological Matter and Soft Condensed Matter Physics," *Journal of Molecular Biology*, vol. 433, no. 11, 2021.

[37] W. M. Brown, P. Wang, S. J. Plimpton, and A. N. Tharrington, "Implementing molecular dynamics on hybrid high performance computers - Short range forces," *Computer Physics Communications*, vol. 182, no. 4, 2011.

[38] W. M. Brown, A. Kohlmeyer, S. J. Plimpton, and A. N. Tharrington, "Implementing molecular dynamics on hybrid high performance computers - Particle-particle particle-mesh," *Computer Physics Communications*, vol. 183, no. 3, 2012.

[39] W. M. Michael Brown and M. Yamada, "Implementing molecular dynamics on hybrid high performance computers - Three-body potentials," *Computer Physics Communications*, vol. 184, no. 12, 2013.

[40] T. D. Nguyen and S. J. Plimpton, "Accelerating dissipative particle dynamics simulations for soft matter systems," *Computational Materials Science*, vol. 100, no. PB, 2015.

[41] T. D. Nguyen, "GPU-accelerated Tersoff potentials for massively parallel Molecular Dynamics simulations," *Computer Physics Communications*, vol. 212, 2017.

[42] V. Nikolskiy and V. Stegailov, "GPU acceleration of four-site water models in LAMMPS," in *Advances in Parallel Computing*, vol. 36, 2020.

[43] M. Kohns, S. Reiser, M. Horsch, and H. Hasse, "Solvent activity in electrolyte solutions from molecular simulation of the osmotic pressure," *Journal of Chemical Physics*, vol. 144, no. 8, 2016.

[44] R. Taylor and R. Krishna, *Multicomponent mass transfer*, vol. 2. John Wiley & Sons, 1993.

[45] X. Liu, T. J. Vlugt, and A. Bardow, "Predictive Darken equation for Maxwell-Stefan diffusivities in multicomponent mixtures," *Industrial and Engineering Chemistry Research*, vol. 50, no. 17, 2011.

[46] R. Krishna and J. M. Van Baten, "The darken relation for multicomponent diffusion in liquid mixtures of linear alkanes: An investigation using Molecular Dynamics (MD) simulations," *Industrial and Engineering Chemistry Research*, vol. 44, no. 17, 2005.

[47] M. McEldrew, Z. A. H. Goodwin, S. Bi, A. A. Kornyshev, and M. Z. Bazant, "Ion Clusters and Networks in Water-in-Salt Electrolytes," *Journal of The Electrochemical Society*, vol. 168, no. 5, 2021.

[48] J. Newman and K. E. Thomas-Alyea, *Electrochemical systems. Third edition*. 2004.

Chapter 5

The effect of electrolyte salt concentration on electrochemical stability

5.1 Abstract

The electrochemical stability of LIB electrolytes is heavily influenced by the salt and solvent species, as already highlighted by the study in chapter 3. To discover new electrolyte formulations that offer wider electrochemical stability windows and facilitate improved battery cycling and capacity retention, a comprehensive understanding of the factors affecting electrolyte's stability must be achieved. Here we investigate the role of salt concentration in the determination of the solvation structures formed on the molecular scale, their electronic structure and finally their effect on the overall electrochemical stability in a LIB electrolyte ($LiPF_6$ in EC:EMC vol:vol 3:7). MD simulations and Raman measurements reveal the formation of CIP and AGG and an increase in the number of EC and EMC molecules involved in direct Li^+ solvation in the more highly concentrated electrolytes. DFT calculations of these solvation structures suggest EC is preferentially oxidised over EMC and PF_6^- at lower salt concentrations as its HOMO has a higher energy. In the more highly concentrated electrolytes, the PF_6^- HOMO energy increases above that of EC, resulting in the preferential oxidation of PF_6^- over EC. The electrolyte LUMO states are dominated by EC at all salt concentrations, resulting in its preferential reduction over EMC and PF_6^- at lower potentials. XAS measurements of the electrolyte O K-edge show the oxygen LUMO states shift to higher excitation energies with increasing salt concentration indicating higher salt concentrations improve overall solvent stability against reduction. This work has shed light on the link between solvation

environment, electronic structure and electrochemical stability in LIB electrolytes. This will aid in the formulation of new electrolytes exhibiting wider electrochemical stability windows to facilitate the use of commercial high voltage LIB cathodes.

5.2 Introduction

Current commercial liquid electrolytes consist of a mixture of linear and cyclic carbonates coupled with a lithium salt possessing a weakly coordinating anion and additives. However these electrolytes are limited by poor solvent stability, in particular at high potentials.[1,2] To mitigate against these issues, recent attention has been paid to highly concentrated electrolytes owing to their improved electrochemical and thermal stabilities.[3–7] The electronic structure of the electrolyte determines its electrochemical stability[8] with the HOMO and LUMO energies playing a vital role in the oxidative and reductive stabilities.

Herein, electrolyte solvation environments are investigated using MD simulations, Raman and XAS measurements. CIPs and AGGs emerge with increasing salt concentration and the number of EC and EMC molecules involved in direct Li^+ solvation increases. DOS calculations reveal EC is preferentially oxidised over EMC and PF_6^- at lower salt concentrations. The electrolyte LUMO states are dominated by EC, accounting for its preferential reduction over EMC and PF_6^- at lower potentials on graphite electrodes. XAS reveals the oxygen LUMO states shift to higher excitation energies with increasing salt concentration, suggesting higher salt concentrations improve overall solvent stability against reduction.[8] This work has unveiled the link between solvation environment, electronic structure and electrochemical stability in LIB electrolytes. This will aid in the formulation of new electrolytes exhibiting improved electrochemical properties assisting the incorporation of high voltage cathodes into commercial LIBs.

5.3 Experimental and theoretical methods

Electrolyte Preparation

Ethylene Carbonate (EC, 99+%, Acros Organics) and Ethyl Methyl Carbonate (EMC, 99.95+%, Solvionic) were mixed in a volume:volume ratio of 3:7 and dried for 24 hours using dried molecular sieves (3 Å, beads, 8-12 mesh , Sigma Aldrich). The water content of this mixture was measured using Karl Fischer titration and was found to be 3.3 ppm. Lithium Hexafluorophosphate ($LiPF_6$, 98+ %, Fisher Scientific) was dried under dynamic vacuum at 1-2 mbar at 30 ^{o}C for 24 hours. Electrolytes were mixed to differing molarities (0.5 - 4.2 M), with the EC:EMC mixture considered as the solvent. Glass fiber (GF) separators (borosilicate, grade GF/ A, Whatman) were dried at 100 ^{o}C under dynamic vacuum at 1-2 mbar for 24 hours prior to use.

Raman Spectroscopy

A Renishaw inVia Reflex laser confocal Raman microscope using a 785nm near-IR Laser, a 5$\times$ magnification objective (Leica, 0.12 NA, 14 mm WD), a 1200 gr/mm grating and a 90^o mirror yielding a spot size of $\sim$4 μm was used for operando Raman measurements. Spectra were recorded with a centre of 1050 cm^{-1} at 5% laser power (15 mW) with a 1 s exposure time and were repeated 30 times at each point. Spectra were recorded at 51 different points in the sample along the optical cell. The background for each spectrum was removed with the baseline correction method proposed by Zhang and coworkers[9] and normalised against against the area under the $-CH_2$ bending modes for EMC and EC at 1440 cm^{-1} and 1480 cm^{-1} respectively.

Operando XAS

The operando cell used here is described in our previous work.[10] SiN_x membranes facilitate X-ray transparency into the electrolyte (Silson, 100 nm window thickness, 0.5 mm $\times$ 0.5 mm window area, 5.0 mm $\times$ 5.0 mm frame area, 200 μm frame thickness). A $\varnothing$3 mm hole through the center of the PEEK flange allows the insertion of a $\varnothing$3 mm glass-fibre separator (Whatman, Borosilicate, dried at 100 ^{o}C in a vacuum oven) soaked in electrolyte. Cell assembly was performed within an Ar-filled glove-box (H_2O < 0.1 ppm, O_2 < 0.1 ppm). Viton O-rings are used to ensure a leak-tight seal against the vacuum conditions of the measurement chamber, avoiding evaporation of the liquid electrolyte. The excitation energies in the FY spectra were corrected such that the pre-edge feature in the O K-edge of a NiO reference sample measured after the electrolyte sample was at 532.8 eV for each sample.

Classical Molecular Dynamics

Classical molecular dynamics (MD) simulations were performed using the Large Scale Atomic/Molecular Massively Parallel Simulator (LAMMPS).[11] The non polarizable optimized potential for liquid simulations all-atom (OPLS-AA) forcefield was used to describe atomic interactions.[12] Arithmetic mixing rules in LAMMPS were used i.e. $\varepsilon_{ij} = \sqrt{\varepsilon_{ii}\varepsilon_{jj}}$, $\sigma_{ij} = \frac{\sigma_{ii}+\sigma_{jj}}{2}$. The bonded interactions were modelled as harmonic functions.[13] The non-bonded and bonded parameters for ethylene carbonate (EC) and ethyl methyl carbonate (EMC) were obtained from the OPLS-AA forcefield[12,14] and have recently been used in similar systems.[15] Restrained electrostatic potential (RESP) fitted atomic charges for EC and EMC were taken from Hou et al.[13] The LJ parameters for the Li^+ ion were taken from Jensen et al.[16] The parameters for the PF_6^- anions are from Kumar and Seminario[17] and Jorn et al.[18]

$LiPF_6$ in EC:EMC (vol:vol 3:7) with salt concentrations ranging from 0.5 - 4.2 M were simulated. The number of moelcules of EC to EMC required to give the desired ratio was determined by extracting the densities of each component separately under the isothermal–isobaric ensemble (constant NPT conditions). From these densities it was found the a mixture of 432 EMC molecules and 277 EC molecules corresponded to desired vol:vol 3:7 ratio. The number of $LiPF_6$ molecules was adjusted to give the desired concentration, with values ranging from 35 to 347. Topologies of single EC, EMC and $LiPF_6$ molecules were generated using the Avogadro software.[19] Initial configurations of the electrolyte system were generated using the Packing Optimization for Molecular Dynamics Simulations (PACKMOL) software.[20] Forcefield parameters were assigned to each atom using Moltemplate.[21] Periodic boundary conditions are applied in a cubic simulation box to represent the electrolyte bulk solution. The simulations were performed on an in-house machine utilising GPU acceleration from a Geforce GTX 1660 graphics card.[22–27] A Nose-Hoover thermostat and barostat are applied to maintain the desired temperatures and pressures. A timestep of 1 fs is used. The system is equilibrated in the isothermal–isobaric ensemble (constant NPT conditions) at 303.15 K for 2 ns, heated to 400 K over 1 ns, held there for 1 ns then cooled down to 303.15 K over 1 ns. The system is equilibrated for a further 1 ns at 303.15 K. Cell volumes and densities were then recorded for 5 ns and the equilibrium values at 303.15 K are extracted. A new cell is constrained to the equilibrium density in the canonical ensemble (constant NVT conditions) and equilibrated in the same way. Production runs are performed for 5 ns outputting atomic coordinates every 50 fs. Small electrolyte boxes of approximate dimension 25Å$\times$ 25Å$\times$ 25Åwere then constructed such that their density was the same as the large box for each salt concentration. The small boxes were equilibrated in the canonical ensemble (NVT) in a similar way to the large boxes. The production run was performed for 5 ns

with trajectories saved every 2000 fs. Snapshots for the small boxes were extracted and used to calculate DOS and core loss spectra for the 0.5 m and 4 m electrolyte. The center of mass (COM) radial distribution function (rdf)s and coordination number (CN) were calculated using the PyLat software.[28]

Density Functional Theory

Density functional theory (DFT) calculations were carried out using the plane wave pseudopotential linear scaling code ONETEP.[29] The Perdew-Burke-Ernzerhof (PBE) form of the generalized gradient approximation (GGA) functional[30] was used for DOS calculations. Atomic positions were generated using classical MD simulations. Appropriate plane wave cut-off energies and k-point spacing values were determined via convergence testing of both the total energy and bond lengths. The DOS of different snapshots were calculated for 0.5 m, 1.0 m and 4.0 m electrolytes.

5.4 Results

Electrolyte Solvation Structure

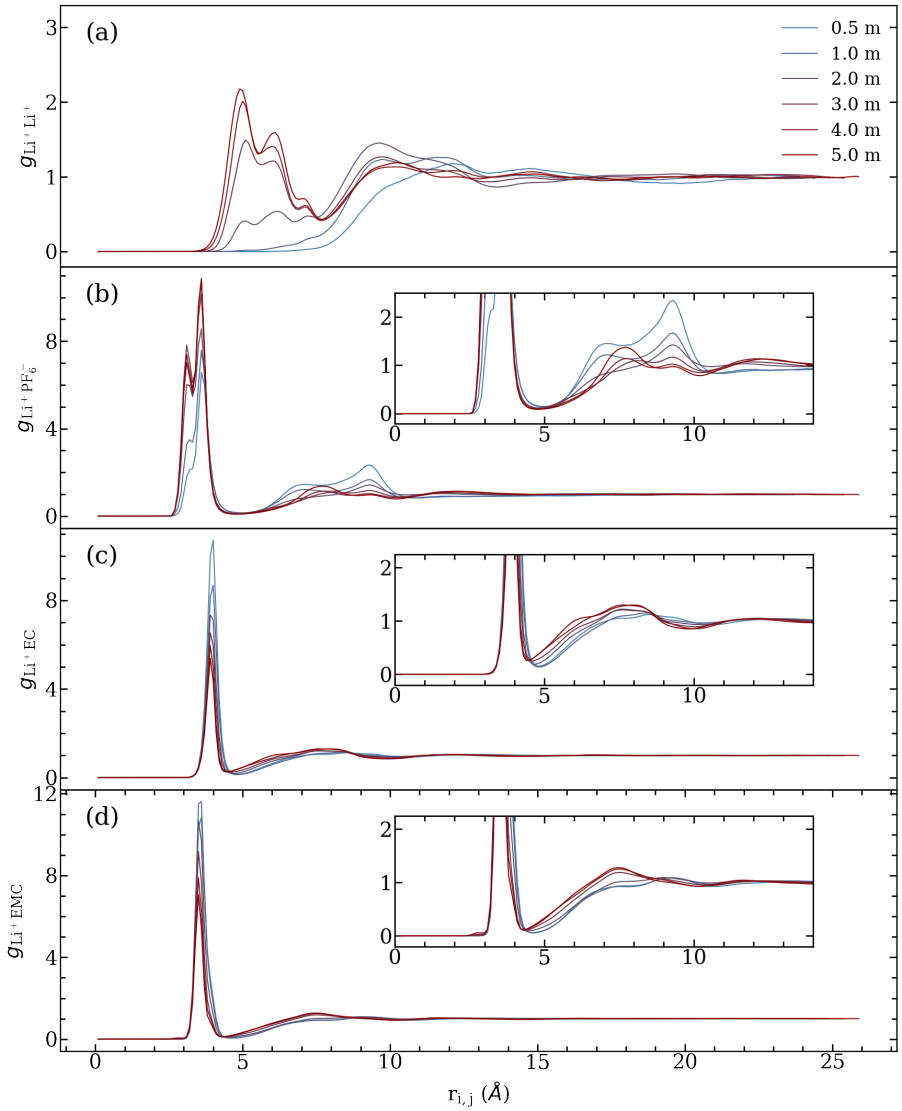

Figure 5.1: COM Li–X rdfs for (a) X=Li^+, (b) X = PF_6^-, (c) EC and (d) EMC for different concentrations of $LiPF_6$ in EC:EMC vol:vol 3:7. The region between 0 - 0.4 nm is considered to be the first solvation layer around Li^+. These molecules/ions are considered to be bound to Li^+, forming a homogenized complex that does not necessarily have an integer number of solvating molecules.

Li^+ ions were observed to primarily solvate through the fluorine atoms in PF_6^- anions or through the carbonyl oxygens of EC and EMC molecules.[13] As salt concentration increases, several key changes occur. From Figure 5.1a, a peak emerges r=0.5 nm with increasing concentration, implying the formation of CIPs and AGGs at higher salt concentrations. The sharp peaks at 2.95 Å and 3.5 Å of Figure 5.1b indicate the presence

of PF_6^- ions in the first solvation sheath of Li ions. The sharp peaks observed at 3.8 Å in Figure 5.1c and 3.3 Å in Figure (5.1d) correspond to the presence of EC and EMC respectively in the first solvation shell of Li^+ ions.

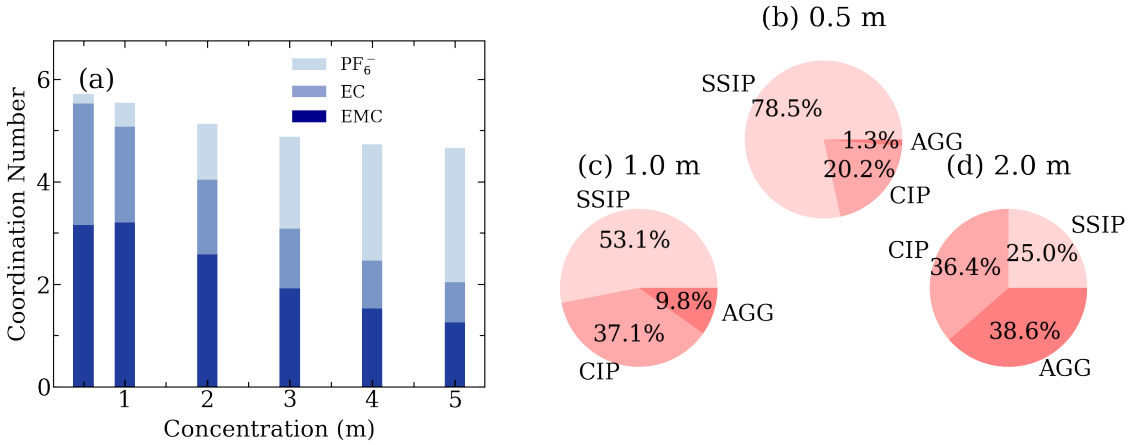

Figure 5.2: (a) Time-averaged coordination numbers in the first solvation shell of the Li^+ ions and (b)-(d) population of SSIP, CIP and AGGs for different concentrations of $LiPF_6$ in EC:EMC vol:vol 3:7.

Figure 5.2 shows the time-averaged coordination numbers and aggregate composition for different concentrations of $LiPF_6$ in EC:EMC vol:vol 3:7. Solvation structures in LIB electrolytes may be categorized into SSIP, CIPs and AGGs. Figure 5.2 demonstrates the time-averaged coordination numbers in the first solvation shell of the Li^+ ions, which are influenced by the nature of the solvation structures present. Figure 5.2 (b)-(d) display the populations of the different solvation structures at different salt concentrations. EC and EMC are present in the first solvation shell at all salt concentrations. At lower salt concentrations, Li^+ ions exist primarily as SSIPs resulting in the first solvation shell being primarily composed of EC and EMC molecules. As salt concentration increases, the emergence of CIPs and AGGs result in more PF_6^- in the first solvation shell in place of the EC and EMC molecules.

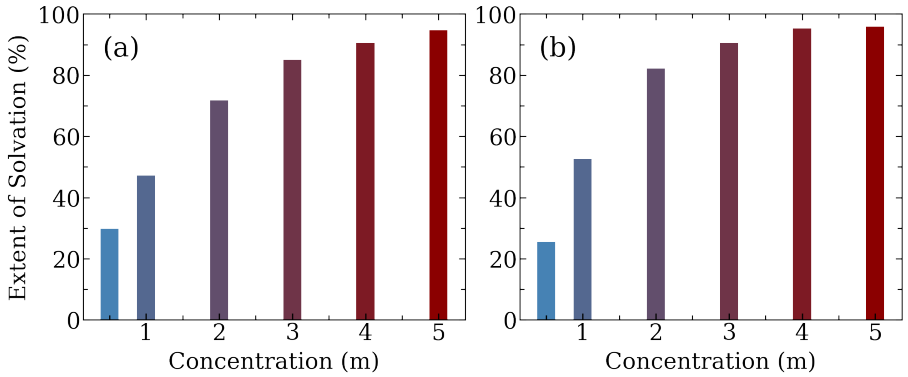

Figure 5.3: Extent of solvation showing the percentage of (a) EC and (b) EMC directly solvating Li^+ ions for different concentrations of $LiPF_6$ in EC:EMC vol:vol 3:7. At lower salt concentrations, unbound EC and EMC molecules are present while almost all solvent molecules are involved in direct Li^+ solvation in the highly concentrated electrolytes.

Figure 5.3 shows the extent of solvation (i.e. percentage of solvent molecules involved in direct Li^+ coordination) for different concentrations of $LiPF_6$ in EC:EMC vol:vol 3:7. In the more highly concentrated electrolytes, almost all EC and EMC molecules are bound in direct Li^+ ion solvation and are shared amongst a growing number of CIPs and AGGs which accounts for their decrease in the highly concentrated electrolytes as shown in Figure 5.2a. At lower salt concentrations, EC and EMC molecules experience both Li^+ bound and unbound environments, while in the more highly concentrated electrolytes the EC and EMC molecules exclusively experience the Li^+ bound environment in agreement with experimental observations.[31]

Raman Measurements

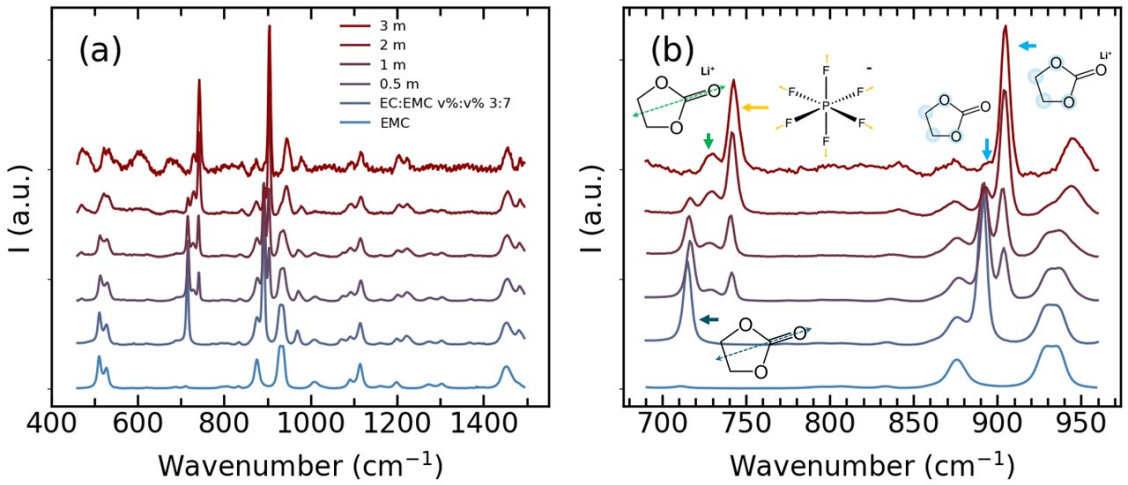

Figure 5.4: (a) Full Raman spectra for $LiPF_6$ in EC:EMC vol:vol 3:7 for different salt concentrations. (b) Zoomed in Raman spectra for $LiPF_6$ in EC:EMC at room temperature with EC and PF_6^- modes indicated.

The full Raman spectra collected for $LiPF_6$ in EC:EMC at various concentrations including pristine EMC are shown in Figure 5.4. The scattering efficiency of $LiPF_6$ has previously been observed to worsen with increasing salt concentration.[32] Neat EMC exhibits a broad peak at 928 and 937 cm^{-1} attributed to unsolvated C-O stretching modes affected by asymmetric ethyl and methyl groups in EMC.[33] The Li^+ solvating solvent peak for EMC emerges at 946 cm^{-1}.[31] The PF_6^- stretching band is expected at 741 cm^{-1} and increases in intensity with increasing salt concentration[31] and has been correlated with enhanced ion association.[34–36] Mixtures of EC and EMC in the absence of $LiPF_6$ exhibits a feature at 715 cm^{-1} attributed to unsolvated C-O stretching modes while a solvating solvent peak emerges at 730 cm^{-1} attributed to bound Li-EC interaction.[37] The unsolvated EC skeletal breathing mode is observed at 893 cm^{-1}, which also exhibits a solvated feature at 900 cm^{-1} with increasing salt concentration.[37] As salt concentration increases, the unsolvated features for both EC and EMC disappear, while the solvating solvent features increase in intensity suggesting more solvent molecules participate in Li^+ coordination for the more highly concentrated electrolytes.

XAS

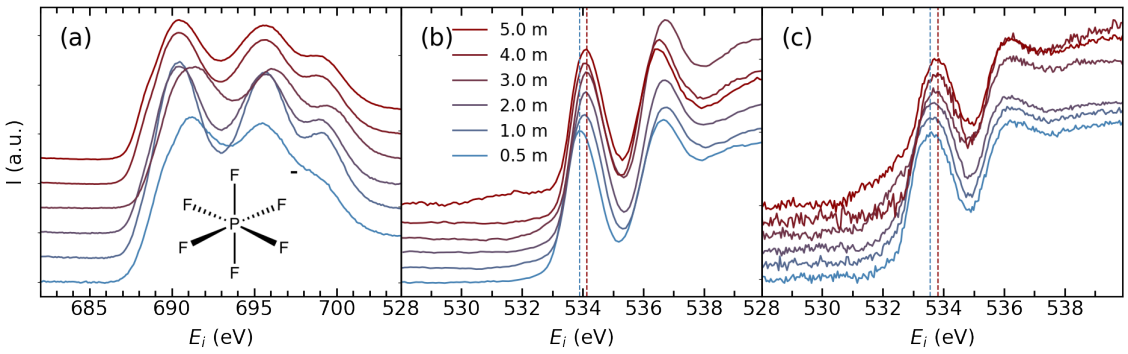

Figure 5.5: FY measurements of the (a) F K-edge and (b) O K-edge. (c) IPFY XAS measurements for the O K-edge of $LiPF_6$ in EC:EMC vol:vol 3:7 electrolyte at different salt concentrations.

Figure 5.5 display the results of operando FY measurements for the F K-edge and O K-edge for alongside IPFY XAS measurements performed for the O K-edge for $LiPF_6$ in EC:EC vol:vol 3:7 at different salt concentrations. The F K-edge shows three clear peaks ≈691.0 eV, ≈696.0 eV and ≈699.6 eV. These correspond closely to the expected line-shape for PF_6^- ions[38–40] and closely resembles findings from our previous work.[10] No clear and obvious trends were observed in the F K-edge with increasing salt concentration, leading to no further analysis of these spectra. However, changes in the O K-edge were observed with increasing salt concentration. Two strong peaks are observed at 534 eV and 537 eV. These features have been attributed to transitions from the 1s-π^* states for carbonyl and ring oxygens respectively in carbonate molecules.[41] The broader states at higher excitation energies represent 1s-σ^* transitions. As $LiPF_6$ salt concentration is increased, the electrolyte features remain relatively unchanged in overall shape. However, we note a distinct shift for the peak at ≈ 534 eV to higher excitation energies in both the FY and IPFY spectra.

DFT

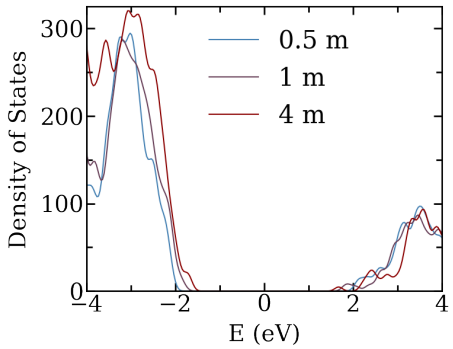

Figure 5.6: Total DOS calculated for 0.5 m, 1.0 m and 4.0 m $LiPF_6$ in EC:EMC vol:vol 3:7 electrolyte. For the higher salt concentrations, new features emerge at -1.8 eV for the HOMO and 1.7 eV for the LUMO.

Figure 5.6 shows the total density of states calculated for 0.5 m, 1.0 m and 4.0 m electrolytes with ONETEP using snapshots from the small electrolyte boxes generated with MD. As salt concentration increases, the energy difference between the HOMO and LUMO orbitals decreases. New features in the DOS are observed at -1.8 eV and 1.7 eV in the 4.0 m electrolyte. To understand the origin of these changes, we consider the DOS of the EC and EMC molecules separately.

Figure 5.7 shows the DOS for each of the atoms in EC and PF_6^- at different salt concentrations. As salt concentration increases, it is evident the new HOMO and LUMO states arising at higher salt concentrations originate from the EC molecules, in particular the carbonyl oxygen (O_C) and carbon (C_C) atoms. On further investigation these features originate from EC molecules solvating Li^+ whose structures are perturbed relative to non-coordinating EC molecules. Lower energy LUMOs and higher energy HOMOs are believed to facilitate easier reduction and oxidation in cathodic and anodic systems respectively,[42–44] resulting in low kinetic stability and high chemical reactivity as it is more energetically favourable to add electrons to the lower energy LUMO and remove electrons from the higher energy HOMO.[45] The lower energy gap between the HOMO and LUMO in the more highly concentrated electrolytes in isolation would suggest it is less stable against oxidation and reduction. However, results from chapter 3 indicate this is not the case. The extent of this perturbation may arise from inaccuracies in the forcefield resulting in an unrealistic structure. More sampling of different snapshots would mitigate this issue as outliers such as these will be averaged out, however due to computational constraints only a small number of snapshots could be sampled. Most of the LUMO states are dominated by contributions from EC. As salt concentration increases, there is increased overlap between the EC hydrogen and chain carbon and the F atom states from the PF_6^- anion in the HOMO at -3.2 eV. There is also a slight shift in the EC hydrogen

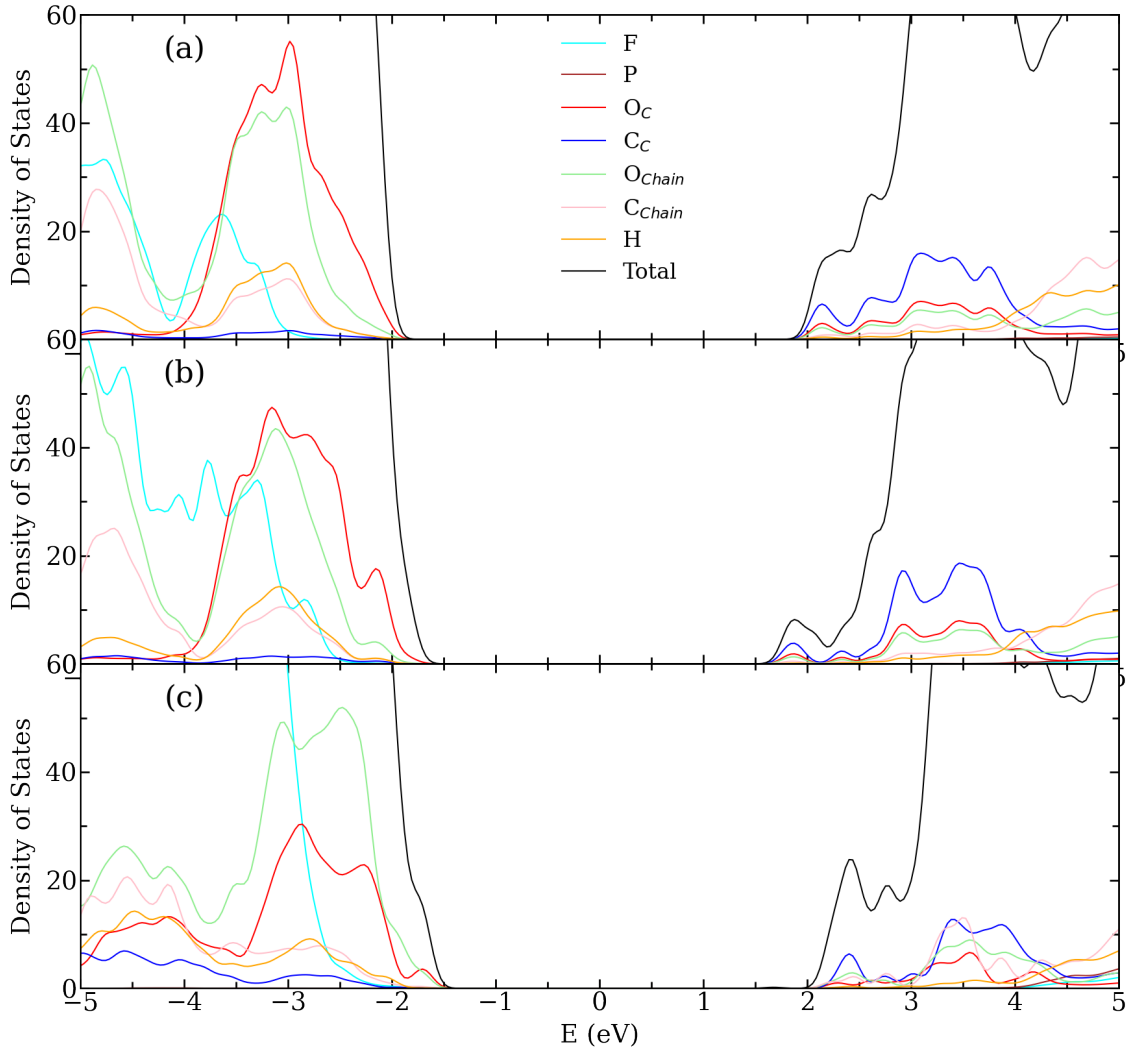

Figure 5.7: DOS for EC and PF_6^- in (a) 0.5 m, (b) 1.0 m and (c) 4.0 m $LiPF_6$ in EC:EMC vol:vol 3:7 electrolyte. The HOMO bulge at -1.8 eV and the new LUMO feature observed in the total DOS are observed to originate from the EC species. No P states were observed to have energies near the LUMO or HOMO for all salt concentrations.

and chain carbon states to lower energies.

Figure 5.8 shows the DOS for each of the atoms in EMC and PF_6^- at different salt concentrations. Similar to EC, the carbonyl and chain oxygen contributions dominate the EMC HOMO states and are shifted to higher energies with increasing salt concentration. The hydrogen and chain carbon states also experience increased overlap with the fluorine states from the PF_6^- ion in the more highly concentrated electrolytes. The LUMO EMC states have higher energies relative to EC and do not strongly contribute to the lowest energy LUMO states. Additionally, no significant contributions from phosphorous, lithium or fluorine are observed in the LUMO states.

Figure 5.9 shows the DOS for solvated and unsolvated EC and EMC molecules at different

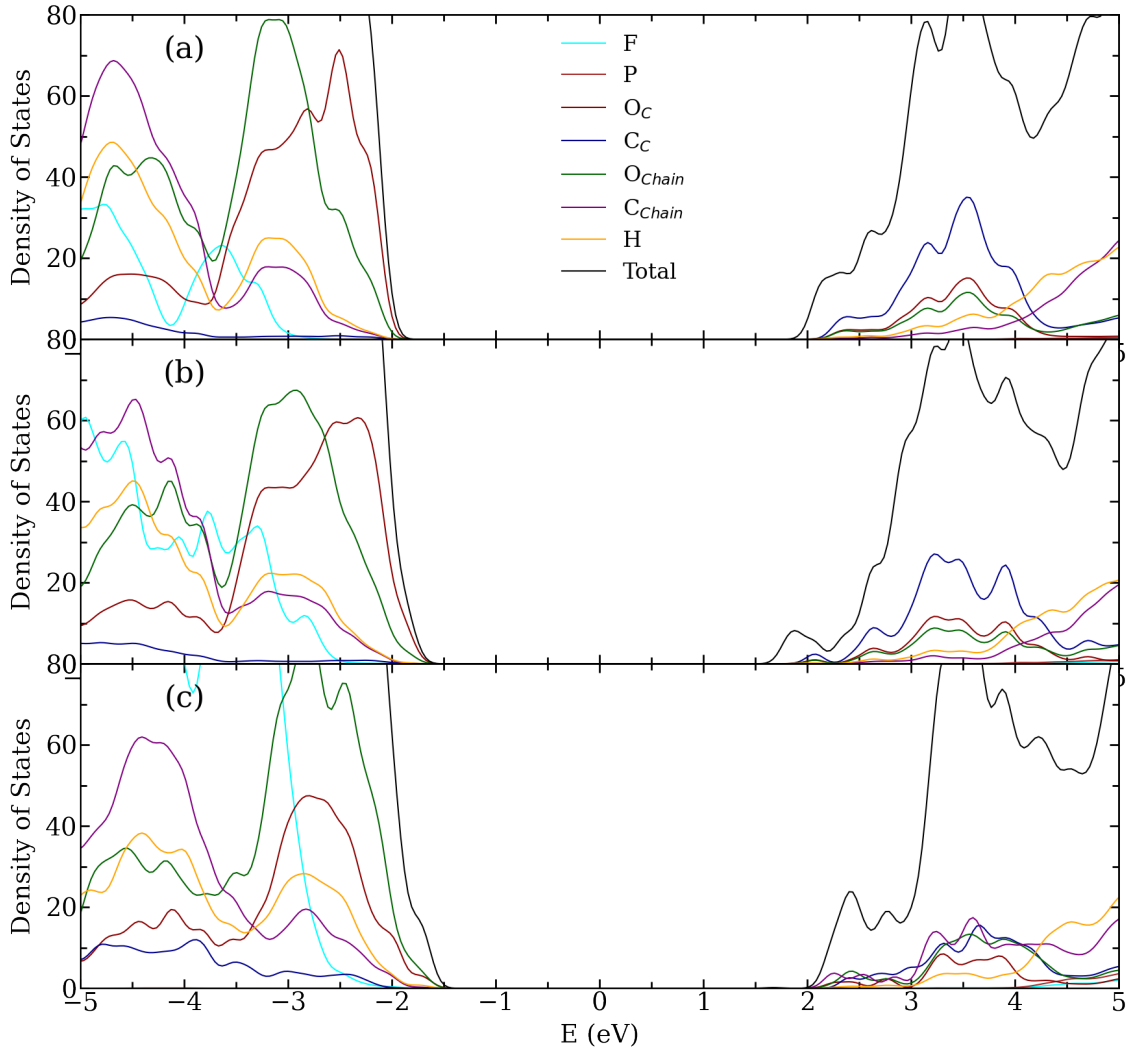

Figure 5.8: DOS for EMC and PF_6^- in (a) 0.5 m, (b) 1.0 m and (c) 4.0 m $LiPF_6$ in EC:EMC vol:vol 3:7 electrolyte. The LUMO states arising from EMC atoms are shifted to higher energies with increasing salt concentration. More overlap between the fluorine states from PF_6^- and the hydrogen and chain carbon states in EMC is observed in the more highly concentrated electrolytes. No P states were observed to have energies near the LUMO or HOMO for all salt concentrations.

salt concentrations. In the context of Li^+ solvation by carbonate molecules, it has been reported the lone pair from carbonyl oxygen interacts with the unoccupied electronic states of the Li^+ ions.[46] Interestingly, no clear differences in the DOS between the solvated and unsolvated solvent molecules are observed in the 0.5 m and 1.0 m electrolytes. In the 4.0 m electrolyte, differences in DOS between the solvated and unsolvated molecules are observed. However, in the 4.0 m electrolyte very few solvent molecules are unsolvated. Consequently, the DOS from the solvated molecules are likely subject to poor statistics due to the small sample size. A clearer trend is observed when comparing different salt concentrations. The HOMO states are shifted to higher energy values for both solvated and unsolvated EC and EMC molecules. The LUMO states show less clear trends with

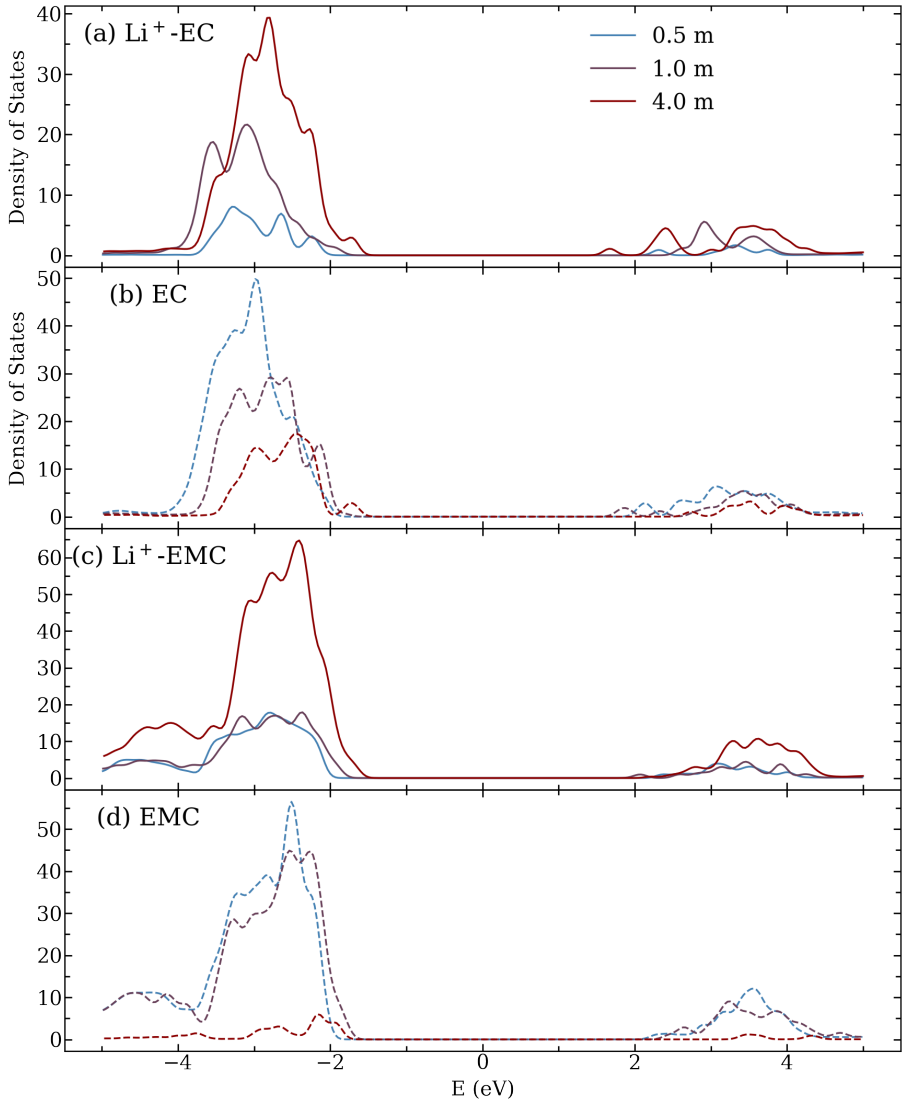

Figure 5.9: DOS for (a) solvated EC, (b) solvated EMC, (c) unsolvated EC and (d) unsolvated EMC in different concentrations of $LiPF_6$ in EC:EMC vol:vol 3:7 electrolyte.

increasing salt concentration, however we again note that the LUMO orbitals of EC are lower in energy than that of EMC in both the solvated and unsolvated cases.

5.5 Discussion

From the MD simulations, at lower salt concentrations the Li^+ solvation environment is dominated by EC and EMC molecules,with few CIPs and AGGs present in the electrolyte. As salt concentration increases, the number of PF_6^- in the first solvation shell of Li^+ increases by replacing EC and EMC as CIPs and AGGs form (Figure 5.2). The EC and EMC are shared amongst an increasing number of Li^+ ions. Indeed, almost all EC and EMC are involved in direct Li^+ solvation in the more highly concentrated electrolytes (Figure 5.3). The increasing extent of solvation for both EC and EMC is supported by the Raman results. Figure 5.4 indicates the disappearance of unsolvated EC and EMC features and the emergence of solvated features for both in the more highly concentrated electrolytes. From Figure 5.5, the pre-edge O K-edge XAS feature shifting to higher excitation energies indicates the LUMO energies of the oxygen atoms are increasing with increasing salt concentration. The shift does not seem to originate from carbonyl oxygens directly solvating to Li^+ ions as shown in Figure 5.9. This combined with the MD results indicates the shift must arise due to the formation of CIPs and AGGs resulting in enhanced interactions between the PF_6^- ions and the solvent molecules.

The shift does not seem to originate from carbonyl oxygens directly solvating to Li^+ ions as shown in Figure 5.9. This combined with the MD results indicates the shift must arise due to the formation of CIPs and AGGs resulting in enhanced interactions between the PF_6^- ions and the solvent molecules.

We interpret the changes in electrolyte electronic structure in the context of electrochemical redox stability as described by Bard and Faulkner.[8] Proposed reaction mechanisms for the chemical oxidation of EC assert the chain carbons and hydrogens are involved in the initial step.[47–49] Furthermore, the lower oxidative stability of EC relative to EMC has been demonstrated for charged Ni rich cathode interfaces.[1,2] As salt concentration increases, the HOMO fluorine states for PF_6^- overlap more with the EC and EMC chain carbons and hydrogen atoms (Figures 5.7, 5.8). Furthermore the HOMO DOS of EMC chain carbon and hydrogen atoms lie at lower energies than that of EC, in particular at lower salt concentrations accounting for the improved oxidative stability of EMC over EC. At lower salt concentrations, EC is oxidised before EMC and PF_6^- as its chain carbon and hydrogen HOMO is found at higher energies. As salt concentration increases, occupied fluorine states from PF_6^- overlap more with the HOMO of the EC chain carbons and hydrogen HOMO states. Consequently more PF_6^- will become oxidised relative to EC as the PF_6^- HOMO occupies higher energies. In the highly concentrated electrolytes, the large number of fluorine atom HOMO states from PF_6^- and their higher energy relative to the EC chain carbon and hydrogen HOMO states results in enhanced PF_6^- oxidation over EC.

This description accounts for earlier results in this work, which demonstrated improved electrolyte electrochemical stability at charged NMC811 interfaces in the more highly concentrated electrolytes and the formation of a $Li_xPO_yF_z$-/LiF-rich CEI passivating the surface against further reactions.

EC has been shown to be preferentially reduced over other linear and cyclic carbonates on porous and metal electrodes cycled to low potentials, forming lithium ethylene dicarbonate, $(CH_2OCO_2Li)_2$ (LED) as part of a SEI which passivates against further electrolyte decomposition.[50–54] From Figures 5.7, 5.8, the LUMO states in $LiPF_6$ in EC:EMC vol:vol 3:7 electrolyte are dominated by the carbonyl oxygen and carbon contributions at all salt concentrations. Consequently, the preferential reduction of EC over EMC is due to the LUMOs of EMC lying at higher energies relative to EC LUMOs. Interestingly, no PF_6^- molecular orbitals are observed near the electrolyte LUMOs, indicating $LiPF_6$ is reduced at much higher energies (lower potentials) relative to EC and EMC. The shift in the LUMO states to higher excitation energies observed in the XAS results suggest the solvent species will exhibit overall improved electrochemical stability against reduction in the more highly concentrated electrolytes.

5.6 Conclusions

New understanding of the effect of $LiPF_6$ salt concentration on electrolyte electrochemical stability is brought to light by incorporating MD and DFT with XAS and Raman spectroscopy to characterize the solvation and electronic structures in both dilute and highly concentrated electrolytes. CIPs and AGGs form with increasing salt concentration, increasing the number of EC and EMC molecules involved in direct Li^+ solvation. EC is preferentially oxidised over EMC and PF_6^- at lower salt concentrations as the HOMO of its reacting components is found at a higher energy. In the more highly concentrated electrolytes, the PF_6^- HOMO energy increases above that of EC resulting in the preferential oxidation of PF_6^- over EC. The electrolyte LUMO states are dominated by EC at all salt concentrations resulting in its preferential reduction over EMC and PF_6^- at low potentials. The electrolyte LUMO states shift to higher excitation energies with increasing salt concentration indicating higher salt concentrations improve overall solvent stability against reduction. This work has provided new insight into electrolyte solvation environments, electronic structure and their influence on the electrochemical stability of LIB electrolytes. This will aid in the development of new electrolyte formulations facilitating improved electrochemical stability at high voltage cathode surfaces by tailoring their solvation structures and electronic structure via their composition using diluents and additives.

Bibliography

[1] W. M. Dose, I. Temprano, J. P. Allen, E. Björklund, C. A. O'Keefe, W. Li, B. L. Mehdi, R. S. Weatherup, M. F. De Volder, and C. P. Grey, "Electrolyte Reactivity at the Charged Ni-Rich Cathode Interface and Degradation in Li-Ion Batteries," *ACS Applied Materials and Interfaces*, vol. 14, no. 11, 2022.

[2] W. M. Dose, W. Li, I. Temprano, C. A. O'Keefe, B. Layla Mehdi, M. F. L. De Volder, and C. P. Grey, "Onset Potential for Electrolyte Oxidation and Ni-Rich Cathode Degradation in Lithium-Ion Batteries," *ACS Energy Letters*, vol. 7, pp. 3524–3530, 9 2022.

[3] J. Wang, Y. Yamada, K. Sodeyama, C. H. Chiang, Y. Tateyama, and A. Yamada, "Superconcentrated electrolytes for a high-voltage lithium-ion battery," *Nature Communications*, vol. 7, 2016.

[4] L. Suo, O. Borodin, T. Gao, M. Olguin, J. Ho, X. Fan, C. Luo, C. Wang, and K. Xu, ""Water-in-salt" electrolyte enables high-voltage aqueous lithium-ion chemistries," *Science*, vol. 350, no. 6263, 2015.

[5] L. Suo, O. Borodin, Y. Wang, X. Rong, W. Sun, X. Fan, S. Xu, M. A. Schroeder, A. V. Cresce, F. Wang, C. Yang, Y. S. Hu, K. Xu, and C. Wang, ""Water-in-Salt" Electrolyte Makes Aqueous Sodium-Ion Battery Safe, Green, and Long-Lasting," *Advanced Energy Materials*, vol. 7, no. 21, 2017.

[6] W. Dai, N. Dong, Y. Xia, S. Chen, H. Luo, Y. Liu, and Z. Liu, "Localized concentrated high-concentration electrolyte enhanced stability and safety for high voltage Li-ion batteries," *Electrochimica Acta*, vol. 320, 2019.

[7] N. Takenaka, T. Fujie, A. Bouibes, Y. Yamada, A. Yamada, and M. Nagaoka, "Microscopic Formation Mechanism of Solid Electrolyte Interphase Film in Lithium-Ion Batteries with Highly Concentrated Electrolyte," *Journal of Physical Chemistry C*, vol. 122, no. 5, 2018.

[8] A. J. Bard and L. R. Faulkner, *Electrochemical Methods Fundamentals of Electrochemistry*, vol. 8. 2001.

[9] Z. M. Zhang, S. Chen, and Y. Z. Liang, "Baseline correction using adaptive iteratively reweighted penalized least squares," *Analyst*, vol. 135, no. 5, 2010.

[10] J. E. N. Swallow, M. W. Fraser, N.-J. H. Kneusels, J. F. Charlton, C. G. Sole, C. M. E. Phelan, E. Björklund, P. Bencok, C. Escudero, V. Pérez-Dieste, C. P. Grey, R. J. Nicholls, and R. S. Weatherup, "Revealing solid electrolyte interphase formation through interface-sensitive Operando X-ray absorption spectroscopy," *Nature Communications*, vol. 13, no. 1, p. 6070, 2022.

[11] S. Plimpton, "Fast parallel algorithms for short-range molecular dynamics," *Journal of Computational Physics*, vol. 117, no. 1, 1995.

[12] W. L. Jorgensen, D. S. Maxwell, and J. Tirado-Rives, "Development and testing of the OPLS all-atom force field on conformational energetics and properties of organic liquids," *Journal of the American Chemical Society*, vol. 118, no. 45, 1996.

[13] T. Hou, K. D. Fong, J. Wang, and K. A. Persson, "The solvation structure, transport properties and reduction behavior of carbonate-based electrolytes of lithium-ion batteries," *Chemical Science*, vol. 12, no. 44, 2021.

[14] G. A. Kaminski, R. A. Friesner, J. Tirado-Rives, and W. L. Jorgensen, "Evaluation and reparametrization of the OPLS-AA force field for proteins via comparison with accurate quantum chemical calculations on peptides," *Journal of Physical Chemistry B*, vol. 105, no. 28, 2001.

[15] T. Hou, G. Yang, N. N. Rajput, J. Self, S. W. Park, J. Nanda, and K. A. Persson, "The influence of FEC on the solvation structure and reduction reaction of LiPF6/EC electrolytes and its implication for solid electrolyte interphase formation," *Nano Energy*, vol. 64, 2019.

[16] K. P. Jensen and W. L. Jorgensen, "Halide, ammonium, and alkali metal ion parameters for modeling aqueous solutions," *Journal of Chemical Theory and Computation*, vol. 2, no. 6, 2006.

[17] N. Kumar and J. M. Seminario, "Lithium-ion model behavior in an ethylene carbonate electrolyte using molecular dynamics," *Journal of Physical Chemistry C*, vol. 120, no. 30, 2016.

[18] R. Jorn, R. Kumar, D. P. Abraham, and G. A. Voth, "Atomistic modeling of the electrode-electrolyte interface in Li-ion energy storage systems: Electrolyte structuring," *Journal of Physical Chemistry C*, vol. 117, no. 8, 2013.

[19] M. D. Hanwell, D. E. Curtis, D. C. Lonie, T. Vandermeerschd, E. Zurek, and G. R. Hutchison, "Avogadro: An advanced semantic chemical editor, visualization, and analysis platform," *Journal of Cheminformatics*, vol. 4, no. 8, 2012.

[20] L. Martinez, R. Andrade, E. G. Birgin, and J. M. Martínez, "PACKMOL: A package for building initial configurations for molecular dynamics simulations," *Journal of Computational Chemistry*, vol. 30, no. 13, 2009.

[21] A. I. Jewett, D. Stelter, J. Lambert, S. M. Saladi, O. M. Roscioni, M. Ricci, L. Autin, M. Maritan, S. M. Bashusqeh, T. Keyes, R. T. Dame, J. E. Shea, G. J. Jensen, and D. S. Goodsell, "Moltemplate: A Tool for Coarse-Grained Modeling of Complex Biological Matter and Soft Condensed Matter Physics," *Journal of Molecular Biology*, vol. 433, no. 11, 2021.

[22] W. M. Brown, P. Wang, S. J. Plimpton, and A. N. Tharrington, "Implementing molecular dynamics on hybrid high performance computers - Short range forces," *Computer Physics Communications*, vol. 182, no. 4, 2011.

[23] W. M. Brown, A. Kohlmeyer, S. J. Plimpton, and A. N. Tharrington, "Implementing molecular dynamics on hybrid high performance computers - Particle-particle particle-mesh," *Computer Physics Communications*, vol. 183, no. 3, 2012.

[24] W. M. Michael Brown and M. Yamada, "Implementing molecular dynamics on hybrid high performance computers - Three-body potentials," *Computer Physics Communications*, vol. 184, no. 12, 2013.

[25] T. D. Nguyen and S. J. Plimpton, "Accelerating dissipative particle dynamics simulations for soft matter systems," *Computational Materials Science*, vol. 100, no. PB, 2015.

[26] T. D. Nguyen, "GPU-accelerated Tersoff potentials for massively parallel Molecular Dynamics simulations," *Computer Physics Communications*, vol. 212, 2017.

[27] V. Nikolskiy and V. Stegailov, "GPU acceleration of four-site water models in LAMMPS," in *Advances in Parallel Computing*, vol. 36, 2020.

[28] M. T. Humbert, Y. Zhang, and E. J. Maginn, "PyLAT: Python LAMMPS Analysis Tools," *Journal of Chemical Information and Modeling*, vol. 59, no. 4, 2019.

[29] J. C. Prentice, J. Aarons, J. C. Womack, A. E. Allen, L. Andrinopoulos, L. Anton, R. A. Bell, A. Bhandari, G. A. Bramley, R. J. Charlton, R. J. Clements, D. J. Cole, G. Constantinescu, F. Corsetti, S. M. Dubois, K. K. Duff, J. M. Escartín, A. Greco, Q. Hill, L. P. Lee, E. Linscott, D. D. O'Regan, M. J. Phipps, L. E. Ratcliff, R. Serrano, E. W. Tait, G. Teobaldi, V. Vitale, N. Yeung, T. J. Zuehlsdorff, J. Dziedzic,

P. D. Haynes, N. D. Hine, A. A. Mostofi, M. C. Payne, and C. K. Skylaris, "The ONETEP linear-scaling density functional theory program," *Journal of Chemical Physics*, vol. 152, no. 17, 2020.

[30] J. P. Perdew, K. Burke, and M. Ernzerhof, "Generalized gradient approximation made simple," *Physical Review Letters*, vol. 77, no. 18, 1996.

[31] A. A. Wang, A. B. Gunnarsdóttir, J. Fawdon, M. Pasta, C. P. Grey, and C. W. Monroe, "Potentiometric MRI of a Superconcentrated Lithium Electrolyte: Testing the Irreversible Thermodynamics Approach," *ACS Energy Letters*, vol. 6, no. 9, 2021.

[32] L. Cabo-Fernandez, A. R. Neale, F. Braga, I. V. Sazanovich, R. Kostecki, and L. J. Hardwick, "Kerr gated Raman spectroscopy of LiPF6 salt and LiPF6-based organic carbonate electrolyte for Li-ion batteries," *Physical Chemistry Chemical Physics*, vol. 21, no. 43, 2019.

[33] A. Heckmann, J. Thienenkamp, K. Beltrop, M. Winter, G. Brunklaus, and T. Placke, "Towards high-performance dual-graphite batteries using highly concentrated organic electrolytes," *Electrochimica Acta*, vol. 260, 2018.

[34] K. Kondo, M. Sano, A. Hiwara, T. Omi, M. Fujita, A. Kuwae, M. Iida, K. Mogi, and H. Yokoyama, "Conductivity and Solvation of Li+ Ions of LiPF6 in Propylene Carbonate Solutions," *Journal of Physical Chemistry B*, vol. 104, no. 20, 2000.

[35] S. Hwang, D. H. Kim, J. H. Shin, J. E. Jang, K. H. Ahn, C. Lee, and H. Lee, "Ionic conduction and solution structure in LiPF6 and LiBF4 Propylene Carbonate Electrolytes," *Journal of Physical Chemistry C*, vol. 122, no. 34, 2018.

[36] S. D. Han, S. H. Yun, O. Borodin, D. M. Seo, R. D. Sommer, V. G. Young, and W. A. Henderson, "Solvate structures and computational/spectroscopic characterization of LiPF6 electrolytes," *Journal of Physical Chemistry C*, vol. 119, no. 16, 2015.

[37] E. Miele, W. M. Dose, I. Manyakin, M. H. Frosz, Z. Ruff, M. F. De Volder, C. P. Grey, J. J. Baumberg, and T. G. Euser, "Hollow-core optical fibre sensors for operando Raman spectroscopy investigation of Li-ion battery liquid electrolytes," *Nature Communications*, vol. 13, no. 1, 2022.

[38] A. S. Vinogradov, S. I. Fedoseenko, D. V. Vyalikh, S. L. Molodtsov, V. K. Adamchuk, C. Laubschat, and G. Kaindl, "High Resolution F1s Absorption Spectra of Solid Fluorides of 3d Elements," *Optics and Spectroscopy (English translation of Optika i Spektroskopiya)*, vol. 93, no. 6, 2002.

[39] A. S. Vinogradov, S. I. Fedoseenko, S. A. Krasnikov, A. B. Preobrajenski, V. N. Sivkov, D. V. Vyalikh, S. L. Molodtsov, V. K. Adamchuk, C. Laubschat, and G. Kaindl, "Low-lying unoccupied electronic states in 3d transition-metal fluorides probed by NEXAFS at the F 1s threshold," *Physical Review B - Condensed Matter and Materials Physics*, vol. 71, no. 4, 2005.

[40] K. Medjanik, A. Chernenkaya, X. Kozina, S. A. Nepijko, G. Öhrwall, P. Foury-Leylekian, P. Alemany, G. Schönhense, E. Canadell, and J. P. Pouget, "Near-Edge x-ray absorption fine structure investigation of the quasi-One-Dimensional organic conductor (TMTSF)2PF6," *Journal of Physical Chemistry A*, vol. 120, no. 43, 2016.

[41] J. W. Smith, R. K. Lam, A. T. Sheardy, O. Shih, A. M. Rizzuto, O. Borodin, S. J. Harris, D. Prendergast, and R. J. Saykally, "X-Ray absorption spectroscopy of LiBF4 in propylene carbonate: A model lithium ion battery electrolyte," *Physical Chemistry Chemical Physics*, vol. 16, no. 43, 2014.

[42] M. Villa, D. Miesel, A. Hildebrandt, F. Ragaini, D. Schaarschmidt, and A. Jacobi von Wangelin, "Synthesis and Catalysis of Redox-Active Bis(imino)acenaphthene (BIAN) Iron Complexes," *ChemCatChem*, vol. 9, no. 16, 2017.

[43] K. Hasan and E. Zysman-Colman, "Synthesis, UV-Vis and CV properties of a structurally related series of bis(Arylimino)acenaphthenes (Ar-BIANs)," *Journal of Physical Organic Chemistry*, vol. 26, no. 3, 2013.

[44] J. Huang, H. Ge, Z. Li, and J. Zhang, "Dynamic Electrochemical Impedance Spectroscopy of a Three-Electrode Lithium-Ion Battery during Pulse Charge and Discharge," *Electrochimica Acta*, vol. 176, 2015.

[45] N. S. Choi, S. Y. Ha, Y. Lee, J. Y. Jang, M. H. Jeong, W. C. Shin, and M. Ue, "Recent progress on polymeric binders for silicon anodes in lithium-ion batteries," 2015.

[46] M. Shakourian-Fard, G. Kamath, and S. K. Sankaranarayanan, "Evaluating the Free Energies of Solvation and Electronic Structures of Lithium-Ion Battery Electrolytes," *ChemPhysChem*, 2016.

[47] B. Rowden and N. Garcia-Araez, "A review of gas evolution in lithium ion batteries," in *Energy Reports*, vol. 6, 2020.

[48] B. L. Rinkel, D. S. Hall, I. Temprano, and C. P. Grey, "Electrolyte oxidation pathways in lithium-ion batteries," *Journal of the American Chemical Society*, vol. 142, no. 35, 2020.

[49] B. L. D. Rinkel, J. P. Vivek, N. Garcia-Araez, and C. P. Grey, "Two electrolyte decomposition pathways at nickel-rich cathode surfaces in lithium-ion batteries," *Energy & Environmental Science*, vol. 15, no. 8, pp. 3416–3438, 2022.

[50] G. V. Zhuang, K. Xu, H. Yang, T. R. Jow, and P. N. Ross, "Lithium ethylene dicarbonate identified as the primary product of chemical and electrochemical reduction of EC in 1.2 M LiPF 6/EC:EMC electrolyte," *Journal of Physical Chemistry B*, vol. 109, no. 37, 2005.

[51] D. Aurbach, B. Markovsky, A. Shechter, Y. Ein-Eli, and H. Cohen, "A Comparative Study of Synthetic Graphite and Li Electrodes in Electrolyte Solutions Based on Ethylene Carbonate-Dimethyl Carbonate Mixtures," *Journal of The Electrochemical Society*, vol. 143, no. 12, 1996.

[52] D. Aurbach, Y. Ein-Eli, B. Markovsky, A. Zaban, S. Luski, Y. Carmeli, and H. Yamin, "The Study of Electrolyte Solutions Based on Ethylene and Diethyl Carbonates for Rechargeable Li Batteries: II . Graphite Electrodes," *Journal of The Electrochemical Society*, vol. 142, no. 9, 1995.

[53] D. Aurbach, Y. Gofer, M. Ben-Zion, and P. Aped, "The behaviour of lithium electrodes in propylene and ethylene carbonate: Te major factors that influence Li cycling efficiency," *Journal of Electroanalytical Chemistry*, vol. 339, no. 1-2, 1992.

[54] A. Kominato, E. Yasukawa, N. Sato, T. Ijuuin, H. Asahina, and S. Mori, "Analysis of surface films on lithium in various organic electrolytes," *Journal of Power Sources*, vol. 68, no. 2, 1997.

Chapter 6

Summary and Future Work

6.1 Summary

This thesis has focused on the influence of salt concentration on solvation structure, transport and electrochemical stability in LIB electrolytes. Chapter 1 introduces highly concentrated electrolytes as a means to improve the electrochemical stability of LIB electrolytes to facilitate the widespread adoption of high voltage, Ni rich cathode materials in LIBs for electric vehicles and grid-scale energy storage systems.

Chapter 3 investigated the influence of salt concentration on electrolyte electrochemical stability at charged, NMC811 interfaces. This work demonstrated the formation of LiF/$Li_xPO_yF_z$ rich CEIs in highly concentrated electrolytes stemming from PF_6^- oxidation which passivates the reactive surface against continuous solvent degradation, attack from acidic species accompanied by RSL formation and TM dissolution. HF, formed by the reaction of PF_6^- with trace amounts of water in the electrolyte, then accumulates in the electrolyte as it can no longer gain access to the surface. This consequently results in enhanced GF separator degradation in the more highly concentrated electrolytes due to HF attack. Our results also indicate the electrochemical stability of the electrolyte at the NMC811 interface is dependent on both the CEI and the electrolyte salt concentration.

Chapter 4 investigated the relationship between the transport properties observed on the molecular scale and the behaviour of the electrolyte under an applied current using MS diffusion. The applied electrostatic potential required for the specified current induces chemical, $f_{i,\mu}$, and electrostatic, $f_{i,\phi}$, forces both of which drive the cations being inserted into the electrolyte from the anode to the cathode where they're removed. Anions experience an electrostatic force driving against their chemical potential gradient from the cathode to the anode. At steady state, the cations experience a constant driving force from

the anode to the cathode. Opposing chemical and electrostatic forces acting on the anion cancel each other out. Solvent molecules are displaced in the direction of ionic current flow experiencing uphill diffusion owing to their solvation of the cations on the molecular scale until the chemical potential driving force arising from their concentration gradients cancels out the dragging force exerted on them from Li^+ ion migration. The ratio of EC to EMC was demonstrated to vary across the length of the cell disproving the validity of the single solvent approximation in LIB continuum scale modelling.

Chapter 5 explores the relationship between the electrolyte solvation structure at the molecular scale and its electrochemical stability. MD simulations indicate almost all solvent molecules are involved in direct Li^+ coordination in the more highly concentrated electrolytes, supported by experimental Raman measurements. The number of PF_6^- directly coordinated to Li^+ also increases in the more highly concentrated electrolytes, replacing the solvent molecules which are shared amongst a growing number of Li^+ ions. XAS measurements of the O K-edge reveal a shift in the first peak associated with carbonyl oxygens to higher excitation energies in the more highly concentrated electrolytes, arising due increasing solvent participation in direct Li^+ coordination. DFT calculations reveal the HOMO states for PF_6^- overlap more with the solvent HOMO states int he more highly concentrated electrolytes, indicating that PF_6^- oxidation competes more with solvent oxidation at the cathode interface in the more highly concentrated electrolytes. This is in agrement with findings from chapter 3 demonstrating enhanced oxidation of PF_6^- at the NMC811 interface in the more highly concentrated electrolytes. The LUMO states were dominated by EC for all salt concentrations, consistent with the observation that EC reduced first during SEI formation in LIBs.

Overall, the results displayed in this thesis unveils the link between electrolyte solvation structure, transport properties and electrochemical stability and the role of salt concentration in varying these factors. In particular, the improved oxidative stability of $LiPF_6$ in EC:EMC (vol:vol 3:7) at higher salt concentrations has been revealed to arise from the PF_6^- HOMO states increasing in energy and density with increasing salt concentration resulting in their preferential oxidation over solvent molecules at the cathode surface in more highly concentrated electrolytes.

6.2 Future work

In chapter 3, the formation of lithium difluorophosphate (LDFP) species on the cathode surface in the more highly concentrated electrolytes was found to yield CEIs with improved electrochemical stability. Highly concentrated electrolytes suffer from poor ionic conductivities due to high viscosities and increased ionic association. Furthermore, results in chapter 3 indicate the CEI composition plays an appreciable role in electrolyte electrochemical stability at the charged NMC811 interface. LDFP like species were found to be present in the CEI in the more highly concentrated electrolyte. A potential avenue for further study could be to carry out a systematic study using LDFP as a variable electrolyte additive and at a standard concentration to investigate its influence on CEI composition and electrolyte electrochemical stability. This is an appealing solution to capture the enhanced electrochemical stability from more highly concentrated electrolytes while maintaining the good ionic conductivities and rate capabilities in standard electrolyte concentrations.

Chapter 4 calculated parameters for the MS diffusion model for a commonly used LIB electrolyte. An interesting follow up study could be incorporating this electrolyte description into the full DFN model. This would facilitate the incorporation of more accurate kinetic SEI formation and degradation models depending on the concentrations of each individual electrolyte species.

In chapter 5, to further validate the solvation structures generated using MD, calculating the core loss spectra for the electrolytes at different salt concentrations would be desirable. The simulated core loss spectra can then be compared to the measured O K-edge for the electrolyte to further support the electronic structure calculations performed in this chapter.

Overall, this thesis has explored the different factors influencing electrolyte electrochemical stability at high voltage NMC cathode interfaces, how stability stems from the electrolyte solvation structure on the molecular level and how these structures influence transport properties. This work has provided new understanding of LIB electrolytes to aid the formulation of novel electrolytes with enhanced electrochemical stability to facilitate the use of high voltage, Ni rich cathodes in commercial LIB batteries for electric vehicles and grid-scale energy storage systems.

Chapter 7

Appendix

7.1 A General BVP Solver in Python

Listing 7.1: AutoGrad.py

```
import numpy as np

class Dual(object):

    def __init__(self, real, dual={}, init=False):
        self.real = real
        self.dual=dual


    def __add__(self, argument):
        if isinstance(argument, Dual):
            real = self.real + argument.real
            dual={}
            for key in self.dual:
                dual[key] = self.dual[key]

            for key in argument.dual:
                if key in dual:
                    dual[key] += argument.dual[key]
                else:
                    dual[key] = argument.dual[key]


            return Dual(real, dual=dual, init=False)
        else:
            return Dual(self.real
            + argument, dual=self.dual,init=False)

    __radd__ = __add__

    def __sub__(self, argument):
        if isinstance(argument, Dual):
            real = self.real - argument.real
```

```
            dual= {}
            for key in self.dual:
                dual[key] = self.dual[key]


            for key in argument.dual:
                if key in dual:
                    dual[key] -= argument.dual[key]
                else:
                    dual[key] = -argument.dual[key]



            return Dual(real, dual=dual, init=False)
        else:
            return Dual(self.real -
            argument, dual=self.dual, init=False)
```

```
def __rsub__(self, argument):
    if isinstance(argument, Dual):
        real = -self.real + argument.real
        dual = {}
        for key in self.dual:
            dual[key] = -self.dual[key]

        for key in argument.dual:
            if key in dual:
                dual[key] += argument.dual[key]
            else:
                dual[key] = argument.dual[key]
```

```
            return Dual(real, dual=dual, init=False)
        else:
            dual={}
            for key in self.dual:
                dual[key] = -self.dual[key]
            return Dual(-self.real +argument, dual=dual, init=False)




def __mul__(self, argument):
    if isinstance(argument, Dual):

        real = self.real * argument.real
        dual = {}

        key1 = [i for i in self.dual]
        key2 = [i for i in argument.dual]
        keys = list(set(key1 + key2))

        for key in keys:
            if key in self.dual and key in argument.dual:
                a1=self.real
                b1=argument.real
                a2=self.dual[key]
                b2 = argument.dual[key]

                dual[key] = a1*b2 + a2*b1
            elif key in self.dual:
                a1=self.real
                b1=argument.real
                a2=self.dual[key]
                b2 = 0
                dual[key] = a1*b2 + a2*b1
            else:
                a1=self.real
                b1=argument.real
                a2=0
```

```
                b2 = argument.dual[key]
                dual[key] = a1*b2 + a2*b1
        return Dual(real, dual=dual, init=False)
    else:
        real = self.real * argument
        dual={}
        for key in self.dual:
            a1=self.real
            b1=argument
            a2=self.dual[key]
            b2 = 0
            dual[key] = a1*b2 + a2*b1
        return Dual(real, dual=dual, init=False)

__rmul__ = __mul__



def invert(self):
    a1=self.real
    dual={}
    for key in self.dual:
        a2 = self.dual[key]
        dual[key] = -a2/(a1*a1)
    return Dual(1/a1, dual=dual, init=False)




def __truediv__(self,argument):
    if isinstance(argument, Dual):
        inv = argument.invert()
        return self*inv
    else:
        inv = 1/argument
        return self*inv
```

```
def __rtruediv__(self,argument):
    inv = self.invert()
    return argument * inv

def __pow__(self, power):
    a1 = self.real
    dual={}
    for key in self.dual:
        a2 = self.dual[key]
        dual[key] = a2 * power * a1**(power-1)
    return Dual(a1**power, dual=dual, init=False)

def __neg__(self):
    return self*-1
def __pos__(self):
    return self*1

### Overload numpy functions
def sin(x):
    a1 = x.real
    dual={}
    for key in x.dual:
        a2 = x.dual[key]
        dual[key] = a2 * np.cos(a1)
    return Dual(np.sin(a1), dual=dual, init=False)

def sinh(x):
    a1 = x.real
    dual={}
    for key in x.dual:
        a2 = x.dual[key]
        dual[key] = a2 * np.cosh(a1)
    return Dual(np.sinh(a1), dual=dual, init=False)

def cos(x):
    a1 = x.real
    dual={}
```

```
    for key in x.dual:
        a2 = x.dual[key]
        dual[key] = a2 * -np.sin(a1)
    return Dual(np.cos(a1), dual=dual, init=False)

def cosh(x):
    a1 = x.real
    dual={}
    for key in x.dual:
        a2 = x.dual[key]
        dual[key] = a2 * -np.sinh(a1)
    return Dual(np.cosh(a1), dual=dual, init=False)

def exp(x):
    a1 = x.real
    dual={}
    for key in x.dual:
        a2 = x.dual[key]
        dual[key] = a2 * np.exp(a1)
    return Dual(np.exp(a1), dual=dual, init=False)


def log(x):
    a1 = x.real
    dual={}
    for key in x.dual:
        a2 = x.dual[key]
        dual[key] = a2 * 1/a1
    return Dual(np.log(a1), dual=dual, init=False)

def tan(x):
    return np.sin(x)/np.cos(x)

def arcsin(x):
    a1 = x.real
    dual={}
    for key in x.dual:
        a2 = x.e1[key]
```

```
            dual[key] = a2 * 1/(1-a1**2)**0.5
        return Dual(np.arcsin(a1), dual=dual, init=False)

    def arccos(x):
        a1 = x.real
        dual={}
        for key in x.dual:
            a2 = x.dual[key]
            dual[key] = a2 * -1/(1-a1**2)**0.5
        return Dual(np.arccos(a1), dual=dual, init=False)

    def arctan(x):
        a1 = x.real
        dual={}
        for key in x.dual:
            a2 = x.dual[key]
            dual[key] = a2 * 1/(1+a1**2)
        return Dual(np.arctan(a1), dual=dual, init=False)


def DN(C, var,x, posx):
    convert = {
        "p9":9,
        "p8":8,
        "p7":7,
        "p6":6,
        "p5":5,
        "p4":4,
        "p3":3,
        "p2":2,
        "p1":1,
        "":0,
        "m1":-1,
        "m2":-2,
        "m3":-3,
        "m4":-4,
        "m5":-5,
        "m6":-6,
```

```
        "m7":-7,
        "m8":-8,
        "m9":-9,

    }
    extra_x = convert[posx]
    return Dual(real=C[var,x+extra_x], dual={f'C_{var}_j{posx}': 1})
```

To verify the functionality of the Dual class we demonstrate its implementation in the evaluation of the function and derivative.

$$f(x) = x^2 + sin(x) + 4e^{x^2} \tag{7.1}$$

$$f'(x) = 2x + cos(x) + 8xe^{x^2} \tag{7.2}$$

Listing 7.2: DualNumberTest.py

```
from AutoGrad import Dual
import numpy as np
import matplotlib.pyplot as plt
from pylab import cm
import matplotlib as mpl

def f(x):
    return x**2    + np.sin(x) + 4 * np.exp(x**2)



def df_dx(x):
    return 2*x + np.cos(x) + 2*x*4*np.exp(x**2)


x_real = np.linspace(-1, 1, 100)


f_val = f(x_real)
dfdx_val = df_dx(x_real)



x_test = [-1, -0.5, 0, 0.5, 1]

reals=[]
duals=[]

for xval in x_test:
```

```
    dual_number = Dual(xval, dual={"x":1})
    function_evaluation = f(dual_number)

    real_component = function_evaluation.real
    dual_component = function_evaluation.dual["x"]

    reals.append(real_component)
    duals.append(dual_component)



### Plotting Portion


fig = plt.figure(figsize=(6, 4.8))


plt.rcParams['font.size'] = 24


plt.rcParams['axes.linewidth'] = 2


ax1 = fig.add_axes([1.4, -1.3, 1, 1])
# Hide the top and right spines of the axis
ax1.spines['right'].set_visible(True)
ax1.spines['top'].set_visible(True)




ax1.xaxis.set_tick_params
(which='major', size=10, width=2, direction='in', top='on')
ax1.xaxis.set_tick_params
(which='minor', size=7, width=2, direction='in', top='on')
ax1.yaxis.set_tick_params
(which='major', size=10, width=2, direction='in', top='on')
ax1.yaxis.set_tick_params
```

```
(which='minor', size=7, width=2, direction='in', top='on')


# Add the x and y-axis labels
ax1.set_xlabel(r'x', labelpad=10)
ax1.set_ylabel(r'f(x)', labelpad=10)

ax1.plot(x_real, f_val, "-", color="green", label = "Function")
ax1.plot(x_real, dfdx_val, color = "red", label = "Derivative")

ax1.plot(x_test, reals, "o", color="green")
ax1.plot(x_test, duals, "o", color = "red")


handles, labels = ax1.get_legend_handles_labels()
ax1.legend(handles[::1], labels[::1],
bbox_to_anchor=(1, 0.3), loc=1, frameon=False, fontsize=24)
```

Listing 7.3: LP57Params.py

```
"""
In this file we define a Python dict containing key parameters
for the simulation.
The dict is then passed to different
functions as an input for use in the solving procedure.
"""

import numpy as np
from bvp_solver_1D_HYPER import process

def generate_params(L1, hours, As, Ds, C_input, C_init):

    p_electrolyte=1.225*1000 # kg/m3
    ctot=12.984366034444264*1000 #mol/m3
    ctot_molal = ctot / p_electrolyte



    params = {
        "N":9, # Number of independent variables
        "ctot":ctot, # Total electrolyte concentration (mol/m3)
        "ctot_molal":ctot_molal, # Total concentration (mol/kg)
        "stepsize":1, # Stepsize used in solver
        "tol":1e-9, # Convergence criteria
        "itmax":60, # Max number of iterations
        "F":96485.3321233100184, # Faradays Constant
        "R":8.31446261815324, # Universal Gas Constant
        "T":303.15, # Temperature
        "timestep":60*60*hours, # Timestep between
        "I_A":2.5, # Applied current density (A/m2)
        "phi0":0.0, # Arbitrary value for one electrode potential
        "L0":2/1000, # Length of first region (m)
        "L1":L1/1000, # length of second region (m)
        "L2":2/1000, # length of third region (m)
        "N0":50, # Number of points in first region
```

```
    "N1":75, # Number of points in second region
    "NJ":125, # Number of points in total
    "As":As, # List containing thermodynamic activity factors
    "Ds":Ds, # List containing MS diffusivities (m2/s)

}


L0=params["L0"]
L1=params["L1"]
L2=params["L2"]


N0=params["N0"]
N1=params["N1"]
NJ=params["NJ"]

NJ_0 = N0
NJ_1= N1-N0+1
NJ_2 = NJ-N1 +1

L=L0+L1+L2


h0 = L0/(NJ_0-1)
h1 = L1/(NJ_1-1)
h2 = L2/(NJ_2-1)


mesh=[0]


for idx in range(1, NJ):
    if idx <= N0:
        value = mesh[idx-1] + h0
        mesh.append(value)
    elif N0 < idx <= N1:
        value = mesh[idx-1] + h1
```

```
            mesh.append(value)
        else:
            value = mesh[idx-1] + h2
            mesh.append(value)


mesh=np.array(mesh)
```

```
N=params["N"]
params["L"]=params["L0"]+params["L1"]+params["L2"]
L=params["L"]

NJ=params["NJ"]
timestep=params["timestep"]

if C_input:
    C=C_init.copy()
else:
    C=np.zeros((N,NJ),dtype=float)
    C[0,:]=0.0770157
    C[1,:]=0.0770157
    C[2,:]=0.33795813
    C[3,:]=0.50801047


params["mesh"]=mesh
params["h0"]=h0
params["h1"]=h1
params["h2"]=h2


params["Cold"]=C.copy()
```

```
    """
    process() takes params and generates a
    list of strings (C_i_j) where i is the
    variable and j is the meshpoint. This is
    then added to the params dict. The
    string is used in the solving function
    when looping to build the Jacobian
    matrix.
    """
    process(params)

    return params
```

Listing 7.4: Residual.py

```
from AutoGrad import Dual
import numpy as np
from X_Derivatives_oh4 import *
from DerivativesBoundary import *


def equations(C, j, params):
    N = params["N"]


    L0=params["L0"]
    L1=params["L1"]
    L2=params["L2"]


    N0=params["N0"]
    N1=params["N1"]
    NJ=params["NJ"]


    NJ_0 = N0
    NJ_1= N1-N0+1
    NJ_2 = NJ-N1 +1

    L=L0+L1+L2


    h0 = L0/(NJ_0-1)
    h1 = L1/(NJ_1-1)
    h2 = L2/(NJ_2-1)


    ctot=params["ctot"]
    F=params["F"]
    R=params["R"]
    T=params["T"]
    Cold = params["Cold"]
```

```
timestep=params["timestep"]
I_A=params["I_A"]
phi0=params["phi0"]

As=params["As"]
Ds=params["Ds"]




I_A_F = I_A/F

eq = np.zeros(N, dtype=object)


C_0_j = Dual(real=C[0,j], dual={'C_0_j': 1})
C_1_j = Dual(real=C[1,j], dual={'C_1_j': 1})
C_2_j = Dual(real=C[2,j], dual={'C_2_j': 1})
C_3_j = Dual(real=C[3,j], dual={'C_3_j': 1})
C_4_j = Dual(real=C[4,j], dual={'C_4_j': 1})
C_5_j = Dual(real=C[5,j], dual={'C_5_j': 1})
C_6_j = Dual(real=C[6,j], dual={'C_6_j': 1})
C_7_j = Dual(real=C[7,j], dual={'C_7_j': 1})
C_8_j = Dual(real=C[8,j], dual={'C_8_j': 1})

x_Li    = x_0 = C_0_j
x_PF6   = x_1 = C_1_j
x_EC    = x_2 = C_2_j
x_EMC   = x_3 = C_3_j

N_Li    = N_0 = C_4_j
N_PF6   = N_1 = C_5_j
N_EC    = N_2 = C_6_j
N_EMC   = N_3 = C_7_j

phi     = C_8_j
```

```
dc0_dt = (x_0*ctot - Cold[0,j]*ctot)/timestep
dc1_dt = (x_1*ctot - Cold[1,j]*ctot)/timestep
dc2_dt = (x_2*ctot - Cold[2,j]*ctot)/timestep
dc3_dt = (x_3*ctot - Cold[3,j]*ctot)/timestep
```

```
dx_0dx     = get_dC_dx(0, j, C, params)
dx_1dx     = get_dC_dx(1, j, C, params)
dx_2dx     = get_dC_dx(2, j, C, params)
dx_3dx     = get_dC_dx(3, j, C, params)
dN_Lidx    = get_dC_dx(4, j, C, params)
dN_PF6dx   = get_dC_dx(5, j, C, params)
dN_ECdx    = get_dC_dx(6, j, C, params)
dN_EMCdx   = get_dC_dx(7, j, C, params)
dphidx     = get_dC_dx(8, j, C, params)
```

```
d2x_0dx2     = get_d2C_dx2(0, j, C, params)
d2x_1dx2     = get_d2C_dx2(1, j, C, params)
d2x_2dx2     = get_d2C_dx2(2, j, C, params)
d2x_3dx2     = get_d2C_dx2(3, j, C, params)
d2N_Lidx2    = get_d2C_dx2(4, j, C, params)
d2N_PF6dx2   = get_d2C_dx2(5, j, C, params)
d2N_ECdx2    = get_d2C_dx2(6, j, C, params)
d2N_EMCdx2   = get_d2C_dx2(7, j, C, params)
d2phi_dx2    = get_d2C_dx2(8, j, C, params)
```

```
z_li=z_0= 1#0
z_pf6=z_1=-1#1
z_ec=z_2 = 0#2
z_emc=z_3 = 0#3
```

```
zc=x_0 * z_0 + x_1 * z_1 +x_2 * z_2+x_3 * z_3


A_00, A_01, A_02, A_10, A_11, A_12, A_20, A_21, A_22 = As


Factor_00 = A_00* dx_0dx
Factor_01 = A_01 * dx_1dx
Factor_02 = A_02 * dx_2dx

Factor_10 = A_10 * dx_0dx
Factor_11 = A_11 * dx_1dx
Factor_12 = A_12 * dx_2dx

Factor_20 = A_20 * dx_0dx
Factor_21 = A_21 * dx_1dx
Factor_22 = A_22 * dx_2dx

Factor_0 = Factor_00 + Factor_01 + Factor_02
Factor_1 = Factor_10 + Factor_11 + Factor_12
Factor_2 = Factor_20 + Factor_21 + Factor_22


D01, D02, D03, D13, D23, D12= Ds


d_01 = ( x_0 * N_1 - x_1 * N_0 )/( ctot * D01 )
d_02 = ( x_0 * N_2 - x_2 * N_0) /( ctot * D02 )
d_03 = ( x_0 * N_3 - x_3 * N_0) /( ctot * D03 )

d_12 = ( x_1 * N_2 - x_2 * N_1) /( ctot * D12 )
d_13 = ( x_1 * N_3 - x_3 * N_1) /( ctot * D13 )


d_23 = ( x_2 * N_3 - x_3 * N_2) /( ctot * D23 )
```

```
if j==0:
    eq[0] = N_Li-I_A_F
    eq[1] = zc
    eq[2] = N_EC
    eq[3] = N_EMC

    eq[4] = d_01 + d_02 + d_03 - Factor_0 -
    z_0 * F / R/T * dphidx * x_0
    eq[5] = -d_01 + d_12 + d_13 - Factor_1 -
    z_1 * F / R/T * dphidx * x_1
    eq[6] = -d_02 - d_12 + d_23 - Factor_2 -
    z_2 * F / R/T * dphidx * x_2
    eq[7] = x_0 + x_1 + x_2 + x_3 - 1


    if I_A_F < 0:
        eq[8] =phi-phi0
    else:
        eq[8]=N_PF6

elif 0<j<NJ-1:
    eq[0] = -dc0_dt-dN_Lidx
    eq[1] = -dc1_dt-dN_PF6dx
    eq[2] = -dc2_dt-dN_ECdx
    eq[3] = -dc3_dt-dN_EMCdx

    eq[4] = d_01 + d_02 + d_03 - Factor_0
    - z_0 * F / R/T * dphidx * x_0
    eq[5] = -d_01 + d_12 + d_13 - Factor_1
    - z_1 * F / R/T * dphidx * x_1
    eq[6] = -d_02 - d_12 + d_23 - Factor_2
    - z_2 * F / R/T * dphidx * x_2
```

```
        eq[7] = x_0 + x_1 + x_2 + x_3 - 1

        eq[8] =zc



    elif j == NJ-1:
        eq[0] = N_Li-I_A_F
        eq[1] = zc
        eq[2] = N_EC
        eq[3] = N_EMC
        eq[4] = d_01 + d_02 + d_03 - Factor_0
        - z_0 * F / R/T * dphidx * x_0
        eq[5] = -d_01 + d_12 + d_13 - Factor_1
        - z_1 * F / R/T * dphidx * x_1
        eq[6] = -d_02 - d_12 + d_23 - Factor_2
        - z_2 * F / R/T * dphidx * x_2
        eq[7] = x_0 + x_1 + x_2 + x_3 - 1
        if I_A_F >= 0:
            eq[8] =phi-phi0
        else:
            eq[8]=N_PF6
    return eq
```

Listing 7.5: ReturnResults.py

```
import numpy as np
from bvp_solver_1D_HYPER import solve_1D as solve

from Residual import equations
from LP57_Params import generate_params

def check_C(x, hours, L1, C_in=False, C_init=0):
    A_00, A_01, A_02, A_10, A_11, A_12,
    A_20, A_21, A_22, D01, D02, D03, D13,
    D23, D12 = x

    As = [A_00, A_01, A_02, A_10, A_11,
    A_12, A_20, A_21, A_22]

    Ds = [D01, D02, D03, D13, D23, D12]

    mesh,C = generate(As, Ds, hours, L1,
    C_input=C_in, C_init=C_init)

    return mesh, C


def generate(As, Ds, hours, L1,
C_input=False, C_init=0):
    params=generate_params(L1, hours, As,
    Ds, C_input, C_init)

    C, err_C, err_G, iteration=
    solve(params, equations,
    params["Cold"].copy())

    mesh=params["mesh"]
    return mesh,C


def output_results(x, L1, Nmax, hour, verbose=False):
    times=[]
```

```
Cs=[]
time=0
for run in range(Nmax):
    if verbose:
        print(time)
    if run==0:
        C_init=0
        C_in=False
    else:
        C_init=C.copy()
        C_in=True
    mesh, C = check_C(x, hour, L1, C_in=C_in, C_init=C_init)

    time+=hour
    times.append(time)
    Cs.append(C)
return times, mesh, Cs
```

Listing 7.6: bvpsolver1DHYPER.py

```
from AutoGrad import Dual


import numpy as np
from scipy.sparse import csc_matrix,csr_matrix
from scipy.sparse.linalg import spsolve

def process(params):
    N=params["N"]
    NJ=params["NJ"]
    var_list=[]
    for var in range(N):
        for j in range(NJ):
            name=f"C_{var}_{j}"
            var_list.append(name)

    var_solve=var_list
    indices =[]
    for idx, val in enumerate(var_list):
        if val in var_solve:
            indices.append(idx)
    indices = np.array(indices)
    params["indices"]=indices
    params["var_solve"]=var_solve
    params["var_list"]=var_list



def switch(dn, j, var):
    conversions = {
        f"C_{var}_j":f"C_{var}_{j}",
        f"C_{var}_jp1":f"C_{var}_{j+1}",
        f"C_{var}_jp2":f"C_{var}_{j+2}",
        f"C_{var}_jp3":f"C_{var}_{j+3}",
        f"C_{var}_jp4":f"C_{var}_{j+4}",
        f"C_{var}_jp5":f"C_{var}_{j+5}",
```

```
        f"C_{var}_jm1":f"C_{var}_{j-1}",
        f"C_{var}_jm2":f"C_{var}_{j-2}",
        f"C_{var}_jm3":f"C_{var}_{j-3}",
        f"C_{var}_jm4":f"C_{var}_{j-4}",
        f"C_{var}_jm5":f"C_{var}_{j-5}",

    }
    return conversions[dn]

def name_to_point(point1):
    point=point1.split("_")
    var, j = int(point[1]), int(point[2])
    return var,j

def solve_1D(params, equations, C):
    itmax=params["itmax"]
    NJ=params["NJ"]
    N=params["N"]
    tol=params["tol"]
    stepsize=params["stepsize"]
    var_list=params["var_list"]

    var_solve=params["var_solve"]
    indices = params["indices"]

    name_to_index = dict(zip(var_solve, indices))
    name_to_index = dict(zip(var_solve, range(len(var_solve))))

    dim=[N,NJ]
    L = N*NJ
    L_solve = len(var_solve)


    G = np.zeros(L_solve, dtype=np.float64)
    Jacobian = np.zeros((L_solve,L_solve), dtype=np.float64)

    deltaC = np.zeros(L,dtype=np.float64)
    err_old = 1e42
```

```
norm_G0=err_old
for iteration in range(itmax):
    G*=0
    Jacobian*=0
    deltaC*=0
    for point in var_solve:
        var,j = name_to_point(point)
        row=name_to_index[point]
        expression = equations(C,j,params)[var]

        G[row]=expression.real

        for dn in expression.dual:
            var_dual = int(dn.split("_")[1])
            dual_number = switch(dn,j,var_dual)
            column = name_to_index[dual_number]
            Jacobian[row,column]=expression.dual[dn]

    Jacobian =csc_matrix(Jacobian)
    deltaC = spsolve(Jacobian, G)
    deltaC = deltaC.reshape(N,NJ)
    err_C = np.sum(np.abs(deltaC))
    err_G = np.sum(np.abs(G))
    C -= deltaC*stepsize
    Jacobian = Jacobian.toarray()
    if err_C < tol:# and err_G < tol:
        break

return C, err_C, err_G, iteration
```

Listing 7.7: DerivativesBoundary.py

```
from X_Derivatives_oh4 import *


def get_dC_dx(var, j, C, params):
    NJ = params["NJ"]
    N0 = params["N0"]
    N1=params["N1"]
    h0 = params["h0"]
    h1 = params["h1"]
    h2 = params["h2"]

    if j == N0 -1:
        dC_dx = dCdx_xNm1(C, var, j,h0)
        return dC_dx
    elif j==N0:
        dC_dx = dCdx_boundary(C, var, j,h0,h1)
        return dC_dx
    elif j== N0+1:
        dC_dx = dCdx_x0(C, var, j,h1)
        return dC_dx




    elif j == N1 -1:
        dC_dx = dCdx_xNm1(C, var, j,h1)
        return dC_dx
    elif j==N1:
        dC_dx = dCdx_boundary(C, var, j,h1,h2)
        return dC_dx
    elif j== N1+1:
        dC_dx = dCdx_x0(C, var, j,h2)
        return dC_dx
```

```
    elif j==0:
        dC_dx = dCdx_x0(C, var, j,h0)
    elif j == 1:
        dC_dx = dCdx_x1(C, var, j,h0)

    elif j == NJ-2:
        dC_dx = dCdx_xNm2(C, var, j,h2)

    elif j == NJ-1:
        dC_dx = dCdx_xNm1(C, var, j,h2)
    else:
        if 0 <= j <= N0-1:
            h=h0
        elif N0+1 < j < N1-1:
            h=h1
        elif N1+1 < j < NJ-2:
            h=h2
        dC_dx = dCdx(C, var, j,h)

    return dC_dx




def get_d2C_dx2(var, j, C, params):
    NJ = params["NJ"]
    N0 = params["N0"]
    N1=params["N1"]
    h0 = params["h0"]
    h1 = params["h1"]
    h2 = params["h2"]

    if j == N0 -1:
        dC_dx = d2Cdx2_xNm1(C, var, j,h0)
        return dC_dx
    elif j==N0:
        dC_dx = d2Cdx2_boundary(C, var, j,h0,h1)
```

```
        return dC_dx
    elif j== N0+1:
        dC_dx = d2Cdx2_x0(C, var, j,h1)
        return dC_dx




    elif j == N1 -1:
        dC_dx = d2Cdx2_xNm1(C, var, j,h1)
        return dC_dx
    elif j==N1:
        dC_dx = d2Cdx2_boundary(C, var, j,h1,h2)
        return dC_dx
    elif j== N1+1:
        dC_dx = d2Cdx2_x0(C, var, j,h2)
        return dC_dx




    elif j==0:
        dC_dx = d2Cdx2_x0(C, var, j,h0)
    elif j == 1:
        dC_dx = d2Cdx2_x1(C, var, j,h0)

    elif j == NJ-2:
        dC_dx = d2Cdx2_xNm2(C, var, j,h2)

    elif j == NJ-1:
        dC_dx = d2Cdx2_xNm1(C, var, j,h2)
    else:
        if 0 <= j <= N0-1:
            h=h0
        elif N0+1 < j < N1-1:
            h=h1
        elif N1+1 < j < NJ-2:
            h=h2
```

```
        dC_dx = d2Cdx2(C, var, j,h)

    return dC_dx
```

Listing 7.8: XDerivativesoh4.py

```
from AutoGrad import DN


def dCdx_x0(C, var, x,h):
    x0 = DN(C, var, x, "")
    x1 = DN(C, var, x, "p1")
    x2 = DN(C, var, x, "p2")
    x3 = DN(C, var, x,"p3")
    x4 = DN(C, var, x,"p4")
    x5 = DN(C, var, x, "p5")
    f = [x0,x1,x2,x3,x4,x5]
    i=0

    res = (-54.8*f[i+0]+120*f[i+1]
    -120*f[i+2]+80*f[i+3]-30*f[i+4] + 4.8*f[i+5])
    /(24*1.0*h**1)
    return res

def d2Cdx2_x0(C, var, x,h):
    x0 = DN(C, var, x, "")
    x1 = DN(C, var, x, "p1")
    x2 = DN(C, var, x, "p2")
    x3 = DN(C, var, x,"p3")
    x4 = DN(C, var, x,"p4")
    x5 = DN(C, var, x, "p5")
    f = [x0,x1,x2,x3,x4,x5]
    i=0
    res = (45*f[i+0]-154*f[i+1]+214*f[i+2]
    -156*f[i+3]+61*f[i+4]-10*f[i+5])
    /(12*1.0*h**2)

    return res


def dCdx_x1(C, var, x,h):
    xm1=DN(C, var, x, "m1")
    x0 = DN(C, var, x, "")
```

```
    x1 = DN(C, var, x, "p1")
    x2 = DN(C, var, x, "p2")
    x3 = DN(C, var, x,"p3")
    x4 = DN(C, var, x,"p4")
    f = [xm1,x0,x1,x2,x3,x4]
    i=1
    res = (-3*f[i-1]-10*f[i+0]+18*f[i+1]
    -6*f[i+2]+1*f[i+3])
    /(12*1.0*h**1)

    return res
def d2Cdx2_x1(C, var, x,h):
    xm1=DN(C, var, x, "m1")
    x0 = DN(C, var, x, "")
    x1 = DN(C, var, x, "p1")
    x2 = DN(C, var, x, "p2")
    x3 = DN(C, var, x,"p3")
    x4 = DN(C, var, x,"p4")
    f = [xm1,x0,x1,x2,x3,x4]
    i=1
    res = (10*f[i-1]-15*f[i+0]-4*f[i+1]+14*f[i+2]
    -6*f[i+3]+1*f[i+4])
    /(12*1.0*h**2)
    return res




def dCdx(C, var, x,h):
    xm2=DN(C, var, x, "m2")
    xm1=DN(C, var, x, "m1")
    x0 = DN(C, var, x, "")
    x1 = DN(C, var, x, "p1")
    x2 = DN(C, var, x, "p2")

    f = [xm2,xm1,x0,x1,x2]
    i=2
```

```
    res=(1*f[i-2]-8*f[i-1]+0*f[i+0]+8*f[i+1]
    -1*f[i+2])
    /(12*1.0*h**1)
    return res

def d2Cdx2(C, var, x,h):
    xm2=DN(C, var, x, "m2")
    xm1=DN(C, var, x, "m1")
    x0 = DN(C, var, x, "")
    x1 = DN(C, var, x, "p1")
    x2 = DN(C, var, x, "p2")

    f = [xm2,xm1,x0,x1,x2]
    i=2
    res=(-1*f[i-2]+16*f[i-1]-30*f[i+0]
    +16*f[i+1]-1*f[i+2])
    /(12*1.0*h**2)
    return res

def dCdx_xNm1(C, var, x,h):
    x0 = DN(C, var, x, "")
    xm1=DN(C, var, x, "m1")
    xm2=DN(C, var, x, "m2")
    xm3=DN(C, var, x, "m3")
    xm4=DN(C, var, x, "m4")

    f = [xm4,xm3,xm2,xm1,x0]
    i=4
    res = (3*f[i-4]
    -16*f[i-3]+36*f[i-2]-48*f[i-1]+25*f[i+0])
    /(12*1.0*h**1)

    return res


def d2Cdx2_xNm1(C, var, x,h):
    x0 = DN(C, var, x, "")
    xm1=DN(C, var, x, "m1")
```

```
    xm2=DN(C, var, x, "m2")
    xm3=DN(C, var, x, "m3")
    xm4=DN(C, var, x, "m4")
    xm5=DN(C, var, x, "m5")

    f = [xm5,xm4,xm3,xm2,xm1,x0]
    i=5
    res = (-10*f[i-5]+61*f[i-4]
    -156*f[i-3]
    +214*f[i-2]-154*f[i-1]+45*f[i+0])

    /(12*1.0*h**2)
    return res

def dCdx_xNm2(C, var, x,h):
    xp1=DN(C, var, x, "p1")
    x0 = DN(C, var, x, "")
    xm1=DN(C, var, x, "m1")
    xm2=DN(C, var, x, "m2")
    xm3=DN(C, var, x, "m3")
    xm4=DN(C, var, x, "m4")
    f = [xm3,xm2,xm1,x0,xp1]
    i=3
    res=(-1*f[i-3]+6*f[i-2]
    -18*f[i-1]+10*f[i+0]+3*f[i+1])
    /(12*1.0*h**1)
    return res

def d2Cdx2_xNm2(C, var, x,h):
    xp1=DN(C, var, x, "p1")
    x0 = DN(C, var, x, "")
    xm1=DN(C, var, x, "m1")
    xm2=DN(C, var, x, "m2")
    xm3=DN(C, var, x, "m3")
    xm4=DN(C, var, x, "m4")
    f = [xm4,xm3,xm2,xm1,x0,xp1]
    i=4
    res=(1*f[i-4]-6*f[i-3]
```

```
    +14*f[i-2]-4*f[i-1]-15*f[i+0]+10*f[i+1])
    /(12*1.0*h**2)
    return res


def dCdx_boundary(C, var, x,hb,hf):
    xm1=DN(C, var, x, "m1")
    xm2=DN(C, var, x, "m2")
    xm3=DN(C, var, x, "m3")
    x0 = DN(C, var, x, "")
    xp1=DN(C, var, x, "p1")
    xp2=DN(C, var, x, "p2")
    xp3=DN(C, var, x, "p3")

    f = [xm3,xm2,xm1,x0,xp1,xp2,xp3]
    i=3
    res = (-4 * f[i-3]
    + 18 * f[i-2] - 36*f[i-1] + 0*f[i] + 36*f[i+1] -18 * f[i+2]
    + 4*f[i+3] )/( 12 * (hb + hf) )
    return res

def d2Cdx2_boundary(C, var, x,hb,hf):
    xm1=DN(C, var, x, "m1")
    xm2=DN(C, var, x, "m2")
    xm3=DN(C, var, x, "m3")
    x0 = DN(C, var, x, "")
    xp1=DN(C, var, x, "p1")
    xp2=DN(C, var, x, "p2")
    xp3=DN(C, var, x, "p3")

    f = [xm3,xm2,xm1,x0,xp1,xp2,xp3]
    i=3
    res = (-12 * f[i-3] + 48 * f[i-2] - 60*f[i-1] + 0*f[i]
    + 60*f[i+1] -48 * f[i+2] + 12*f[i+3] )
    /( -12 * (hf**2-hb**2) )
    return res
```

Listing 7.9: Main.py

```
from Return_Results import output_results
import numpy as np
import pandas as pd


x = np.array([ 0.97513288, -0.02483064, -0.06104164, -0.02486712,
0.97516936,
        -0.06104164, -0.23697094, -0.23697079,  0.28045965,

9.401416288598671e-11,
 2.3783791564556085e-10,
 2.069208058780769e-10,
 3.6231124928427994e-11,
 5.772339428596073e-11,
 2.3398883774755926e-10])


L1 = 2.412
hour=0.25
Nmax = int(1/hour*18)

times, mesh1, Cs = output_results(x, L1, Nmax, hour)
```